

# The Stability and Dynamics of Localized Spot Patterns in the Two-Dimensional Gray-Scott Model

W. CHEN, M. J. WARD

*Wan Chen; Department of Mathematics, University of British Columbia, Vancouver, British Columbia, V6T 1Z2, Canada,  
(Currently at OCCAM, Oxford University, Oxford, U.K.)*

*Michael J. Ward; Department of Mathematics, University of British Columbia, Vancouver, British Columbia, V6T 1Z2, Canada  
(corresponding author)*

*(Received 10 September 2010)*

The dynamics and stability of multi-spot patterns to the Gray-Scott (GS) reaction-diffusion model in a two-dimensional domain is studied in the singularly perturbed limit of small diffusivity  $\varepsilon$  of one of the two solution components. A hybrid asymptotic-numerical approach based on combining the method of matched asymptotic expansions with the detailed numerical study of certain eigenvalue problems is used to predict the dynamical behavior and instability mechanisms of multi-spot quasi-equilibrium patterns for the GS model in the limit  $\varepsilon \rightarrow 0$ . For  $\varepsilon \rightarrow 0$ , a quasi-equilibrium  $k$ -spot pattern is constructed by representing each localized spot as a logarithmic singularity of unknown strength  $S_j$  for  $j = 1, \dots, k$  at unknown spot locations  $\mathbf{x}_j \in \Omega$  for  $j = 1, \dots, k$ . A formal asymptotic analysis is then used to derive a differential algebraic ODE system for the collective coordinates  $S_j$  and  $\mathbf{x}_j$  for  $j = 1, \dots, k$ , which characterizes the slow dynamics of a spot pattern. Instabilities of the multi-spot pattern due to the three distinct mechanisms of spot self-replication, spot oscillation, and spot annihilation, are studied by first deriving certain associated eigenvalue problems by using singular perturbation techniques. From a numerical computation of the spectrum of these eigenvalue problems, phase diagrams representing in the GS parameter space corresponding to the onset of spot instabilities are obtained for various simple spatial configurations of multi-spot patterns. In addition, it is shown that there is a wide parameter range where a spot instability can be triggered only as a result of the intrinsic slow motion of the collection of spots. The construction of the quasi-equilibrium multi-spot patterns and the numerical study of the spectrum of the eigenvalue problems relies on certain detailed properties of the reduced-wave Green's function. The hybrid asymptotic-numerical results for spot dynamics and spot instabilities are validated from full numerical results computed from the GS model for various spatial configurations of spots.

Key words: matched asymptotic expansions, spots, self-replication, logarithmic expansions, eigenvalues, Hopf bifurcation, reduced-wave Green's function, circulant matrix.

## 1 Introduction

Spatially localized spot patterns have been observed in a wide variety of experimental settings including, the ferrocyanide-iodate-sulphite reaction (cf. [40]), the chloride-dioxide-malonic acid reaction (cf. [14]), and certain electronic gas-discharge systems (cf. [3], [4]). Furthermore, numerical simulations of certain simple reaction-diffusion systems, such as the two-component Gray-Scott model (cf. [48], [42]) and a three-component gas-discharge model (cf. [52]), have shown the occurrence of complex spatio-temporal localized spot patterns exhibiting a wide range of different instabilities including, spot oscillation, spot annihilation, and spot self-replication behavior. A survey of experimental and theoretical studies, through reaction-diffusion (RD) modeling, of localized spot patterns in various physical or chemical contexts is given in [55]. These experimental and numerical studies have provided considerable impetus for developing a theoretical understanding of the dynamics, stability, and spot self-replication behavior associated with localized solutions to singularly perturbed RD systems. A brief survey of some new directions and open

problems for the theoretical study of localized patterns in various applications is given in [30]. More generally, a wide range of topics in the analysis of far-from-equilibrium patterns modeled by PDE systems are discussed in [45].

In this context, the goal of this paper is to provide a detailed case study of the dynamics, stability, and self-replication behavior, of localized multi-spot patterns for the Gray-Scott (GS) RD system in a two-dimensional domain. The GS model is formulated in dimensionless form as (cf. [44])

$$v_t = \varepsilon^2 \Delta v - v + Auv^2, \quad \tau u_t = D \Delta u + (1 - u) - uv^2, \quad \mathbf{x} \in \Omega \in \mathbb{R}^2; \quad \partial_n u = \partial_n v = 0, \quad \mathbf{x} \in \partial\Omega. \quad (1.1)$$

Here  $\varepsilon > 0$ ,  $D > 0$ ,  $\tau > 1$ , and  $A$  are constants. The parameter  $A$  is called the feed-rate parameter. For various ranges of these parameters, (1.1) has a rich solution structure consisting of oscillating spots, spot annihilation behavior, spot self-replication, and stripe and labyrinthian patterns. For the specific choice  $D = 2\varepsilon^2$ , the complexity and diversity of these patterns were first studied numerically in [48] in the unit square. Further numerical studies that clearly exhibit the distinguishing phenomena of spot self-replication in a two-dimensional domain include [42] and [50].

For the study of localized patterns in the GS model (1.1), there are two distinguished limits for the diffusion coefficient  $D$  in (1.1); the weak interaction regime with  $D = \mathcal{O}(\varepsilon^2)$ , where the original numerical simulations of the GS model were performed (cf. [48]), and the semi-strong interaction regime  $D = \mathcal{O}(1)$ , where many analytical studies have been focused. In the weak interaction regime, there is only an exponentially weak coupling between any two spots in the multi-spot pattern. This weak coupling arises from the exponential decay of a local spot profile. In contrast, in the semi-strong interaction regime, and for a certain range of  $A$ , the spots are more strongly coupled through the long-range effect of the slowly varying  $u$  component in (1.1). In this way, for  $D = \mathcal{O}(1)$  the dynamics of each individual spot in a multi-spot pattern is rather strongly influenced by the locations of the other spots in the pattern, as well as by the geometry of the confining domain.

In a one-dimensional spatial domain, there has been much work over the past decade in analyzing the stability, dynamics, and self-replication of spike patterns for the GS model (1.1). For the weak interaction regime where  $D = \mathcal{O}(\varepsilon^2)$  and  $A = \mathcal{O}(1)$ , the mechanism for spike self-replication put forth in [46] (see also [54]) was based on the occurrence of a nearly-coinciding hierarchical saddle-node global bifurcation structure for the global bifurcation branches of multi-spike solutions. This mechanism was also shown to occur for the related Gierer-Meinhardt (GM) system (cf. [45]). In this one-dimensional context, it was shown in [24] that typically only the spikes at the edges of a multi-spike pattern can undergo splitting. The possibility of spatial-temporal chaotic behavior of spike patterns due to repeated annihilation and self-replication events was explored in [47] from a global bifurcation viewpoint. The study of solution behavior in this weak interaction regime relies heavily on the use of numerically computed global bifurcation diagrams, since it appears to be analytically intractable to study the local problem near each spike. In contrast, for the semi-strong interaction regime  $D = \mathcal{O}(1)$  there are many analytical studies of spike behavior for (1.1) for different ranges of the parameter  $A$ . For the range  $\mathcal{O}(\varepsilon^{1/2}) \leq A \ll \mathcal{O}(1)$ , oscillatory instabilities of the spike profile, characterized in terms of threshold values of the time-constant  $\tau$  in (1.1), have been analyzed in [17], [18], [43], [34], and [9]. Competition or annihilation instabilities of the spike profile, characterized by threshold values of the diffusivity  $D$ , have been analyzed in [34] for the range  $A = \mathcal{O}(\varepsilon^{1/2})$ . In addition, self-replication instabilities of spike patterns have been shown to occur only in the regime  $A = \mathcal{O}(1)$ , and they have been well-studied in [50], [51], [18], [44], [35], and [20]. Weak translation, or drift, instabilities of spike patterns have been analyzed in [33] and [35]. Finally, there have been several studies of the dynamical behavior of spike patterns for the one-dimensional GS model including, two-spike dynamics for the infinite-line problem (cf. [15], [16]) and in a bounded domain (cf. [53]),

and multi-spike patterns on a bounded domain (cf. [9]). Related studies on the stability and dynamics of spike solutions for the GM model in a one-dimensional domain are given in [29], [28], [59], [21], and [56] (see also the references therein). For the semi-strong regime  $D = \mathcal{O}(1)$ , one key feature of the GS model (1.1) in one spatial dimension is that the parameter regime  $A = \mathcal{O}(\varepsilon^{1/2})$  where spike competition instabilities occur is well-separated in parameter space from the range  $A = \mathcal{O}(1)$  where spike self-replication occurs. As we discuss below, this feature with the one-dimensional GS model is in distinct contrast to the two-dimensional GS model (1.1) where several distinct spot instability mechanisms occur in nearby parameter regimes for  $A$ .

Although the stability properties of spike patterns for the one-dimensional case is rather well-understood, there are only a few studies of the stability of multi-spot patterns for singularly perturbed two-component RD systems in two dimensional domains. In particular, for the GS model (1.1) on the infinite plane  $\Omega = \mathbb{R}^2$ , the existence and the stability, with respect to locally radially symmetric perturbations, of a one-spot solution to (1.1) was studied in [60] for the range  $A = \mathcal{O}(\varepsilon(-\ln \varepsilon)^{1/2})$  with either  $D = \mathcal{O}(1)$  or  $D = \mathcal{O}(\nu^{-1})$ , where  $\nu \equiv -1/\ln \varepsilon$ . This rigorous study was based on first deriving, and then analyzing, a certain nonlocal eigenvalue problem (NLEP). For the same range of  $A$ , in [62] the one-spot NLEP stability analysis of [60] was extended to treat the case of multi-spot patterns on a bounded domain. A further extension of this theory to study certain asymmetric multi-spot patterns was made in [61]. The  $k$ -spot NLEP stability analysis of [62] for the regime  $A = \mathcal{O}(\varepsilon(-\ln \varepsilon)^{1/2})$  was based on retaining only the leading-order term in powers of  $\nu \equiv -1/\ln \varepsilon$  in the construction of the spot profile, and it pertains to the class of locally radially symmetric perturbations near each spot. This theory characterizes competition and oscillatory profile instabilities for the parameter range  $A = \mathcal{O}(\varepsilon(-\ln \varepsilon)^{1/2})$  with either  $D = \mathcal{O}(1)$  or  $D = \mathcal{O}(\nu^{-1})$ . In this leading-order theory, the stability thresholds depend only on the number of spots, and not on their spatial locations in the multi-spot pattern. Spot self-replication instabilities were not accounted for in these NLEP studies, as this instability is triggered by a locally non-radially symmetric perturbation near each spot for the nearby parameter regime  $A = \mathcal{O}(\varepsilon(-\ln \varepsilon))$  (cf. [43]). A survey of NLEP stability theory as applied to other two-component singularly perturbed RD systems, such as the GM and Schnakenburg models, is given in [63].

With regards to the dynamics of spots, there are only a few analytical results characterizing spot dynamics for singularly perturbed RD systems in two-dimensional domains. These include, [11], [31] and [58] for a one-spot solution of the GM model, [22], [23] and [25] for exponentially weakly interacting metastable spots in various contexts, [38] for the Schnakenburg model, and [52] for a three-component gas-discharge RD model. We are not aware of any previous study of the dynamics of spots for the GS model (1.1) in a two-dimensional domain.

We emphasize that the previous NLEP stability studies for the GS model (1.1) (cf. [60], [61], [62]) are based on a leading-order theory in powers of  $\nu = -1/\ln \varepsilon$  for the parameter range  $A = \mathcal{O}(\varepsilon(-\ln \varepsilon)^{1/2})$  with either  $D = \mathcal{O}(1)$  or  $D = \mathcal{O}(\nu^{-1})$ . Therefore, since  $\nu$  is not very small unless  $\varepsilon$  is extremely small, it is desirable to obtain a stability theory for multi-spot solutions that accounts for all terms in powers of  $\nu$ . However, more importantly, since the scaling regime  $A = \mathcal{O}(-\varepsilon \ln \varepsilon)$  where a spot-replication instability can occur for (1.1) (cf. [43]) is logarithmically close to the low feed-rate regime  $A = \mathcal{O}(\varepsilon(-\ln \varepsilon)^{1/2})$  studied in [62] and [60], where only competition or oscillatory profile instabilities can occur, it is highly desirable to develop an asymptotic theory that incorporates these two slightly different scaling regimes into a single parameter regime where all three types of spot instability can be studied simultaneously. The leading-order theory in [62] is not sufficiently accurate to study the three types of spot profile instability (competition, oscillatory, and self-replication) within a single parameter regime.

For the simpler Schnakenburg RD model, where competition and oscillatory instabilities do not occur when  $D =$

$\mathcal{O}(1)$ , a hybrid asymptotic-numerical method was developed in [38] to study the dynamics and self-replication instabilities of a collection of spots for this specific RD model in an arbitrary two-dimensional domain. The theory, which accounts for all terms in powers of  $\nu = -1/\ln \varepsilon$ , was illustrated explicitly for the square and the disk, and the results from this theory were favorably compared with full numerical computations of the RD system.

The main goal of this paper is to extend the theoretical framework of [38] for the Schnakenburg model to study the dynamics and three types of instabilities associated with a collection of spots for the GS model (1.1) in the semi-strong parameter regime  $D = \mathcal{O}(1)$  with  $A = \mathcal{O}(-\varepsilon \ln \varepsilon)$ . In our theory we account for all terms in powers of  $\nu = -1/\ln \varepsilon$ . In contrast to the Schnakenburg model of [38], we emphasize that there are three distinct instability mechanisms for a collection of spots to the GS model (1.1) in this scaling regime for  $A$  and  $D$  that must be considered.

We now give an outline of the paper. In §2 and §3 the method of matched asymptotic expansions is used to construct a quasi-equilibrium  $k$ -spot pattern for (1.1) that evolves slowly over a long  $\mathcal{O}(\varepsilon^{-2})$  time scale. For this pattern, the spatial profile for  $v$  concentrates at a set of points  $\mathbf{x}_j \in \Omega$  for  $j = 1, \dots, k$  that drift with an asymptotically small  $\mathcal{O}(\varepsilon^2)$  speed. Within an  $\mathcal{O}(\varepsilon)$  neighborhood of each spot centered at  $\mathbf{x}_j$ , and at any instant in  $t$ , the local spot profiles for  $u$  and  $v$  are radially symmetric to within  $\mathcal{O}(\varepsilon)$  terms and satisfy a coupled system of BVP, referred to as the *core problem*, on the (stretched) infinite plane. In the outer region, each spot at a given instant in time is represented as a Coulomb singularity for  $u$  of strength  $S_j$ . The *collective coordinates* characterizing the slow dynamics of this quasi-equilibrium  $k$ -spot pattern are the locations  $\mathbf{x}_1, \dots, \mathbf{x}_k$  of the spots and their corresponding source strengths  $S_1, \dots, S_k$ , which measure the far-field logarithmic growth of the (inner) core solution for  $u$  near each spot. By asymptotically matching the inner and outer solutions for  $u$ , we derive a differential algebraic system (DAE) of ODE's for the slow time evolution of these collective coordinates. At any instant in time, the quasi-equilibrium solution is characterized as in Principal Result 2.1, where the source strengths  $S_j$  for  $j = 1, \dots, k$  are shown to satisfy a coupled nonlinear algebraic system that depends on the instantaneous spot locations  $\mathbf{x}_j$  for  $j = 1, \dots, k$ , together with certain properties of the reduced-wave Green's function  $G(\mathbf{x}; \mathbf{x}_j)$  and its regular part  $R_{jj}$  defined by

$$\Delta G - \frac{1}{D}G = -\delta(\mathbf{x} - \mathbf{x}_j), \quad \mathbf{x} \in \Omega; \quad \partial_n G = 0, \quad \mathbf{x} \in \partial\Omega, \quad (1.2 a)$$

$$G(\mathbf{x}; \mathbf{x}_j) \sim -\frac{1}{2\pi} \ln |\mathbf{x} - \mathbf{x}_j| + R_{j,j} + o(1), \quad \text{as } \mathbf{x} \rightarrow \mathbf{x}_j. \quad (1.2 b)$$

In Principal Result 3.1 of §3 the dynamical behavior of the collection of spots is characterized in terms of the source strengths and certain gradients of the reduced-wave Green's function. The overall DAE ODE system for  $\mathbf{x}_j$  and  $S_j$ , for  $j = 1, \dots, k$ , incorporates the interaction between the spots and the geometry of the domain, as mediated by the reduced-wave Green's function and its regular part, and it also accounts for all logarithmic correction terms in powers of  $\nu = -1/\ln \varepsilon$  in the asymptotic expansion of the solution. In this DAE ODE system there are two nonlinear functions of  $S_j$ , defined in terms of the solution to the core problem, that must be computed numerically.

In §4.1 we study spot self-replication instabilities by first deriving a local eigenvalue problem near the  $j^{\text{th}}$  spot that characterizes any instability due to a non-radially symmetric local deformation of the spot profile. We emphasize that in this stability analysis the local eigenvalue problems near each spot are not coupled together, except in the sense that the source strengths  $S_1, \dots, S_k$  must be determined from a globally coupled nonlinear algebraic system. The spectrum of the local two-component linear eigenvalue problem near the  $j^{\text{th}}$  spot is studied numerically, and we show that there is a critical value  $\Sigma_2 \approx 4.31$  of the source strength  $S_j$  for which there is a peanut-splitting linear instability for any  $S_j > \Sigma_2$ . These results for spot-splitting parallel those for the Schnakenburg model, as given in [38]. As a new result, we derive and then numerically study a certain time-dependent elliptic-parabolic core problem near the  $j^{\text{th}}$

spot. Our computations from this time-dependent core problem strongly suggest that the localized peanut-splitting linear instability of the quasi-equilibrium spot profile is in fact subcritical, and robustly triggers a nonlinear spot self-replication event for the  $j^{\text{th}}$  spot whenever  $S_j > \Sigma_2$ . In summary, our hybrid asymptotic-numerical theory predicts that if  $S_J > \Sigma_2 \approx 4.31$  for some  $J \in \{1, \dots, k\}$  then the  $J^{\text{th}}$  spot will undergo a nonlinear spot self-replication event. Alternatively, the spots are all stable to self-replication whenever  $S_j < \Sigma_2$  for  $j = 1 \dots, k$ .

In §4.2 we use the method of matched asymptotic expansions to formulate a novel global eigenvalue problem associated with competition or oscillatory instabilities in the spot amplitudes for a  $k$ -spot quasi-equilibrium solution to (1.1) for the parameter range  $A = \mathcal{O}(-\varepsilon \ln \varepsilon)$  with  $D = \mathcal{O}(1)$ . This global eigenvalue problem, as formulated in Principal Result 4.1, is associated with a locally radially symmetric perturbation near each spot, and it accounts for all terms in powers of  $\nu$ . It differs from the eigenvalue problem characterizing spot self-replication in that now the local eigenfunction for the perturbation of the  $u$  component in (1.1) has a logarithmic growth away from the center of each spot. This logarithmic growth leads to a global eigenvalue problem that effectively couples together the local problems near each spot. A key component in the formulation of this global eigenvalue problem is a certain eigenvalue-dependent Green's matrix, with entries determined in terms of properties the Green's function  $G_\lambda(\mathbf{x}; \mathbf{x}_j)$  satisfying  $\Delta G - D^{-1}(1 + \tau\lambda)G = -\delta(x - x_j)$  for  $\mathbf{x} \in \Omega$ , with  $\partial_n G = 0$  for  $\mathbf{x} \in \partial\Omega$ . This globally coupled eigenvalue problem can be viewed, essentially, as an extended NLEP theory that accounts for all terms in powers of  $\nu$ . In §5–§6 we show that it determines thresholds for competition and oscillatory instabilities very accurately. However, in contrast to the leading-order-in- $\nu$  NLEP stability studies (cf. [60], [62]) for  $A = \mathcal{O}(\varepsilon[-\ln \varepsilon]^{1/2})$ , our globally coupled eigenvalue problem is not readily amenable to rigorous analysis. In Appendix B we briefly review the NLEP theory of [60] and [62], and we show how our globally coupled eigenvalue problem can be reduced to leading order in  $\nu$  to the NLEP problems of [60] and [62] when  $A = \mathcal{O}(\varepsilon[-\ln \varepsilon]^{1/2})$  and  $D = \mathcal{O}(\nu^{-1})$ .

In our stability analysis of §4 we linearize the GS model (1.1) around a quasi-equilibrium solution where the spots are assumed to be at fixed locations  $\mathbf{x}_1, \dots, \mathbf{x}_k$ , independent of time. However, since the spots locations undergo a slow drift with speed  $\mathcal{O}(\varepsilon^2)$ , the source strengths  $S_j$  for  $j = 1, \dots, k$  also vary slowly in time on a time-scale  $t = \mathcal{O}(\varepsilon^{-2})$ . As a result of this slow drift, there can be triggered, or dynamically induced, instabilities of a quasi-equilibrium spot pattern that is initially stable at time  $t = 0$ . To illustrate this, suppose that the pattern is initially stable to spot self-replication at  $t = 0$  in the sense that  $S_j < \Sigma_2$  at  $t = 0$  for  $j = 1, \dots, k$ . Then, it is possible, that as the  $J^{\text{th}}$  spot drifts toward its equilibrium location in the domain, that  $S_J > \Sigma_2$  after a sufficiently long time of order  $t = \mathcal{O}(\varepsilon^{-2})$ . This will trigger a nonlinear spot self-replication event for the  $J^{\text{th}}$  spot. In a similar way, we show that dynamically-triggered oscillatory and competition instabilities can also occur for a multi-spot pattern. This dynamical bifurcation phenomena is similar to that for other ODE and PDE slow passage problems (cf. [5], [39]) that have triggered instabilities generated by a slowly varying *external* bifurcation, or control, parameter. The key difference here, is that the dynamically-triggered instabilities for the GS model (1.1) occur as a result of the *intrinsic* motion of the collection of spots, and is not due to the tuning of an external control parameter.

In our numerical computations of competition and oscillatory instability thresholds from our globally coupled eigenvalue problem of §4.2, we will for simplicity only consider  $k$ -spot quasi-equilibrium spot configurations  $\mathbf{x}_1, \dots, \mathbf{x}_k$  for which a certain Green's matrix is circulant symmetric. For instance, this circulant matrix structure occurs when  $k$  spots are equally spaced on a circular ring that is concentric within a circular disk, and it also occurs for other spot patterns with sufficient spatial symmetry in other domains. Examples of such patterns are given in §5 and 6 below. Under this condition, we show in §2.1 that the source strengths  $S_j$  for  $j = 1, \dots, k$  have a common value. In

addition, by calculating the spectrum of the circulant symmetric Green’s matrix, we show in Principal Result 4.3 of §4.3 that the globally coupled eigenvalue problem simplifies to  $k$  separate transcendental equations for the eigenvalue parameter. In Appendix C we outline the numerical methods that we use to compute the instability thresholds from the globally coupled eigenvalue problem under the circulant Green’s matrix assumption.

Spot patterns that give rise to this special circulant matrix structure are the direct counterpart of *equally-spaced*  $k$ -spike patterns with spikes of a common amplitude, treated in almost all of the previous NLEP stability studies of the GS and related RD models on a one-dimensional domain (cf. [17], [18], [34], [15], [16], [29], [59], [21], [56]). In one spatial dimension, the only NLEP stability studies of an *arbitrarily-spaced* slowly evolving  $k$ -spike quasi-equilibrium solution are the asymptotic-numerical study of dynamic competition instabilities for the Gierer-Meinhardt model with  $\tau = 0$  in [28], and the study of oscillatory instabilities in [9] for the one-dimensional GS model for the range  $\mathcal{O}(\varepsilon^{1/2}) \ll A \ll \mathcal{O}(1)$ . For this range of  $A$  it was shown in [9] that the  $k$  separate NLEP problems can be reduced, via a scaling law, to only one single NLEP problem. To date, there has been no NLEP stability study of a slowly evolving *arbitrarily-spaced*  $k$ -spike quasi-equilibrium spike pattern in a one-dimensional domain that takes into account both competition and oscillatory instabilities. As a result, in our two-dimensional setting, it is a natural first step to study the global eigenvalue problem, which governs competition and oscillatory instabilities, under the circulant matrix condition, which allows for spots of a common source strength.

In §5 the asymptotic theory of §2– §4 is illustrated for the case of both one and two-spot quasi-equilibrium solutions to the GS model (1.1) on the infinite plane. Phase diagrams characterizing the GS parameter ranges for the different types of instabilities are derived for these simple spot patterns. In particular, for two spots that are sufficiently far apart, we show that spot self-replication instabilities will occur when  $A$  exceeds some threshold. In contrast, a competition instability will occur if the two spots are too closely spaced. For a very large, but finite, domain the full numerical simulations in §5.3 are used to validate the stability results from the asymptotic theory.

In §6 the asymptotic theory of §2– §4 is implemented and compared with full numerical results computed from (1.1) for various special multi-spot patterns on the unit disk and square for which a certain Green’s matrix has a circulant matrix structure. For these domains, the explicit formulae for the reduced-wave Green’s function and its regular part, as derived in Appendix A, are used to numerically implement the asymptotic theory. The overall hybrid asymptotic-numerical approach provides phase diagrams in parameter space characterizing both the stability thresholds and the possibility of dynamically-triggered instabilities. One key theoretical advantage of considering the unit disk is that the reduced-wave Green’s function can be well-approximated for  $D \gg 1$  by the Neumann Green’s function, which has a simple explicit formula in the unit disk. By using this explicit formula, the hybrid asymptotic-numerical framework of §2– §4 can be studied, to a large extent, analytically for the case of  $k$  equally-spaced spots on a ring that is concentric within the unit disk.

In §7 we compare our theoretical predictions for spot dynamics and spot self-replication instabilities with full numerical results computed from (1.1) for a few simple “asymmetric” spot patterns for which the associated Green’s matrix is not circulant. We show that the dynamics in Principal Result 3.1 accurately determines spot dynamics before a self-replication event, and with a re-calibration of the initial spot locations, it accurately predict spot dynamics after a spot-splitting event. We emphasize that since the local eigenvalue problems near each spot are decoupled for the case of locally non-radially symmetric perturbations, the onset of spot self-replication behavior only depends on the source strength of an individual spot. Therefore, given any initial spatial configuration of spots at  $t = 0$ , we need only solve the nonlinear algebraic system for  $S_j, j = 1, \dots, k$  at  $t = 0$  to predict that the  $j^{\text{th}}$  spot undergoes splitting

starting at  $t = 0$  when  $S_j > \Sigma_2 \approx 4.31$ . A special asymmetric pattern that we consider in some detail in §7 is a  $k$ -spot pattern consisting of  $k - 1$  equally-spaced spots on a ring concentric within the unit disk, with an additional spot at the center of the unit disk. For  $D \gg 1$ , we use the simple explicit formula for the Neumann Green's function to explicitly predict the occurrence of dynamically-triggered spot self-replication instabilities for this special pattern.

Although the hybrid asymptotic-numerical framework developed herein to study the stability and dynamics of multi-spot quasi-equilibrium patterns for the GS model (1.1) is related to that initiated for the Schnakenburg model in [38], there are some key differences in the analysis and in the results obtained. The primary difference between these two models is that the GS model (1.1) admits three types of instability mechanisms, whereas only spot self-replication instabilities can occur for the Schnakenburg model of [38] when  $D = \mathcal{O}(1)$ . In addition, in contrast to our study in §5 of one- and two-spot patterns to the GS model on the infinite plane, the Schnakenburg model of [38] is ill-posed in  $\mathbb{R}^2$ . Finally, our results for the GS model (1.1) show that there is a wide parameter range and many simple spot configurations for which we can theoretically predict the occurrence of dynamically-triggered instabilities due to either competition, oscillation, or splitting. These dynamically-triggered bifurcation events can occur even within the very simple context of a multi-spot pattern with a common source strength. For these special patterns, such instabilities cannot occur for the Schnakenburg model.

Finally, although this paper focuses only on the study of spot patterns, we remark that the GS model (1.1) supports patterns of increasing complexity as the feed-rate parameter  $A$  increases. In particular, in the range  $\mathcal{O}(\varepsilon^{1/2}) \ll A \ll \mathcal{O}(1)$ , the GS model (1.1) with  $D = \mathcal{O}(1)$  on a two-dimensional domain does not admit spots, but instead allows for solutions for which  $v$  concentrates on a higher dimensional set such as on a one-dimensional stripe or a one-dimensional ring inside a two-dimensional domain. A stability analysis of a planar stripe inside a square domain or a concentric ring inside a disk was given in [41] and in [37].

## 2 $K$ -Spot Quasi-Equilibrium Solutions

We first construct a  $k$ -spot quasi-equilibrium solution to (1.1) by using the method of matched asymptotic expansions. We denote the center of the  $j^{\text{th}}$  spot by  $\mathbf{x}_j = (x_j, y_j) \in \Omega$  for  $j = 1, \dots, k$ . We assume that the spots are well-separated in the sense that  $|\mathbf{x}_i - \mathbf{x}_j| = \mathcal{O}(1)$  for  $i \neq j$ , and  $\text{dist}(\mathbf{x}_j, \partial\Omega) = \mathcal{O}(1)$  for  $j = 1, \dots, k$ . In an  $\mathcal{O}(\varepsilon)$  neighborhood near the  $j^{\text{th}}$  spot, we get  $v = \mathcal{O}(\varepsilon^{-1})$  and  $u = \mathcal{O}(\varepsilon)$ . Thus, we introduce the local variables  $U_j, V_j$ , and  $\mathbf{y}$ , defined by

$$u = \frac{\varepsilon}{A\sqrt{D}}U_j, \quad v = \frac{\sqrt{D}}{\varepsilon}V_j, \quad \mathbf{y} = \varepsilon^{-1}(\mathbf{x} - \mathbf{x}_j). \quad (2.1)$$

In terms of these local variables, (1.1) transforms to

$$\Delta_{\mathbf{y}}V_j - V_j + U_jV_j^2 = 0, \quad \Delta_{\mathbf{y}}U_j - U_jV_j^2 + \frac{\varepsilon A}{\sqrt{D}} - \frac{\varepsilon^2}{D}U_j = 0, \quad \mathbf{y} \in \mathbb{R}^2. \quad (2.2)$$

We look for a radially symmetric solution to (2.2) of the form  $U_j = U_j(\rho)$  and  $V_j = V_j(\rho)$ , where  $\rho \equiv |\mathbf{y}|$ . Then, to leading order in  $\varepsilon$ ,  $U_j$  and  $V_j$  are the solutions to the radially symmetric problem

$$U_j'' + \frac{1}{\rho}U_j' - U_jV_j^2 = 0, \quad V_j'' + \frac{1}{\rho}V_j' - V_j + U_jV_j^2 = 0, \quad 0 < \rho < \infty, \quad (2.3a)$$

$$V_j'(0) = 0, \quad U_j'(0) = 0; \quad V_j(\rho) \rightarrow 0, \quad U_j(\rho) \sim S_j \ln \rho + \chi(S_j) + o(1), \quad \text{as } \rho \rightarrow \infty. \quad (2.3b)$$

This leading-order coupled inner problem is referred to as the *core problem*, and is the same as that derived in [38] for the Schnakenburg model. We refer to  $S_j$  as the *source strength* of the  $j^{\text{th}}$  spot. From the divergence theorem, it

follows from the  $U_j$  equation in (2.3) that  $S_j = \int_0^\infty U_j V_j^2 \rho d\rho > 0$ . In the far-field behavior (2.3 b) for  $U_j$ , the constant  $\chi$  is a nonlinear function of the source strength  $S_j$ , which must be computed numerically from the solution to (2.3).

The solution to (2.3) is calculated numerically for a range of values of  $S_j > 0$  by using the BVP solver COLSYS (cf. [2]). In Fig. 1, we plot  $\chi(S_j)$ ,  $V_j(0)$  versus  $S_j$ , and  $V_j(\rho)$  for a few different values of  $S_j$ . For  $S_j > S_v \approx 4.78$ , the profile  $V_j(\rho)$  has a volcano shape, whereby the maximum of  $V_j$  occurs at some  $\rho > 0$ . These computations give numerical evidence to support the conjecture that there is a unique solution to (2.3) for each  $S_j > 0$ .

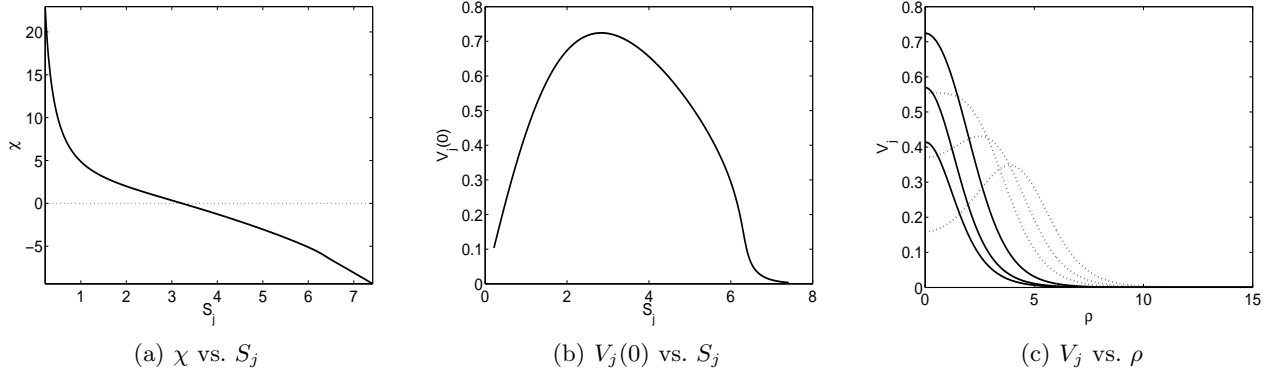


Figure 1. Numerical results for the core problem (2.3) (a) The function  $\chi$  vs.  $S_j$ ; (b)  $V_j(0)$  vs.  $S_j$ ; (c) The spot profile  $V_j(\rho)$  for  $S_j = 0.94, 1.45, 2.79$  (solid curves where  $V_j(0)$  is the maximum of  $V_j(\rho)$ ), and the volcano profile  $V_j(\rho)$  for  $S_j = 4.79, 5.73, 6.29$  (the dotted curves correspond to cases where the maximum of  $V_j(\rho)$  occurs for  $\rho > 0$ ).

Since  $v$  is localized near each  $\mathbf{x}_j$  for  $j = 1, \dots, k$ , and is exponentially small in the outer region away from the spot centers, the effect of the nonlinear term  $uv^2$  in the outer region can be calculated in the sense of distributions as  $uv^2 \sim \varepsilon^2 \sum_{j=1}^k \left( \int_{\mathbb{R}^2} \sqrt{D} (A\varepsilon)^{-1} U_j V_j^2 dy \right) \delta(\mathbf{x} - \mathbf{x}_j) \sim 2\pi\varepsilon\sqrt{D}A^{-1} \sum_{j=1}^k S_j \delta(\mathbf{x} - \mathbf{x}_j)$ . Therefore, in the quasi-steady limit, the outer problem for  $u$  from (1.1) is

$$D\Delta u + (1 - u) = \frac{2\pi\sqrt{D}\varepsilon}{A} \sum_{j=1}^k S_j \delta(\mathbf{x} - \mathbf{x}_j), \quad \mathbf{x} \in \Omega; \quad \partial_n u = 0, \quad \mathbf{x} \in \partial\Omega, \quad (2.4 a)$$

$$u \sim \frac{\varepsilon}{A\sqrt{D}} \left( S_j \ln |\mathbf{x} - \mathbf{x}_j| - S_j \ln \varepsilon + \chi(S_j) \right), \quad \text{as } \mathbf{x} \rightarrow \mathbf{x}_j, \quad j = 1, \dots, k. \quad (2.4 b)$$

The singularity condition (2.4 b) for  $u$  as  $\mathbf{x} \rightarrow \mathbf{x}_j$  was derived by matching the outer solution for  $u$  to the far-field behavior (2.3 b) of the core solution, and by recalling  $u = \varepsilon U_j / (A\sqrt{D})$  from (2.1). The problem (2.4) suggests that we introduce new variables  $\mathcal{A} = \mathcal{O}(1)$  and  $\nu \ll 1$  defined by

$$\nu = -1/\ln \varepsilon, \quad \mathcal{A} = \nu A\sqrt{D}/\varepsilon = A\sqrt{D}/[-\varepsilon \ln \varepsilon]. \quad (2.5)$$

In terms of these new variables, (2.4) transforms to

$$\Delta u + \frac{(1 - u)}{D} = \frac{2\pi\nu}{\mathcal{A}} \sum_{j=1}^k S_j \delta(\mathbf{x} - \mathbf{x}_j), \quad \mathbf{x} \in \Omega; \quad \partial_n u = 0, \quad \mathbf{x} \in \partial\Omega, \quad (2.6 a)$$

$$u \sim \frac{1}{\mathcal{A}} [S_j \nu \ln |\mathbf{x} - \mathbf{x}_j| + S_j + \nu\chi(S_j)], \quad \text{as } \mathbf{x} \rightarrow \mathbf{x}_j, \quad j = 1, \dots, k. \quad (2.6 b)$$

We emphasize that the singularity behavior in (2.6 b) specifies both the strength of the logarithmic singularity for  $u$  and the regular, or non-singular, part of this behavior. This pre-specification of the regular part of this singularity behavior at each  $\mathbf{x}_j$  will yield a nonlinear algebraic system for the source strengths  $S_1, \dots, S_k$ .



The solution to (2.6) is represented as  $u = 1 - \sum_{i=1}^k 2\pi\nu\mathcal{A}^{-1}S_i G(\mathbf{x}; \mathbf{x}_i)$ , where  $G(\mathbf{x}; \mathbf{x}_i)$  is the reduced-wave Green's function defined by (1.2). By expanding  $u$  as  $\mathbf{x} \rightarrow \mathbf{x}_j$ , and then equating the resulting expression with the required singularity behavior in (2.6 b), we obtain the following nonlinear algebraic system for  $S_1, \dots, S_k$ :

$$\mathcal{A} = S_j(1 + 2\pi\nu R_{j,j}) + \nu\chi(S_j) + 2\pi\nu \sum_{\substack{i=1 \\ i \neq j}}^k S_i G(\mathbf{x}_j; \mathbf{x}_i), \quad j = 1, \dots, k. \quad (2.7)$$

Given the GS parameters  $A$ ,  $\varepsilon$  and  $D$ , we first calculate  $\mathcal{A}$  and  $\nu$  from (2.5), and then solve (2.7) numerically for the source strengths  $S_1, \dots, S_k$ . With  $S_j$  known, the quasi-equilibrium solution in each inner region is determined from (2.3). As a remark, since  $\mathcal{A} = \mathcal{O}(1)$ , then  $A = \mathcal{O}(-\varepsilon \ln \varepsilon)$  from (2.5). Therefore, the error made in approximating (2.2) by (2.3) in the inner region is of the order  $\mathcal{O}(-\varepsilon^2 \ln \varepsilon)$ . We summarize our result as follows:

**Principal Result 2.1:** *For  $\varepsilon \rightarrow 0$  assume that  $A = \mathcal{O}(-\varepsilon \ln \varepsilon)$ , and define  $\nu$  and  $\mathcal{A}$  by  $\nu = -1/\ln \varepsilon$  and  $\mathcal{A} = \nu A \sqrt{D}/\varepsilon$ , where  $\mathcal{A} = \mathcal{O}(1)$ . Then, the solution  $v$  and the outer solution for  $u$ , corresponding to a  $k$ -spot quasi-equilibrium solution of the GS model (1.1), are given asymptotically by*

$$u(\mathbf{x}) \sim 1 - \frac{2\pi\nu}{\mathcal{A}} \sum_{j=1}^k S_j G(\mathbf{x}; \mathbf{x}_j), \quad v(\mathbf{x}) \sim \frac{\sqrt{D}}{\varepsilon} \sum_{j=1}^k V_j(\varepsilon^{-1}|\mathbf{x} - \mathbf{x}_j|). \quad (2.8 a)$$

Moreover, the inner solution for  $u$ , defined in an  $\mathcal{O}(\varepsilon)$  neighborhood of the  $j^{\text{th}}$  spot, is

$$u(\mathbf{x}) \sim \frac{\nu}{\mathcal{A}} U_j(\varepsilon^{-1}|\mathbf{x} - \mathbf{x}_j|). \quad (2.8 b)$$

Here  $\mathbf{x}_1, \dots, \mathbf{x}_k$  is the spatial configuration of the centers of the spots, and  $G(\mathbf{x}; \mathbf{x}_j)$  is the reduced-wave Green's function satisfying (1.2). In (2.8), each spot profile  $V_j(\rho)$  and  $U_j(\rho)$  for  $j = 1, \dots, k$  satisfies the coupled BVP system (2.3), where the source strength  $S_j$  in (2.3 b) is to be calculated from the nonlinear algebraic system (2.7).

We emphasize that the nonlinear algebraic system (2.7) determines the source strengths  $S_j$  for  $j = 1, \dots, k$  to within an error smaller than any power of  $\nu = -1/\ln \varepsilon$ . As such, our construction of the quasi-equilibrium pattern is accurate to all orders in  $\nu$ . Similar techniques for summing logarithmic expansions in the context of *linear* elliptic PDE's or eigenvalue problems in two-dimensional perforated domains containing small holes have been developed in a variety of contexts (cf. [57], [32], [13], [49]). Our construction here of a quasi-equilibrium solution for the GS model (1.1) extends this previous methodology for treating logarithmic expansions to an RD system for which the local problem is nonlinear with a logarithmic far-field behavior. The nonlinear algebraic system (2.7) for the source strengths is the mechanism through which the spots interact and sense the presence of the domain  $\Omega$ . This global coupling mechanism, which is not of nearest-neighbor type as in the case of the exponentially weak spot interactions studied in [23] and [25], is rather significant since  $\nu = -1/\ln \varepsilon$  is not very small unless  $\varepsilon$  is extremely small.

The quasi-equilibrium solution in Principal Result 2.1 exists only when the spatial configuration of spots and the GS parameters are such that the nonlinear algebraic system (2.7) for  $S_1, \dots, S_k$  has a solution. Determining precise conditions for the solvability of this system is a difficult issue. Therefore, in §5–7 we will primarily consider spot patterns where the source strengths have a common value, for which (2.7) reduces to a scalar nonlinear equation.

Next, we derive analytical approximations for the solution to (2.7) by first re-writing (2.7) in matrix form. To do

so, we define the Green's matrix  $\mathcal{G}$ , the vector of source strengths  $\mathbf{s}$ , the vector  $\chi(\mathbf{s})$ , and the identity vector  $\mathbf{e}$  by

$$\mathcal{G} \equiv \begin{pmatrix} R_{1,1} & G_{1,2} & \cdots & G_{1,k} \\ G_{2,1} & \ddots & \ddots & \vdots \\ \vdots & \ddots & \ddots & G_{k-1,k} \\ G_{k,1} & \cdots & G_{k,k-1} & R_{k,k} \end{pmatrix}, \quad \mathbf{s} \equiv \begin{pmatrix} S_1 \\ \vdots \\ S_k \end{pmatrix}, \quad \mathbf{e} \equiv \begin{pmatrix} 1 \\ \vdots \\ 1 \end{pmatrix}, \quad \chi(\mathbf{s}) \equiv \begin{pmatrix} \chi(S_1) \\ \vdots \\ \chi(S_k) \end{pmatrix}. \quad (2.9)$$

Here  $G_{i,j} \equiv G(\mathbf{x}_i; \mathbf{x}_j)$ , and  $G_{i,j} = G_{j,i}$  by reciprocity, so that  $\mathcal{G}$  is a symmetric matrix. Then, (2.7) becomes

$$\mathcal{A}\mathbf{e} = \mathbf{s} + 2\pi\nu\mathcal{G}\mathbf{s} + \nu\chi(\mathbf{s}). \quad (2.10)$$

We will consider (2.10) for two ranges of  $D$ ;  $D = \mathcal{O}(1)$  and  $D = \mathcal{O}(\nu^{-1})$ . For  $D = \mathcal{O}(1)$ , we can obtain a two-term approximation for the source strengths in terms of  $\nu \ll 1$  by expanding  $\mathbf{s} = \mathbf{s}_0 + \nu\mathbf{s}_1 + \cdots$ . This readily yields

$$\mathbf{s} = \mathcal{A}\mathbf{e} - \nu [2\pi\mathcal{A}\mathcal{G}\mathbf{e} + \chi(\mathcal{A})\mathbf{e}] + \mathcal{O}(\nu^2). \quad (2.11)$$

Therefore, for  $\nu \ll 1$ , the leading-order approximation for  $\mathbf{s}$  is the same for all of the spots. However, the  $\mathcal{O}(\nu)$  correction term depends on the spot locations and the domain geometry.

Next, we consider (2.10) for the distinguished limit where  $D = D_0/\nu \gg 1$  with  $D_0 = \mathcal{O}(1)$ . Since the reduced-wave Green's function  $G$ , satisfying (1.2), depends on  $D$  we first must approximate it for  $D$  large. Assuming that  $\Omega$  is a bounded domain, we expand  $G$  and its regular part  $R$  for  $D \gg 1$  as

$$G \sim DG_{-1} + G_0 + \frac{1}{D}G_1 + \cdots, \quad R \sim DR_{-1} + R_0 + \frac{1}{D}R_1 + \cdots.$$

Substituting this expansion into (1.2), and collecting powers of  $D$ , we obtain that  $G_{-1}$  is constant and that

$$\Delta G_0 = G_{-1} - \delta(\mathbf{x} - \mathbf{x}_j), \quad \mathbf{x} \in \Omega; \quad \partial_n G_0 = 0, \quad \mathbf{x} \in \partial\Omega.$$

The divergence theorem then shows that  $G_{-1} = |\Omega|^{-1}$ , where  $|\Omega|$  is the area of  $\Omega$ . In addition, the divergence theorem imposed on the  $G_1$  problem enforces that  $\int_{\Omega} G_0 d\mathbf{x} = 0$ , which makes  $G_0$  unique. Next, from the singularity condition (1.2 b) for  $G$  we obtain for  $\mathbf{x} \rightarrow \mathbf{x}_j$  that  $DG_{-1} + G_0(\mathbf{x}; \mathbf{x}_j) + \cdots \sim -(2\pi)^{-1} \ln |\mathbf{x} - \mathbf{x}_j| + DR_{-1} + R_0(\mathbf{x}; \mathbf{x}_j) + \cdots$ . Since  $G_{-1} = |\Omega|^{-1}$ , we conclude that  $R_{-1} = G_{-1} = 1/|\Omega|$ . In this way, we obtain the following two-term expansion

$$R_{j,j} \sim \tilde{R}_{j,j} \equiv \frac{D}{|\Omega|} + R_{j,j}^{(N)} + \cdots, \quad G(\mathbf{x}; \mathbf{x}_j) \sim \tilde{G}(\mathbf{x}; \mathbf{x}_j) \equiv \frac{D}{|\Omega|} + G^{(N)}(\mathbf{x}; \mathbf{x}_j) + \cdots, \quad \text{for } D \gg 1. \quad (2.12)$$

Here  $G^{(N)}(\mathbf{x}; \mathbf{x}_j)$  is the Neumann Green's function with regular part  $R_{j,j}^{(N)}$ , determined from the unique solution to

$$\Delta G^{(N)} = \frac{1}{|\Omega|} - \delta(\mathbf{x} - \mathbf{x}_j), \quad \mathbf{x} \in \Omega; \quad \partial_n G^{(N)} = 0, \quad \mathbf{x} \in \partial\Omega; \quad \int_{\Omega} G^{(N)} d\mathbf{x} = 0, \quad (2.13 a)$$

$$G^{(N)}(\mathbf{x}; \mathbf{x}_j) \sim -\frac{1}{2\pi} \ln |\mathbf{x} - \mathbf{x}_j| + R_{j,j}^{(N)} + o(1), \quad \text{as } \mathbf{x} \rightarrow \mathbf{x}_j. \quad (2.13 b)$$

For the disk and the square, in Appendix A we analytically calculate both  $G(\mathbf{x}; \mathbf{x}_j)$  and its regular part  $R_{j,j}$ , as well as the Neumann Green's function  $G^{(N)}(\mathbf{x}; \mathbf{x}_j)$  and its regular part  $R_{j,j}^{(N)}$ . For the case of a one-spot solution centered at the midpoint  $\mathbf{x}_1$  of the unit square  $[0, 1] \times [0, 1]$ , we use some of the explicit formulae from Appendix A to compare the two-term approximation  $\tilde{R}_{1,1}$ , given in (2.12), with the reduced-wave regular part  $R_{1,1}$ , as computed from (A.11). These results are shown in Fig. 2. From (A.13), the two-term approximation (2.12) for large  $D$  is

$$\tilde{R}_{1,1} = D - \frac{1}{\pi} \sum_{n=1}^{\infty} \ln(1 - q^n) + \frac{1}{12} - \frac{1}{2\pi} \ln(2\pi), \quad q \equiv e^{-2\pi}. \quad (2.14)$$

A similar comparison is made in Fig. 3 for the case of a single spot located at the center  $\mathbf{x}_1 = (0, 0)$  of the unit disk. For this radially symmetric case  $R_{1,1}$  can be found explicitly, and its two-term approximation for large  $D$  is obtained from (2.12) and (A.9 b). In this way, we get

$$R_{1,1} = \frac{1}{2\pi} \left[ \frac{1}{2} \ln D + \ln 2 - \gamma_e + \frac{K_1(D^{-1/2})}{I_1(D^{-1/2})} \right], \quad \tilde{R}_{1,1} = \frac{D}{\pi} - \frac{3}{8\pi}. \quad (2.15)$$

Here  $\gamma_e \approx 0.5772$  is Euler's constant, while  $I_1(r)$  and  $K_1(r)$  are the modified Bessel functions of order one. From Fig. 2 and Fig. 3 we observe that for both domains the two-term approximation (2.12) involving the regular part of the Neumann Green's provides a decent approximation of  $R_{1,1}$  even for only moderately large values of  $D$ .

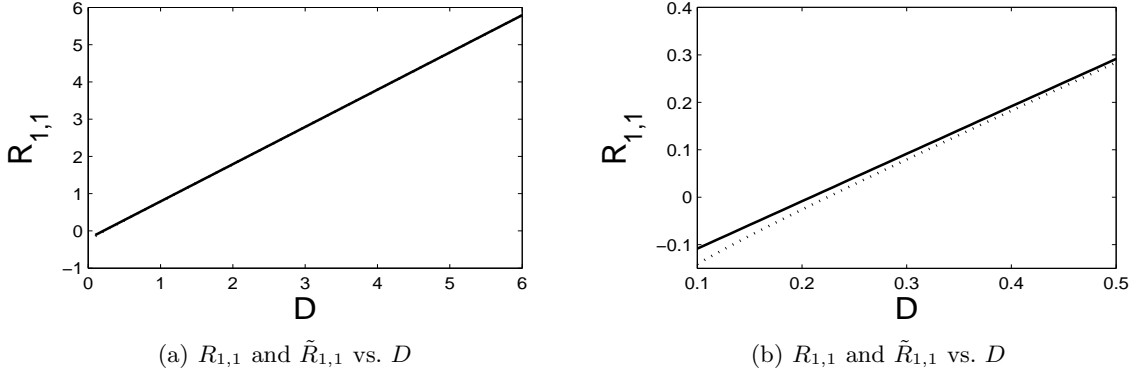


Figure 2. Consider a single spot centered at the midpoint  $\mathbf{x}_1 = (0.5, 0.5)$  of the unit square. We plot  $R_{1,1}$  vs.  $D$  (solid curve) and its two-term large  $D$  approximation  $\tilde{R}_{1,1}$  given in (2.14) (dotted curve). (a)  $D \in [0.1, 6]$ ; (b)  $D \in [0.1, 0.5]$ .

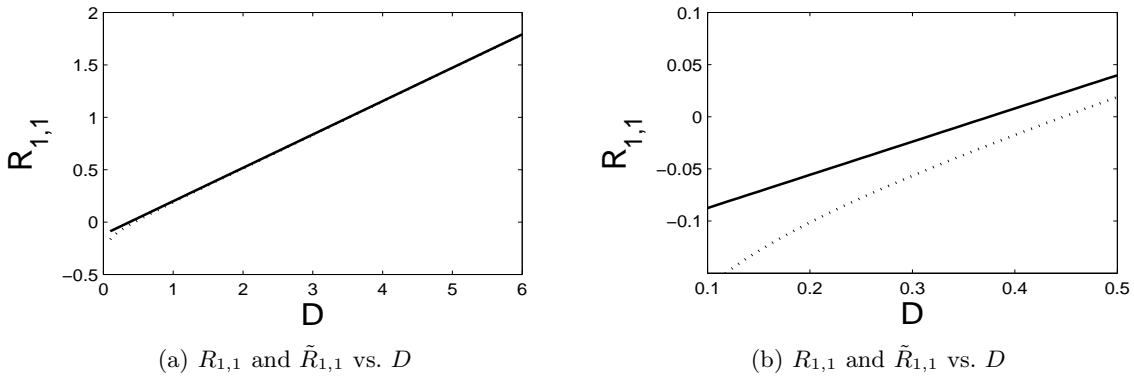


Figure 3. Consider a single spot located at the center  $\mathbf{x}_1 = (0, 0)$  of the unit disk. We plot  $R_{1,1}$  vs.  $D$  given in (2.15) (dotted curve) and its two-term large  $D$  approximation  $\tilde{R}_{1,1}$  given in (2.15) (solid curve). (a)  $D \in [0.1, 6]$ ; (b)  $D \in [0.1, 0.5]$ .

Next, we use the large  $D$  asymptotics to find an approximate solution to the nonlinear algebraic system (2.10) in the limit  $D = D_0/\nu \gg 1$ , where  $D_0 = \mathcal{O}(1)$  and  $\nu \ll 1$ . Upon substituting (2.12) into (2.10) we obtain

$$\mathbf{A}\mathbf{e} = \mathbf{s} + \frac{2\pi D_0}{|\Omega|} \mathbf{e} \mathbf{e}^T \mathbf{s} + 2\pi\nu \mathcal{G}^{(N)} \mathbf{s} + \nu \chi(\mathbf{s}),$$

where  $\mathcal{G}^{(N)}$  is the Green's matrix associated with the Neumann Green's function, i.e.  $\mathcal{G}_{i,j}^{(N)} = G^{(N)}(\mathbf{x}_i; \mathbf{x}_j)$  for  $i \neq j$ ,

and  $\mathcal{G}_{j,j}^{(N)} \equiv R_{j,j}^{(N)}$ . By expanding  $\mathbf{s}$  as  $\mathbf{s} = \mathbf{s}_0 + \nu \mathbf{s}_1 + \dots$  for  $\nu \ll 1$ , we then obtain that  $\mathbf{s}_0$  and  $\mathbf{s}_1$  satisfy

$$\left( I + \frac{2\pi D_0}{|\Omega|} \mathbf{e} \mathbf{e}^T \right) \mathbf{s}_0 = \mathcal{A} \mathbf{e}, \quad \left( \mathcal{I} + \frac{2\pi D_0}{|\Omega|} \mathbf{e} \mathbf{e}^T \right) \mathbf{s}_1 = -2\pi \mathcal{G}^{(N)} \mathbf{s}_0 - \chi(\mathbf{s}_0), \quad (2.16)$$

where  $I$  is the  $k \times k$  identity matrix. Since  $\mathbf{e}^T \mathbf{e} = k$ , the leading-order approximation  $\mathbf{s}_0$  shows that the source strengths have an asymptotically common value  $S_c$  given by

$$\mathbf{s}_0 = S_c \mathbf{e}, \quad S_c \equiv \frac{\mathcal{A}}{1 + \mu k}, \quad \mu \equiv \frac{2\pi D_0}{|\Omega|}. \quad (2.17)$$

The next order approximation  $\mathbf{s}_1$  from (2.16) yields

$$\mathbf{s}_1 = - \left( I + \mu \mathbf{e} \mathbf{e}^T \right)^{-1} \left( 2\pi S_c \mathcal{G}^{(N)} + \chi(S_c) \right) \mathbf{e}. \quad (2.18)$$

Since the matrix  $I + \mu \mathbf{e} \mathbf{e}^T$  is a rank-one perturbation of the identity, its inverse is readily calculated from the Sherman-Woodbury-Morrison formula as  $(I + \mu \mathbf{e} \mathbf{e}^T)^{-1} = I - \mu \mathbf{e} \mathbf{e}^T / (1 + \mu k)$ , which determines  $\mathbf{s}_1$  from (2.18). In this way, for  $D = D_0/\nu$  and  $\nu \ll 1$  we obtain the two-term expansion for  $s$  given by

$$\mathbf{s} = S_c \mathbf{e} - \left( \frac{\chi(S_c)}{1 + \mu k} \mathbf{e} + \frac{2\pi \mathcal{A}}{1 + \mu k} \left( \mathcal{G}^{(N)} - \frac{\mu F}{1 + \mu k} I \right) \mathbf{e} \right) \nu + \mathcal{O}(\nu^2). \quad (2.19)$$

Here  $S_c$  and  $\mu$  are defined in (2.17), while the scalar function  $F(\mathbf{x}_1, \dots, \mathbf{x}_k)$  is defined by

$$F(\mathbf{x}_1, \dots, \mathbf{x}_k) = \mathbf{e}^T \mathcal{G}^{(N)} \mathbf{e} = \sum_{i=1}^k \sum_{j=1}^k \mathcal{G}_{i,j}^{(N)}. \quad (2.20)$$

In contrast to the leading-order approximation in (2.11) when  $D = \mathcal{O}(1)$ , the leading-order approximation  $S_c$  in (2.19) depends on the number of spots and the area of the domain, with  $S_c$  increasing as the area  $|\Omega|$  increases.

We now illustrate our asymptotic theory for the construction of quasi-equilibria for the case of a one-spot solution centered at the midpoint of either the unit square or disk. Many additional examples of the theory are given in §5–6.

For our first example, we consider a one-spot solution with a spot located at the center  $\mathbf{x}_1 = \mathbf{0}$  of the unit disk with  $\varepsilon = 0.02$ . We fix  $D = 1$ , so that from (2.15) the regular part of the Green's function for a spot at  $\mathbf{x}_1$  is  $R_{1,1} \approx 0.1890$ . Then, (2.7) reduces to the following scalar nonlinear algebraic equation for the source strength  $S_1$  in terms of  $\mathcal{A}$ :

$$\mathcal{A} = S_1 (1 + 2\pi \nu R_{1,1}) + \nu \chi(S_1). \quad (2.21)$$

In Fig. 4(a) we plot  $\mathcal{A}$  versus  $S_1$ , showing the existence of a fold point at  $\mathcal{A}_f \approx 2.55$  corresponding to  $S_f \approx 1.01$ . Thus,  $\mathcal{A} \geq \mathcal{A}_f$  is required for the existence of a one-spot quasi-equilibrium solution located at the center of the unit disk. In Fig. 4(b) the asymptotic result for  $u(\mathbf{x}_1) = \nu U_1(0)/\mathcal{A}$  vs.  $\mathcal{A}$  is shown by the dotted curve, with a fold point at  $u_f(\mathbf{x}_1) \approx 0.50$ . The fold point is marked by a circle in both figures, and the critical value  $\mathcal{A}_v \approx 5.55$ ,  $u_v(\mathbf{x}_1) \approx 0.083$  for a volcano-type solution corresponding to  $S_v \approx 4.78$  is marked by a square. For  $\mathcal{A} > \mathcal{A}_f$ ,  $u(\mathbf{x}_1)$  has two solution branches. The upper branch corresponds to  $S_1 < S_f$ , while the lower branch is for the range  $S_1 > S_f$ .

To validate the asymptotic result for solution multiplicity, we solve the steady-state GS model (1.1) in the unit disk by using the Matlab BVP solver *BVP4C*. By varying  $u(0)$ , we then compute the corresponding value of  $\mathcal{A}$ . The resulting full numerical result for  $u(0)$  vs.  $\mathcal{A}$  is shown by the heavy solid curve in Fig.4(b), which essentially overlaps the asymptotic result. This shows that when  $\varepsilon = 0.02$ , the asymptotic result for the bifurcation diagram, based on retaining all terms in powers of  $\nu$ , agrees very closely with the full numerical result.

For our second example, we consider a one-spot solution centered at the midpoint  $\mathbf{x}_1 = (0.5, 0.5)$  of the unit square  $\Omega = [0, 1] \times [0, 1]$ . We fix  $\varepsilon = 0.02$  and  $D = 1$ . Then, by using (A.11) for the reduced-wave Green's function, as given

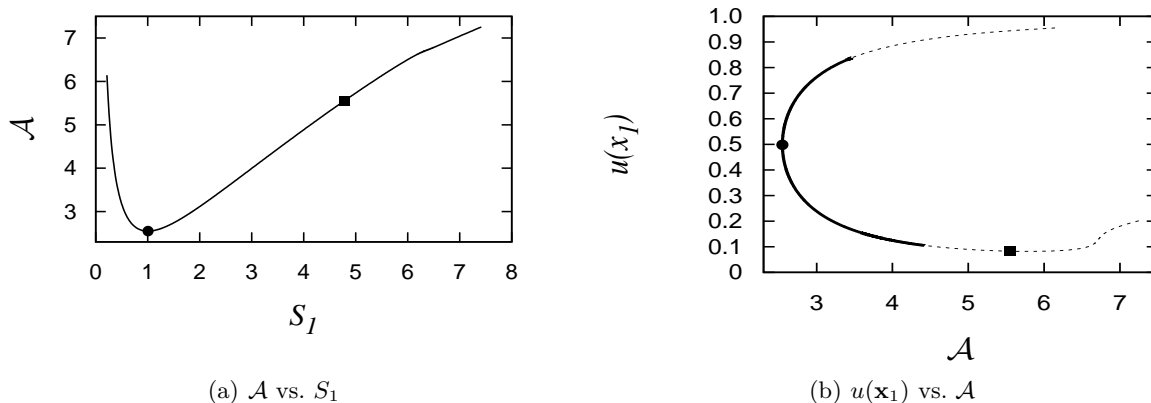


Figure 4. Let  $\Omega = \{\mathbf{x} \mid |\mathbf{x}| \leq 1\}$ ,  $\varepsilon = 0.02$ ,  $D = 1$ , and  $\mathbf{x}_1 = \mathbf{0}$ . (a)  $\mathcal{A}$  vs.  $S_1$ ; the square marks the volcano threshold  $S_v \approx 4.78$ , and the circle marks the fold point  $\mathcal{A}_f \approx 2.55$  at which  $S_f \approx 1.01$ . (b)  $u(\mathbf{x}_1)$  vs.  $\mathcal{A}$ ; the square marks  $S_v \approx 4.78$ , and the circle marks the fold point  $S_f \approx 1.01$ . The upper branch is for  $S_1 < S_f$ , and the lower branch is for  $S_1 > S_f$ .

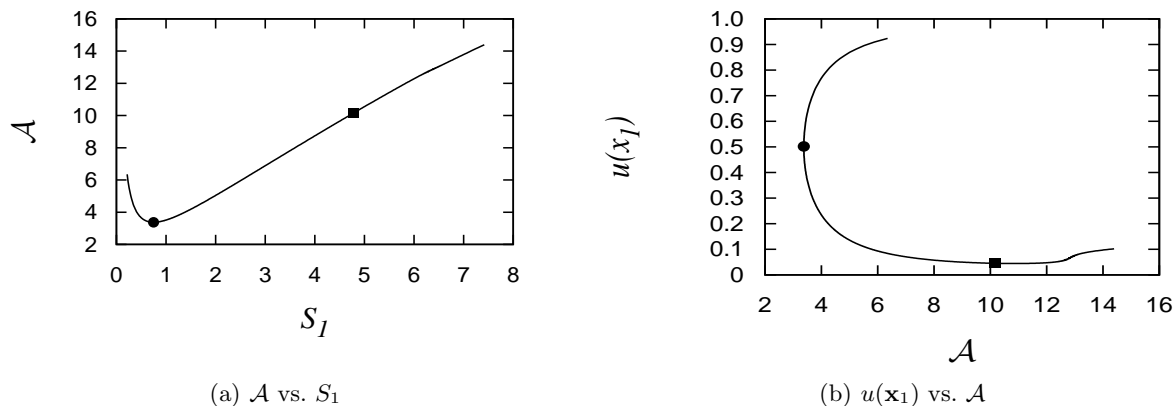


Figure 5. Let  $\Omega = [0, 1] \times [0, 1]$ ,  $\varepsilon = 0.02$ ,  $D = 1$ , and  $\mathbf{x}_1 = (0.5, 0.5)$ . (a)  $\mathcal{A}$  vs.  $S_1$ ; the square marks the volcano threshold  $S_v \approx 4.78$ , and the circle marks the fold point  $\mathcal{A}_f \approx 3.3756$  at which  $S_f \approx 0.7499$ . (b)  $u(\mathbf{x}_1)$  vs.  $\mathcal{A}$ ; the square marks  $S_v \approx 4.78$ , and the circle marks the fold point  $S_f \approx 0.7499$ . The upper branch is for  $S_1 < S_f$ , and the lower branch is for  $S_1 > S_f$ .

in Appendix A, we obtain that  $R_{1,1} \approx 0.7876$ . We remark that even if we use the two-term large  $D$  asymptotics (2.14) for the unit square, then we get the rather good estimate  $R_{1,1} \approx 0.7914$ . In Fig. 5 we use (2.21) to plot  $\mathcal{A}$  versus  $S_1$  and  $u(\mathbf{x}_1) = \nu U_1(0)/\mathcal{A}$  versus  $\mathcal{A}$ . For  $\mathcal{A} > \mathcal{A}_f \approx 3.376$ ,  $u(\mathbf{x}_1)$  versus  $\mathcal{A}$  has two solution branches, with the upper branch corresponds to  $S_1 < S_f \approx 0.750$  and the lower branch for  $S_1 > S_f$ . In contrast to the previous example for the unit disk, where the full GS model (1.1) is reduced to a coupled set of BVP for ODE's, we cannot readily verify this asymptotic result for solution multiplicity in a square from a full numerical solution of (1.1).

## 2.1 Symmetric Spot Patterns and a Circulant Matrix

A special case for multi-spot patterns, which features prominently in §4–7 below, is when the spatial configuration  $\mathbf{x}_1, \dots, \mathbf{x}_k$  of spots within  $\Omega$  is sufficiently symmetric so that the Green's matrix  $\mathcal{G}$  is a circulant matrix.

When  $\mathcal{G}$  is circulant, then it has the eigenpair  $\mathcal{G}\mathbf{e} = \theta\mathbf{e}$ , where  $\theta = k^{-1} \sum_{i=1}^k \sum_{j=1}^k (\mathcal{G})_{i,j}$ . For this special case,

(2.10) has a solution for which the spots have a common source strength  $S_j = S_c$  for  $j = 1, \dots, k$ , where  $S_c$  is the solution to the single nonlinear algebraic equation

$$\mathcal{A} = S_c + 2\pi\nu\theta S_c + \nu\chi(S_c). \quad (2.22)$$

For  $\nu \ll 1$ , a two-term approximation for this common source strength  $S_c$  is

$$S_c = \mathcal{A} - \nu [2\pi\theta\mathcal{A} + \chi(\mathcal{A})] + \mathcal{O}(\nu^2). \quad (2.23)$$

For the distinguished limit  $D = \mathcal{O}(\nu^{-1})$ , and with  $\mathcal{G}$  a circulant matrix, we calculate from (2.19) that a two-term asymptotic approximation for the source strengths is given in terms of  $F(\mathbf{x}_1, \dots, \mathbf{x}_k)$ , as defined in (2.20), by

$$\mathbf{s} = S_c \mathbf{e} - \nu \left( \frac{\chi(S_c)}{1 + \mu k} + \frac{2\pi\mathcal{A}\theta^{(N)}}{(1 + \mu k)^2} \right) \mathbf{e} + \mathcal{O}(\nu^2), \quad S_c \equiv \frac{\mathcal{A}}{1 + \mu k}, \quad \mu \equiv \frac{2\pi D_0}{|\Omega|}, \quad (2.24)$$

Here  $\theta^{(N)} = F/k$  is the eigenvalue for the eigenvector  $\mathbf{e}$  of the circulant Neumann Green's matrix  $\mathcal{G}^{(N)}$ .

Owing to the fact that the nonlinear algebraic system (2.10) can be reduced to the scalar nonlinear problem (2.22) when the Green's matrix is circulant, in the majority of our numerical experiments for multi-spot patterns in §5–§7 below we will consider  $k$ -spot quasi-equilibrium patterns that lead to this special matrix structure.

### 3 The Slow Dynamics of a Collection of Spots

In this section we derive the slow dynamics for the spot locations corresponding to a  $k$ -spot quasi-equilibrium solution of the GS model (1.1). At each fixed time  $t$ , the spatial profile of the spot pattern is characterized as in Principal Result 2.1. In the inner region near the  $j^{\text{th}}$  spot, we introduce  $\mathbf{y} = \varepsilon^{-1} [\mathbf{x} - \mathbf{x}_j(\xi)]$ , where  $\xi \equiv \varepsilon^2 t$  is the slow time variable, and we expand the inner solution as

$$u = \frac{\varepsilon}{A\sqrt{D}} (U_{0j}(\rho) + \varepsilon U_{1j}(\mathbf{y}) + \dots), \quad v = \frac{\sqrt{D}}{\varepsilon} (V_{0j}(\rho) + \varepsilon V_{1j}(\mathbf{y}) + \dots). \quad (3.1)$$

Here the subscript 0 in  $U_{0j}, V_{0j}$  denotes the order of the expansion, while  $j$  denotes the  $j^{\text{th}}$  inner region. In the analysis below we omit the subscript  $j$  if there is no confusion in the notation. The leading-order terms  $U_{0j}$  and  $V_{0j}$  are solutions of the core problem (2.3). Define  $\mathbf{w}_j \equiv (V_{1j}, U_{1j})^T$ , where  $T$  denotes transpose. At next order, we get from (3.1) and (1.1) that  $\mathbf{w}_j$  satisfies

$$\Delta_{\mathbf{y}} \mathbf{w}_j + \mathcal{M}_j \mathbf{w}_j = \mathbf{g}_j, \quad \mathbf{y} \in \mathbb{R}^2; \quad \mathcal{M}_j \equiv \begin{pmatrix} -1 + 2U_0 V_0 & V_0^2 \\ -2U_0 V_0 & -V_0^2 \end{pmatrix}, \quad \mathbf{g}_j \equiv \begin{pmatrix} -V_0' \mathbf{x}_j' \cdot \mathbf{e}_\theta \\ 0 \end{pmatrix}. \quad (3.2)$$

In (3.2),  $\cdot$  denotes dot product, and  $\mathbf{e}_\theta \equiv (\cos \theta, \sin \theta)^T$ , where  $\theta$  is the polar angle for the vector  $(\mathbf{x} - \mathbf{x}_j)$ .

To determine the dynamics of the spots we must calculate the gradient terms in the local expansion of the outer solution for  $u$ , as given in (2.8), in the limit  $\mathbf{x} \rightarrow \mathbf{x}_j$ . To do so, we must calculate a further term in the local behavior as  $\mathbf{x} \rightarrow \mathbf{x}_j$  of the reduced-wave Green's function satisfying (1.2). In terms of the inner variable  $\mathbf{y}$ , we get

$$G(\mathbf{x}; \mathbf{x}_j) \sim -\frac{1}{2\pi} \ln |\mathbf{y}| + R_{j,j} + \varepsilon \nabla R(\mathbf{x}_j; \mathbf{x}_j) \cdot \mathbf{y} + \dots,$$

where we have defined  $\nabla R(\mathbf{x}_j; \mathbf{x}_j) \equiv \nabla_{\mathbf{x}} R(\mathbf{x}; \mathbf{x}_j) \Big|_{\mathbf{x}=\mathbf{x}_j}$ . By comparing the higher-order terms in the matching condition between the inner expansion (3.1) for  $u$  and the outer expansion for  $u$ , we obtain the required far-field behavior

as  $|\mathbf{y}| \rightarrow \infty$  of the inner solution  $U_{1j}$ . In this way, we obtain that  $\mathbf{w}_j$  satisfies (3.2) with far-field behavior

$$\mathbf{w}_j \rightarrow \begin{pmatrix} 0 \\ -\mathbf{f}_j \cdot \mathbf{y} \end{pmatrix}, \quad \text{as } \mathbf{y} \rightarrow \infty, \quad \mathbf{f}_j = \begin{pmatrix} f_{j1} \\ f_{j2} \end{pmatrix} \equiv 2\pi \left( S_j \nabla R(\mathbf{x}_j; \mathbf{x}_j) + \sum_{\substack{i=1 \\ i \neq j}}^k S_i \nabla G(\mathbf{x}_j; \mathbf{x}_i) \right). \quad (3.3)$$

To determine the dynamics of the  $j^{\text{th}}$  spot we must formulate the solvability condition for (3.2) and (3.3). We define  $\hat{P}_j^*(\rho) = (\hat{\phi}_j^*(\rho), \hat{\psi}_j^*(\rho))^T$  to be the radially symmetric solution of the adjoint problem

$$\Delta_\rho \hat{P}_j^* + \mathcal{M}_j^T \hat{P}_j^* = 0, \quad 0 < \rho < \infty, \quad (3.4)$$

subject to the far-field condition that  $\hat{P}_j^* \rightarrow (0, 1/\rho)^T$  as  $\rho \rightarrow \infty$ , where  $\Delta_\rho \equiv \partial_{\rho\rho} + \rho^{-1} \partial_\rho - \rho^{-2}$ . We look for solutions  $P_j^c$  and  $P_j^s$  to the homogeneous adjoint problem  $\Delta_{\mathbf{y}} P_j^* + \mathcal{M}_j^T P_j^* = 0$  for  $\mathbf{y} \in \mathbb{R}^2$  in the form  $P_j^* = P_j^c \equiv \hat{P}_j^* \cos \theta$  and  $P_j^* = P_j^s \equiv \hat{P}_j^* \sin \theta$ , where  $\hat{P}_j^*(\rho)$  is the radially symmetric solution of (3.4).

In terms of the adjoint solution  $P_j^c$ , the solvability condition for (3.2), subject to (3.3), is that

$$\lim_{\sigma \rightarrow \infty} \int_{B_\sigma} P_j^c \cdot \mathbf{g}_j \, d\mathbf{y} = \lim_{\sigma \rightarrow \infty} \int_{\partial B_\sigma} \left[ P_j^c \cdot \partial_\rho \mathbf{w}_j - \mathbf{w}_j \cdot \partial_\rho P_j^c \right] \Big|_{\rho=\sigma} \, d\mathbf{y}. \quad (3.5)$$

Here  $B_\sigma$  is a ball of radius  $\sigma$ , i.e.  $|\mathbf{y}| = \sigma$ . Upon using the far-field condition (3.3), and writing  $\mathbf{x}_j = (x_{j1}, x_{j2})^T$  in component form, we reduce (3.5) to

$$x'_{j1} \int_0^{2\pi} = \int_0^\infty \hat{\phi}_j^* V_0' \cos^2 \theta \, \rho \, d\rho \, d\theta - x'_{j2} \int_0^{2\pi} \int_0^\infty \hat{\phi}_j^* V_0' \cos \theta \sin \theta \, \rho \, d\rho \, d\theta = \lim_{\sigma \rightarrow \infty} \int_0^{2\pi} \left( \frac{2 \cos \theta}{\sigma} \mathbf{f}_j \cdot \mathbf{e}_\theta \right) \sigma \, d\theta. \quad (3.6)$$

Therefore, since  $\int_0^{2\pi} \cos \theta \sin \theta \, d\theta = 0$ , we obtain  $dx_{j1}/d\xi = 2f_{j1}/\left(\int_0^\infty \hat{\phi}_j^* V_0' \rho \, d\rho\right)$ . Similarly, the solvability condition for (3.2), subject to (3.3), with respect to the homogeneous adjoint solution  $P_j^s$ , yields  $dx_{j2}/d\xi = 2f_{j2}/\left(\int_0^\infty \hat{\phi}_j^* V_0' \rho \, d\rho\right)$ . Upon recalling the definition of  $(f_{j1}, f_{j2})^T$  in (3.3), we can summarize our result for the slow dynamics as follows:

**Principal Result 3.1:** *Consider the GS model (1.1) with  $\varepsilon \ll 1$ ,  $A = \mathcal{O}(-\varepsilon \ln \varepsilon)$ , and  $\tau \ll \mathcal{O}(\varepsilon^{-2})$ . Then, provided that each spot is stable to any profile instability, the slow dynamics of a collection  $\mathbf{x}_1, \dots, \mathbf{x}_k$  of spots satisfies the differential-algebraic (DAE) system*

$$\frac{d\mathbf{x}_j}{dt} \sim -2\pi\varepsilon^2 \gamma(S_j) \left( S_j \nabla R(\mathbf{x}_j; \mathbf{x}_j) + \sum_{\substack{i=1 \\ i \neq j}}^k S_i \nabla G(\mathbf{x}_j; \mathbf{x}_i) \right), \quad j = 1, \dots, k; \quad \gamma(S_j) \equiv \frac{-2}{\int_0^\infty \hat{\phi}_j^* V_0' \rho \, d\rho}. \quad (3.7)$$

In (3.7), the source strengths  $S_j$ , for  $j = 1, \dots, k$ , are determined in terms of the instantaneous spot locations and the parameters  $\mathcal{A}$  and  $\nu$  of (2.5) by the nonlinear algebraic system (2.7). In the definition of  $\gamma(S_j)$ ,  $V_0$  satisfies the core problem (2.3), while  $\hat{\phi}_j^*$  is the first component of the solution to the radially symmetric adjoint problem (3.4). Finally, the equilibrium spot locations  $\mathbf{x}_{je}$  and spot strengths  $S_{je}$ , for  $j = 1, \dots, k$ , satisfy

$$S_{je} \nabla R(\mathbf{x}_{je}; \mathbf{x}_{je}) + \sum_{\substack{i=1 \\ i \neq j}}^k S_{ie} \nabla G(\mathbf{x}_{je}; \mathbf{x}_{ie}) = 0, \quad j = 1, \dots, k, \quad (3.8)$$

subject to the nonlinear algebraic system (2.7), which relates the source strengths to the spot locations.

The ODE system (3.7) coupled to the nonlinear algebraic system (2.7) constitutes a DAE system for the time-dependent spot locations  $\mathbf{x}_j$  and source strengths  $S_j$  for  $j = 1, \dots, k$ . These collective coordinates evolve slowly over a long time-scale of order  $t = \mathcal{O}(\varepsilon^{-2})$ , and characterizes the slow evolution of the quasi-equilibrium pattern. From

a numerical computation of  $\hat{\phi}_j^*$ , the function  $\gamma(S_j)$  in (3.7) was previously computed numerically in Fig. 3 of [38], where it was shown that  $\gamma(S_j) > 0$  when  $S_j > 0$ . This plot is reproduced below in Fig. 10(b). In §7 we will compare the dynamics (3.7) with corresponding full numerical results for different spot patterns in the unit square.

We emphasize that the DAE system in Principal Result 3.1 for the slow spot evolution is only valid if each spot is stable to any spot profile instability that occurs on a fast  $\mathcal{O}(1)$  time-scale. One such spot profile instability is the peanut-splitting instability, studied below in §4.1, that is triggered whenever  $S_J > \Sigma_2 \approx 4.31$  for some  $J \in \{1, \dots, k\}$ . The other profile instabilities are locally radially symmetric instabilities and, roughly speaking, consist of a temporal oscillation of the spot amplitude if  $\tau$  is sufficiently large, or a spot over-crowding competition instability, which is triggered when either the spots are too closely spaced or, equivalently, when  $D$  is too large. A new global eigenvalue problem characterizing these latter two types of instabilities is formulated in §4.2.

For the equilibrium problem (3.8), it is analytically intractable to determine all possible equilibrium solution branches for  $k$ -spot patterns in an arbitrary two-dimensional domain as the parameters  $\mathcal{A}$  and  $D$  are varied. However, some partial analytical results are obtained in §6 for the special case of  $k$  spots equally spaced on a circular ring that lies within, and is concentric with, a circular disk domain. For this special case, the Green's matrix in (2.10) is circulant, and the equilibrium problem is reduced to determining the equilibrium ring radius for the pattern.

For the related Schnakenburg model, it was shown in §2.4 of [38] that near the spot self-replication threshold, i.e. for  $S_j$  near  $\Sigma_2$ , the direction at which the spot splits is always perpendicular to the direction of the motion of the spot. This result was derived in [38] from a center-manifold type calculation involving the four dimensional eigenspace associated with the two independent translation modes and the two independent directions of splitting. Since this calculation in [38] involves only the inner region near an individual spot, it also applies directly to the GS model (1.1). This qualitative result is stated as follows:

**Principal Result 3.2:** *Consider the GS model (1.1) with  $\varepsilon \ll 1$ ,  $A = \mathcal{O}(-\varepsilon \ln \varepsilon)$ , and  $\tau \ll \mathcal{O}(\varepsilon^{-2})$ . Suppose that  $S_J > \Sigma_2$ , with  $S_J - \Sigma_2 \rightarrow 0^+$  for some unique index  $J$  in the set  $j = 1, \dots, k$ . Then, the direction of splitting of the  $J^{\text{th}}$  spot is perpendicular to the direction of its motion.*

#### 4 Fast Instabilities of the Quasi-Equilibrium Spot Pattern

In this section we study the stability of a  $k$ -spot quasi-equilibrium pattern to either competition, oscillatory, or self-replication, instabilities that can occur on a fast  $\mathcal{O}(1)$  time-scale relative to the slow motion, of speed  $\mathcal{O}(\varepsilon^2)$ , of the spot locations. The stability analysis below with regards to spot self-replication is similar to that done in [38] for the Schnakenburg model. The formulation of a globally coupled eigenvalue problem governing competition and oscillatory instabilities is a new result.

Let  $u_e$  and  $v_e$  denote the quasi-equilibrium solution of Principal Result 2.1. We introduce the perturbation

$$u(\mathbf{x}, t) = u_e + e^{\lambda t} \eta(\mathbf{x}), \quad v(\mathbf{x}, t) = v_e + e^{\lambda t} \phi(\mathbf{x}),$$

for a fixed spatial configuration  $\mathbf{x}_1, \dots, \mathbf{x}_k$  of spots. Then, from (1.1), we obtain the eigenvalue problem

$$\varepsilon^2 \Delta \phi - (1 + \lambda) \phi + 2A u_e v_e \phi + A v_e^2 \eta = 0, \quad D \Delta \eta - (1 + \tau \lambda) \eta - 2u_e v_e \phi - v_e^2 \eta = 0. \quad (4.1)$$

In the inner region near the  $j^{\text{th}}$  spot, we recall from (2.1) that  $u_e \sim \frac{\varepsilon}{A\sqrt{D}} U_j$  and  $v_e \sim \frac{\sqrt{D}}{\varepsilon} V_j$ , where  $U_j, V_j$  is the



radially symmetric solution of the core problem (2.3). Next, we define

$$\mathbf{y} = \varepsilon^{-1}(\mathbf{x} - \mathbf{x}_j), \quad \eta = \frac{\varepsilon}{A\sqrt{D}}N_j, \quad \phi = \frac{\sqrt{D}}{\varepsilon}\Phi_j, \quad (4.2)$$

so that (4.1) transforms to

$$\Delta_{\mathbf{y}}\Phi_j - (1 + \lambda)\Phi_j + 2U_jV_j\Phi_j + V_j^2N_j = 0, \quad \Delta_{\mathbf{y}}N_j - V_j^2N_j - 2U_jV_j\Phi_j = \frac{\varepsilon^2}{D}(1 + \tau\lambda)N_j. \quad (4.3)$$

Then, assuming that  $D = \mathcal{O}(1)$  and  $\tau \ll \mathcal{O}(\varepsilon^{-2})$ , we can neglect the right-hand side of the equation for  $N_j$  in (4.3).

Next, we look for angular perturbations of the form  $\Phi_j = e^{im\theta}\hat{\Phi}_j(\rho)$ ,  $N_j = e^{im\theta}\hat{N}_j(\rho)$ , where  $m \geq 0$  is a non-negative integer,  $\theta = \arg(\mathbf{y})$ , and  $\rho = |\mathbf{y}|$ . Then, from (4.3),  $\hat{N}_j(\rho)$  and  $\hat{\Phi}_j(\rho)$  satisfy

$$\hat{\Phi}_j'' + \frac{1}{\rho}\hat{\Phi}_j' - \frac{m^2}{\rho^2}\hat{\Phi}_j - (1 + \lambda)\hat{\Phi}_j + 2U_jV_j\hat{\Phi}_j + V_j^2\hat{N}_j = 0, \quad 0 < \rho < \infty, \quad (4.4a)$$

$$\hat{N}_j'' + \frac{1}{\rho}\hat{N}_j' - \frac{m^2}{\rho^2}\hat{N}_j - V_j^2\hat{N}_j - 2U_jV_j\hat{\Phi}_j = 0, \quad 0 < \rho < \infty, \quad (4.4b)$$

with boundary conditions

$$\hat{\Phi}_j'(0) = 0, \quad \hat{N}_j'(0) = 0, \quad \hat{\Phi}_j(\rho) \rightarrow 0, \quad \text{as } \rho \rightarrow \infty. \quad (4.4c)$$

Since the far-field behavior of  $\hat{N}_j$  is different for  $m = 0$  and  $m \geq 2$ , we will consider these two different cases separately below. For  $m = 1$ , which corresponds to translation invariance, it follows trivially that  $\lambda = 0$  is an eigenvalue of the local eigenvalue problem. For this translation eigenvalue, a higher-order analysis would show that  $\lambda = \mathcal{O}(\varepsilon^2)$  when  $\varepsilon \rightarrow 0$ . Since any weak instability of this type should be reflected by the properties of the Hessian of the DAE system of Principal Result 3.1 for the slow spot dynamics, the mode  $m = 1$  is not considered here.

#### 4.1 Non-Radially Symmetric Local Perturbations: Spot Self-Replication Instabilities

An instability of (4.4) for the mode  $m = 2$  is associated with the initiation of a peanut-splitting instability. Instabilities for the higher modes  $m \geq 3$  suggest the possibility of the initiation of more spatially intricate spot self-replication events. Thus, the eigenvalue problem (4.4) with angular modes  $m \geq 2$  initiate angular deformations of the spot profile. For this range of  $m$ , the linear operator for  $N_j$  in (4.4b) allows for algebraic decay of  $N_j$  as  $\rho \rightarrow \infty$  owing to the  $m^2\hat{N}_j/\rho^2$  term. As such, for  $m \geq 2$  we impose the far-field boundary condition that  $\hat{N}_j \rightarrow 0$  as  $\rho \rightarrow \infty$ .

For  $m \geq 2$ , the eigenvalue problem (4.4) is coupled to the core problem (2.3) for  $U_j$  and  $V_j$ , and can only be solved numerically. To do so, we first solve the BVP (2.3) numerically by using COLSYS (cf. [2]). Then, we discretize (4.4) by a centered difference scheme to obtain a matrix eigenvalue problem. By using the linear algebra package LAPACK [1] to compute the spectrum of this matrix eigenvalue problem, we estimate the eigenvalue  $\lambda_0$  of (4.4) with the largest real part as a function of the source strength  $S_j$  for different angular modes  $m \geq 2$ . The instability threshold occurs when  $\text{Re}(\lambda_0) = 0$ . We find numerically that  $\lambda_0$  is real when  $S_j$  is large enough. In the left subfigure of Fig. 6, we plot  $\text{Re}(\lambda_0)$  as a function of the source strength  $S_j$  for  $m = 2, 3, 4$ . Our computational results show that the instability threshold for the modes  $m \geq 2$  occurs at  $S_j = \Sigma_m$ , where  $\Sigma_2 \approx 4.31$ ,  $\Sigma_3 \approx 5.44$ , and  $\Sigma_4 \approx 6.14$ . In the right subfigure of Fig. 6, we plot the eigenfunction  $(\hat{\Phi}_j, \hat{N}_j)$  corresponding to  $\lambda_0 = 0$  with  $m = 2$  at  $S_j = \Sigma_2$ .

We emphasize that since  $\hat{N}_j \rightarrow 0$  as  $\rho \rightarrow \infty$ , the initiation of a spot self-replication instability is determined through a *local* stability analysis near the  $j^{\text{th}}$  spot. We summarize the result in the following statement:

**Principal Result 4.1:** *Consider the GS model (1.1) with  $\varepsilon \ll 1$ ,  $A = \mathcal{O}(-\varepsilon \ln \varepsilon)$ , and  $\tau \ll \mathcal{O}(\varepsilon^{-2})$ . We define*

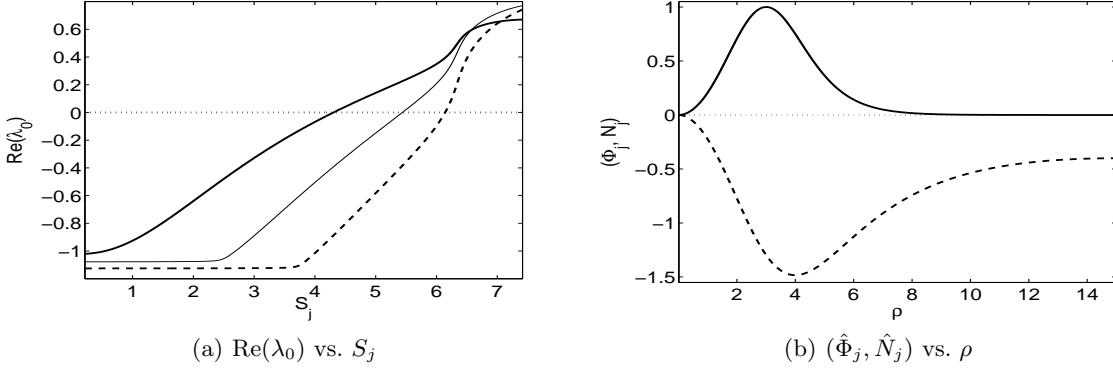


Figure 6. Numerical results for the principal eigenvalue  $\lambda_0$  of (4.4) with mode  $m \geq 2$ . (a)  $\text{Re}(\lambda_0)$  vs.  $S_j$ ; heavy solid curve is for  $m = 2$  with  $\Sigma_2 = 4.31$ , the solid curve is for  $m = 3$  with  $\Sigma_3 = 5.44$ , and the dashed curve is for  $m = 4$  with  $\Sigma_4 = 6.14$ . (b) For  $m = 2$ , the eigenfunctions  $(\hat{\Phi}_j(\rho), \hat{N}_j(\rho))$  near  $\lambda_0 = 0$  with  $S_j = \Sigma_2 \approx 4.31$  are shown. The solid curve is  $\hat{\Phi}_j(\rho)$ , and the dashed curve is  $\hat{N}_j(\rho)$ . In this subfigure the maximum value of  $\hat{\Phi}_j$  has been scaled to unity.

$\nu$  and  $\mathcal{A}$  as in (2.5). In terms of  $\mathcal{A}$ ,  $D$ , and  $\nu$ , we calculate  $S_1, \dots, S_k$  for a  $k$ -spot quasi-equilibrium pattern from the nonlinear algebraic system (2.7). Then, if  $S_j < \Sigma_2 \approx 4.31$ , the  $j^{\text{th}}$  spot is linearly stable to a spot deformation instability for modes  $m \geq 2$ . Alternatively, for  $S_j > \Sigma_2$ , it is linearly unstable to the peanut-splitting mode  $m = 2$ .

We now show numerically that the peanut-splitting linear instability leads to a nonlinear spot self-replication event. This suggests that the bifurcation as  $S_j$  increases above  $\Sigma_2$  is subcritical. To show this, we formulate a time-dependent inner, or core, problem near a single spot, defined in terms of the local inner variables

$$u = \frac{\varepsilon}{A\sqrt{D}} U(\mathbf{y}, t), \quad v = \frac{\sqrt{D}}{\varepsilon} V(\mathbf{y}, t), \quad \mathbf{y} = \varepsilon^{-1}(\mathbf{x} - \mathbf{x}_j). \quad (4.5)$$

Then, from (1.1), we obtain to leading order that  $U$  and  $V$  satisfy the time-dependent parabolic-elliptic problem

$$V_t = \Delta_{\mathbf{y}} V - V + UV^2, \quad \Delta_{\mathbf{y}} U - UV^2 = 0, \quad \mathbf{y} \in \mathbb{R}^2; \quad V \rightarrow 0, \quad U \rightarrow S \ln |\mathbf{y}|, \quad \text{as } |\mathbf{y}| \rightarrow \infty. \quad (4.6)$$

From our eigenvalue computations, based on (4.4), the radially symmetric equilibrium solution to (4.6) for  $U$  and  $V$  exhibits a peanut-splitting linear instability when  $S > \Sigma_2 \approx 4.31$ . To determine whether this linear instability leads to a nonlinear spot self-replication event when  $S > \Sigma_2$ , we use *FlexPDE* (cf. [26]) to compute solutions to (4.6) in a large disk of radius  $|\mathbf{y}| = R_m \equiv 30$ , and with initial data

$$V(\mathbf{y}, 0) = \frac{3}{2} \text{sech}^2(|\mathbf{y}|/2), \quad U(\mathbf{y}, 0) = 1 - \frac{\cosh(R_m - |\mathbf{y}|)}{\cosh R_m}. \quad (4.7)$$

The asymptotic boundary condition  $\partial_{|\mathbf{y}|} U = S/|\mathbf{y}|$  is imposed at  $|\mathbf{y}| = R_m = 30$ . We set  $S = 4.5 > \Sigma_2$ , and in Fig. 7 we plot the solution  $V$  for  $t < 300$  showing a nonlinear spot self-replication event. Owing to the rotational symmetry of this problem, the direction of spot-splitting observed in Fig. 7 is likely due to small numerical errors or grid effects. In contrast, if we choose  $S = 4.1$  and the same initial condition, then there is no spot self-replication for (4.6) (not shown). Therefore, this numerical evidence supports the conjecture that the peanut-splitting instability associated with the  $m = 2$  mode initiates a nonlinear spot self-replication event when  $S > \Sigma_2$ .

Next, we numerically investigate spot-splitting for values of  $S_j$  that well-exceed the threshold  $\Sigma_2 \approx 4.31$  for the peanut-splitting instability. From Fig. 6(a), the threshold values of  $S_j$  for higher splittings are  $\Sigma_3 \approx 5.44$  and

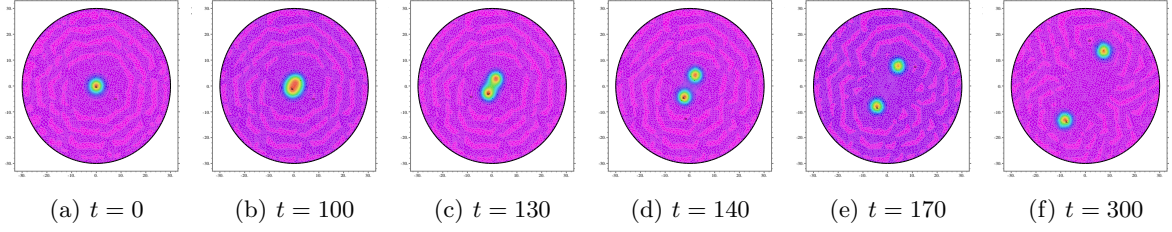


Figure 7. In a circular domain with radius  $R_m = 30$ , we compute numerical solutions to (4.6) by FlexPDE (cf. [26]) using the initial condition in (4.7). The solution  $V$  with  $S = 4.5$  is plotted at  $t = 0, 10, 100, 130, 140, 170, 300$ .

$\Sigma_4 \approx 6.14$ , corresponding to  $m = 3$  and  $m = 4$ , respectively. From Fig. 6(a) we observe that the growth rates associated with these further unstable modes are comparable to that for the mode  $m = 2$  when  $S_j \approx 6.5$ .

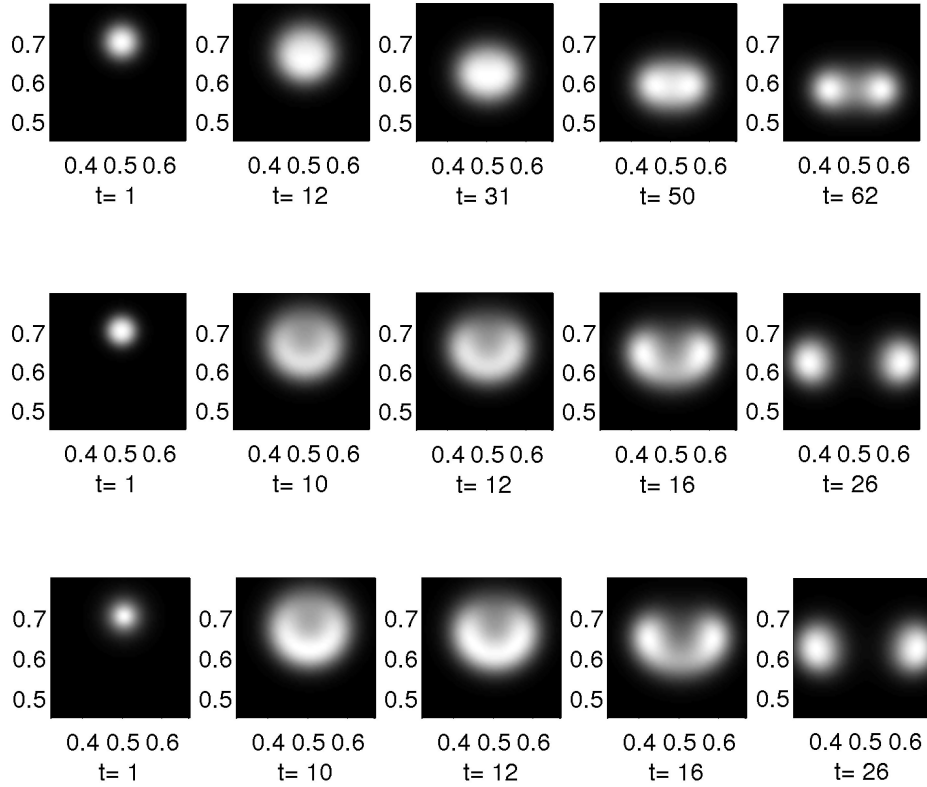


Figure 8. One-spot pattern in the unit square  $[0, 1] \times [0, 1]$ . Let  $D = 1.0$ ,  $\epsilon = 0.02$  and  $\mathbf{x}_1 = (0.5, 0.7)$ . We set  $\mathcal{A} = 9.9213$  (top row),  $\mathcal{A} = 12.643$  (middle row), and  $\mathcal{A} = 13.285$  (bottom row), so that  $S_1 \approx 4.5 > \Sigma_2$ ,  $S_1 \approx 6.0 > \Sigma_3$  and  $S_1 \approx 6.4 > \Sigma_4$ , respectively. The numerical solutions for  $v$  from (1.1) are computed using VLUGR (cf. [6]), and are plotted at different instants in time in the zoomed spatial region  $[0.325, 0.675] \times [0.45, 0.8]$ .

For illustration, we consider a one-spot pattern with  $D = 1$  and  $\epsilon = 0.02$  in the unit square  $[0, 1] \times [0, 1]$  with a spot centered at  $\mathbf{x}_1 = (0.5, 0.7)$ . From (2.21), we then calculate  $\mathcal{A}$  from  $\mathcal{A} = S_1 + 2\pi\nu R_{1,1} S_1 + \nu\chi(S_1)$ , where  $R_{1,1}$  is the regular part of the reduced-wave Green's function that can be calculated from (A.11) of Appendix A. We numerically study the spot-splitting process by using VLUGR (cf. [6]) to compute solutions to (1.1) for  $\mathcal{A} = 9.9213$ ,

$\mathcal{A} = 12.643$ , and  $\mathcal{A} = 13.285$ , corresponding to  $S_1 = 4.5 > \Sigma_2$ ,  $S_1 = 6.0 > \Sigma_3$ , and  $S_1 = 6.4 > \Sigma_4$ , respectively. The results are shown in Fig. 8 in the sub-region  $[0.325, 0.675] \times [0.45, 0.8]$ . These computations show that spot self-replication, leading to the creation of two distinct spots, is a robust phenomena for (1.1) whenever  $S_1 > \Sigma_2$ . Although for  $S_1 = 6.0$  and  $S_1 = 6.4$  the initial instability leads to a crescent pattern for the volcano profile for  $V$ , eventually two spots are created from this instability. Therefore, these numerical results support the conjecture that the unstable mode  $m = 2$  dominates any of the other unstable modes with  $m > 2$  in the weakly nonlinear regime, and eventually leads to the creation of two spots from a single spot when  $S_1 > \Sigma_2$ .

#### 4.2 Radially Symmetric Local Perturbations: Competition and Oscillatory Instabilities

In §4.1 the stability of the spot profile to locally non-radially symmetric perturbations was studied numerically. In this subsection, we examine the stability of the spot profile to locally radially symmetric perturbations of the form  $N_j = N_j(\rho)$  and  $\Phi_j = \Phi_j(\rho)$ , with  $\rho = |\mathbf{y}|$ , which characterize instabilities in the amplitudes of the spots. With the assumption that  $\tau\lambda \ll \mathbf{O}(\varepsilon^{-2}D)$ , (4.3) reduces to the following radially symmetric eigenvalue problem on  $0 < \rho < \infty$ :

$$\Phi_j'' + \frac{1}{\rho}\Phi_j' - \Phi_j + 2U_jV_j\Phi_j + V_j^2N_j = \lambda\Phi_j, \quad N_j'' + \frac{1}{\rho}N_j' - V_j^2N_j - 2U_jV_j\Phi_j = 0, \quad (4.8 a)$$

$$\Phi_j'(0) = N_j'(0) = 0; \quad \Phi_j(\rho) \rightarrow 0, \quad N_j(\rho) \rightarrow C_j \ln \rho + B_j + o(1), \quad \text{as } \rho \rightarrow \infty. \quad (4.8 b)$$

Here  $U_j$  and  $V_j$  is the radially symmetric solution of the core problem (2.3) for the  $j^{\text{th}}$  spot. From the divergence theorem, the constant  $C_j$  in (4.8 b) is given by  $C_j \equiv \int_0^\infty (2U_jV_j\Phi_j + V_j^2N_j)\rho d\rho$ . We emphasize that the operator in (4.8 a) for  $N_j$  reduces to  $N_j'' + \rho^{-1}N_j' \approx 0$  for  $\rho \gg 1$ , and so we cannot impose that  $N_j \rightarrow 0$  as  $\rho \rightarrow \infty$ . Instead, we must allow for the possibility of a logarithmic growth at infinity for  $N_j$ , as written in (4.8 b). This growth condition, which will lead to a global coupling of the  $k$  local eigenvalue problems, is in contrast to the decay condition as  $\rho \rightarrow \infty$  used in §4.1 for the stability analysis with respect to locally non-radially symmetric perturbations.

To formulate our eigenvalue problem we must match the far-field logarithmic growth of  $N_j$  with a global outer solution for  $\eta$ . This matching globally couples the local eigenvalue problems near each spot. To determine the problem for the outer solution for  $\eta$ , we use the fact that  $v$  is localized near  $\mathbf{x}_j$  for  $j = 1, \dots, k$ . Then, from (2.1) and (4.2), we represent the last two terms in the  $\eta$  equation of (4.1) in the sense of distributions to obtain that  $2uv\phi + v^2\eta \sim 2\pi\varepsilon\sqrt{D}A^{-1} \sum_{j=1}^k C_j \delta(\mathbf{x} - \mathbf{x}_j)$ , where  $C_j \equiv \int_0^\infty (2U_jV_j\Phi_j + V_j^2N_j)\rho d\rho$  and  $\delta(\mathbf{x} - \mathbf{x}_j)$  is the Dirac delta function. Therefore, in the outer region, we obtain from (4.1) that  $\eta$  satisfies

$$\Delta\eta - \frac{(1 + \tau\lambda)}{D}\eta = \frac{2\pi\varepsilon}{A\sqrt{D}} \sum_{j=1}^k C_j \delta(\mathbf{x} - \mathbf{x}_j), \quad \mathbf{x} \in \Omega; \quad \partial_n\eta = 0, \quad \mathbf{x} \in \partial\Omega. \quad (4.9)$$

This outer solution can be represented in terms of a  $\lambda$ -dependent Green's function as

$$\eta = -\frac{2\pi\varepsilon}{A\sqrt{D}} \sum_{j=1}^k C_j G_\lambda(\mathbf{x}; \mathbf{x}_j), \quad (4.10)$$

where  $G_\lambda(\mathbf{x}; \mathbf{x}_j)$  satisfies

$$\Delta G_\lambda - \frac{(1 + \tau\lambda)}{D} G_\lambda = -\delta(\mathbf{x} - \mathbf{x}_j), \quad \mathbf{x} \in \Omega; \quad \partial_n G_\lambda = 0, \quad \mathbf{x} \in \partial\Omega, \quad (4.11 a)$$

$$G_\lambda(\mathbf{x}; \mathbf{x}_j) \sim -\frac{1}{2\pi} \ln |\mathbf{x} - \mathbf{x}_j| + R_{\lambda,j,j} + o(1) \quad \text{as } \mathbf{x} \rightarrow \mathbf{x}_j. \quad (4.11 b)$$

We remark that the regular part  $R_{\lambda,j}$  of  $G_\lambda$  depends on  $\mathbf{x}_j$ ,  $D$ , and  $\tau\lambda$ .

The matching condition between the outer solution (4.10) for  $\eta$  as  $\mathbf{x} \rightarrow \mathbf{x}_j$  and the far-field behavior (4.8 b) as  $\rho \rightarrow \infty$  of the inner solution  $N_j$  near the  $j^{\text{th}}$  spot, defined in terms of  $\eta$  by (4.2), yields that

$$-\frac{2\pi\varepsilon}{A\sqrt{D}} \left[ C_j \left( -\frac{1}{2\pi} \ln|\mathbf{x} - \mathbf{x}_j| + R_{\lambda,j,j} \right) \right] - \frac{2\pi\varepsilon}{A\sqrt{D}} \sum_{i \neq j}^k C_i G_{\lambda i,j} \sim \frac{\varepsilon}{A\sqrt{D}} \left[ C_j \ln|\mathbf{x} - \mathbf{x}_j| + \frac{C_j}{\nu} + B_j \right], \quad (4.12)$$

where  $G_{\lambda i,j} \equiv G_\lambda(\mathbf{x}_i; \mathbf{x}_j)$  and  $\nu = -1/\ln \varepsilon$ . This matching condition provides the  $k$  equations

$$C_j (1 + 2\pi\nu R_{\lambda,j,j}) + \nu B_j + 2\pi\nu \sum_{i \neq j}^k C_i G_{\lambda i,j} = 0, \quad j = 1, \dots, k. \quad (4.13)$$

We remark that the constants  $\tau$  and  $D$  appear in the operator of the  $\lambda$ -dependent Green's function defined by (4.11).

For  $D = \mathcal{O}(1)$  and  $\tau = \mathcal{O}(1)$ , we consider the leading-order theory in  $\nu$  based on assuming that  $\nu \equiv -1/\ln \varepsilon \ll 1$ . Then, to leading-order in  $\nu$ , (4.13) yields that  $C_j = 0$  for  $j = 1, \dots, k$ . This implies that  $N_j$  in (4.8) is bounded as  $\rho \rightarrow \infty$ , and so we can impose that  $N_j'(\rho) \rightarrow 0$  as  $\rho \rightarrow \infty$ . Therefore, when  $\tau = \mathcal{O}(1)$  and  $D = \mathcal{O}(1)$ , then, to leading order in  $\nu$ , the eigenvalue problems (4.8) for  $j = 1, \dots, k$  are coupled together only through the determination of the source strengths  $S_1, \dots, S_k$  from the nonlinear algebraic system (2.7). For this leading-order theory, we compute the real part of the principal eigenvalue  $\lambda_0$  of (4.8) as a function of  $S_j$ , subject to the condition that  $N_j'(\rho) \rightarrow 0$  as  $\rho \rightarrow \infty$ . This computation is done by discretizing (4.8) by finite differences and then calculating the spectrum of the resulting matrix eigenvalue problem using LAPACK (cf. [1]). The plot of  $\text{Re}(\lambda_0)$  versus  $S_j$  is shown in Fig. 9(a) for the range  $S_j < 7.5$ , which includes the value  $S_j = \Sigma_2 \approx 4.31$  corresponding to the spot self-replication threshold of §4.1. In Fig. 9(b) and Fig. 9(c), respectively, we plot the eigenfunctions  $\Phi_j(\rho)$  and  $N_j(\rho)$  for two different values of  $S_j$ . For this leading-order-in- $\nu$  local eigenvalue problem, our computations show that  $\text{Re}(\lambda_0) < 0$  for  $S_j < 7.5$ . Therefore, we conclude that an instability can only be generated through the *global* coupling of the local eigenvalue problems. This coupling occurs when we do not make the  $\nu \ll 1$  approximation in (4.13).

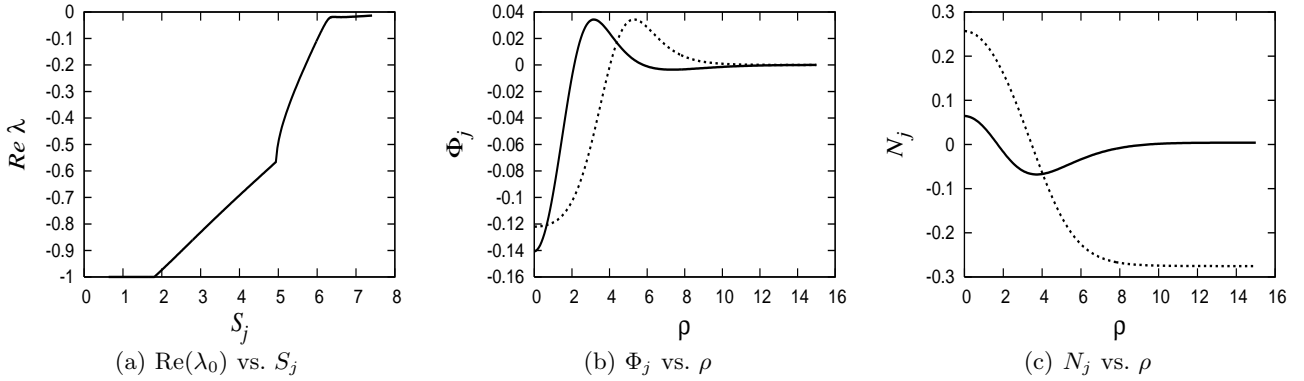


Figure 9. *Left figure: The real part of the largest eigenvalue  $\text{Re}(\lambda_0)$  of (4.8) vs.  $S_j$  subject to the condition that  $N_j$  is bounded as  $\rho \rightarrow \infty$ . Middle figure:  $\Phi_j$  vs.  $\rho$  for  $S_j = 3.0$  (solid curve) and  $S_j = 6.0$  (dashed curve). Right figure:  $N_j$  vs.  $\rho$  for  $S_j = 3.0$  (solid curve) and  $S_j = 6.0$  (dashed curve).*

Since  $\nu = -1/\ln \varepsilon$  decreases only very slowly as  $\varepsilon$  decreases, the leading-order approximation  $C_j = 0$  for  $j = 1, \dots, k$  to (4.13), which does not lead to any instabilities, is not expected to be very accurate. Consequently, we must examine the effect of the coupling in (4.13). Since (4.8) is a linear homogeneous problem, we introduce  $\hat{B}_j$  by  $B_j = \hat{B}_j C_j$ , and

we define the new variables  $\hat{\Phi}_j$  and  $\hat{N}_j$  by  $\Phi_j = C_j \hat{\Phi}_j$  and  $N_j = C_j \hat{N}_j$ . Then, (4.8) on  $0 < \rho < \infty$  becomes

$$\hat{\Phi}_j'' + \frac{1}{\rho} \hat{\Phi}_j' - \hat{\Phi}_j + 2U_j V_j \hat{\Phi}_j + V_j^2 \hat{N}_j = \lambda \hat{\Phi}_j, \quad \hat{N}_j'' + \frac{1}{\rho} \hat{N}_j' - V_j^2 \hat{N}_j - 2U_j V_j \hat{\Phi}_j = 0, \quad (4.14 a)$$

$$\hat{\Phi}_j'(0) = \hat{N}_j'(0) = 0; \quad \hat{\Phi}_j(\rho) \rightarrow 0, \quad \hat{N}_j(\rho) \rightarrow \ln \rho + \hat{B}_j, \quad \text{as } \rho \rightarrow \infty. \quad (4.14 b)$$

The constant  $\hat{B}_j$  in (4.14 b) is a function of the, as yet unknown, complex-valued eigenvalue parameter  $\lambda$ . It also depends on the source strength  $S_j$  through the solution  $U_j$  and  $V_j$  to the core problem (2.3).

In terms of  $\hat{B}_j$ , (4.13) transforms to the homogeneous linear system for  $C_1, \dots, C_k$  given by

$$C_j(1 + 2\pi\nu R_{\lambda j,j} + \nu \hat{B}_j) + 2\pi\nu \sum_{i \neq j}^k C_i G_{\lambda j,i} = 0, \quad j = 1, \dots, k. \quad (4.15)$$

It is convenient to express (4.15) in matrix form as

$$\mathcal{M} \mathbf{c} = \mathbf{0}, \quad \mathcal{M} \equiv I + \nu \mathcal{B} + 2\pi\nu \mathcal{G}_\lambda, \quad (4.16 a)$$

where  $I$  is the  $k \times k$  identity matrix and  $\mathbf{c} \equiv (C_1, \dots, C_k)^T$ . In (4.16 a),  $\mathcal{B}$  is a diagonal matrix and  $\mathcal{G}_\lambda$  is the  $\lambda$ -dependent symmetric Green's matrix defined by

$$\mathcal{G}_\lambda \equiv \begin{pmatrix} R_{\lambda 1,1} & G_{\lambda 1,2} & \cdots & G_{\lambda 1,k} \\ G_{\lambda 2,1} & R_{\lambda 2,2} & \cdots & G_{\lambda 2,k} \\ \vdots & \vdots & \vdots & \vdots \\ G_{\lambda k,1} & G_{\lambda k,2} & \cdots & G_{\lambda k,k} \end{pmatrix}, \quad \mathcal{B} \equiv \begin{pmatrix} \hat{B}_1 & 0 & \cdots & 0 \\ 0 & \hat{B}_2 & \cdots & 0 \\ \vdots & \vdots & \vdots & \vdots \\ 0 & 0 & \cdots & \hat{B}_k \end{pmatrix}. \quad (4.16 b)$$

Since  $\bar{G}_{\lambda ij} \neq G_{\lambda j,i}$  when  $\lambda$  is complex-valued, where the overbar denotes complex conjugate,  $\mathcal{G}_\lambda$  is not Hermitian.

The eigenvalue  $\lambda$  is determined from the condition that  $\det(\mathcal{M}) = 0$ , so that there is a nontrivial solution  $\mathbf{c} \neq \mathbf{0}$  to (4.16 a). This condition leads, effectively, to a transcendental equation for  $\lambda$ . The roots of this equation determine the discrete eigenvalues governing the linear stability of the  $k$ -spot quasi-equilibria to locally radially symmetric perturbations near each spot. We summarize our formulation of the global eigenvalue problem as follows:

**Principal Result 4.2:** *Consider a  $k$ -spot quasi-equilibrium solution to the GS model (1.1). For  $\varepsilon \rightarrow 0$ , with  $D = \mathcal{O}(1)$ ,  $A = \mathcal{O}(-\varepsilon \ln \varepsilon)$ , and  $\tau\lambda \ll \mathcal{O}(\varepsilon^{-2})$ , the stability of this pattern to locally radially symmetric perturbations near each spot is determined by the condition  $\det(\mathcal{M}) = 0$ , where  $\mathcal{M}$  is defined in (4.16). The diagonal matrix  $\mathcal{B}$  in (4.16) is determined in terms of  $S_j$  and  $\lambda$  by the local problems (4.14) for  $j = 1, \dots, k$ . If the principal eigenvalue  $\lambda_0$  of this global eigenvalue problem is such that  $\text{Re}(\lambda_0) < 0$ , then the  $k$ -spot quasi-equilibrium solution is linearly stable to locally radially symmetric perturbations near each spot, and it is linearly unstable if  $\text{Re}(\lambda_0) > 0$ .*

We remark that (4.16) couples the local spot solutions in two distinct ways. First, the  $\lambda$ -dependent terms  $R_{\lambda j,j}$  and  $G_{\lambda i,j}$  in the Green's matrix  $\mathcal{G}_\lambda$  in (4.16) depend on  $D$ , on  $\tau\lambda$ , and on the spatial configuration  $\mathbf{x}_1, \dots, \mathbf{x}_k$  of spots, as well as the geometry of  $\Omega$ . Secondly, the constant  $\hat{B}_j$  in the matrix  $\mathcal{B}$  depends on  $\lambda$  and on  $S_j$ . Recall that the source strengths  $S_1, \dots, S_k$  are coupled through the nonlinear algebraic system (2.7), which involves  $\mathcal{A}$ ,  $D$ , the reduced-wave Green's function, and the spatial configuration of spot locations.

From our numerical study of this global eigenvalue problem in §5–6, there are two mechanisms through which a  $k$ -spot quasi-equilibrium pattern can lose stability. Firstly, for  $k \geq 1$  there can be a complex conjugate pair of eigenvalues that crosses into the unstable half-plane  $\text{Re}(\lambda_0) > 0$ . This instability as a result of a Hopf bifurcation initiates an oscillatory profile instability, whereby the spot amplitudes undergo temporal oscillations. Such an instability typically occurs if  $\tau$  is sufficiently large. Alternatively, for  $k \geq 2$ , the principal eigenvalue  $\lambda_0$  can be real and enter the unstable

right half-plane  $\text{Re}(\lambda_0) > 0$  along the real axis  $\text{Im}(\lambda_0) = 0$ . This instability, due to the creation of a positive real eigenvalue, gives rise to an unstable sign-fluctuating perturbation of the spot amplitudes and it initiates a competition instability, leading to spot annihilation events. This instability can be triggered if  $D$  is sufficiently large or, equivalently, if the inter-spot separation is too small.

The global eigenvalue problem leading to the stability formulation in Principal Result 4.2 is a new result, and essentially can be viewed as an extended NLEP theory that accounts for all terms in powers of  $\nu$ . In Appendix B, we summarize the main results for the leading-order-in- $\nu$  NLEP stability theory of [62] based on the parameter range  $D = \mathcal{O}(\nu^{-1})$  and  $A = \mathcal{O}(\varepsilon[-\ln \varepsilon]^{1/2})$ , and we show how our global eigenvalue problem can be asymptotically reduced to the leading order NLEP problem of [62] in this parameter regime for  $D$  and  $A$ .

### 4.3 Symmetric Spot Patterns and a Circulant Matrix

The global eigenvalue problem is rather challenging to investigate in full generality owing to the complexity of the two different coupling mechanisms in (4.16). However, for the special case where the spot configuration  $\mathbf{x}_1, \dots, \mathbf{x}_k$  is such that  $\mathcal{G}$ , and consequently  $\mathcal{G}_\lambda$ , are circulant matrices, then the complexity of this eigenvalue problem reduces considerably. For this special arrangement of spot locations, the spots have a common source strength  $S_c = S_j$  for  $j = 1, \dots, k$ , where  $S_c$  satisfies the nonlinear algebraic equation (2.22). Hence, the inner problem (4.14) is the same for each spot, which enforces that  $\hat{B}_j \equiv \hat{B}_c$  for  $j = 1, \dots, k$ , where  $\hat{B}_c = \hat{B}_c(\lambda, S_c)$ . Therefore, we can write  $\mathcal{B} = \hat{B}_c I$  in (4.16). Moreover, let  $\mathbf{v}$  be an eigenvector of the  $\lambda$ -dependent Green's matrix  $\mathcal{G}_\lambda$  with eigenvalue  $\omega_\lambda = \omega_\lambda(\tau\lambda)$ , i.e.  $\mathcal{G}_\lambda \mathbf{v} = \omega_\lambda \mathbf{v}$ . We note that the matrix  $\mathcal{G}_\lambda$  is also circulant when  $\mathcal{G}$  is circulant. Then, the condition that  $\mathcal{M}$  in (4.16) is a singular matrix reduces to  $k$  transcendental equations in  $\lambda$ . We summarize the result as follows:

**Principal Result 4.3:** *Under the conditions of Principal Result 4.2, suppose that the spot configuration  $\mathbf{x}_1, \dots, \mathbf{x}_k$  is such that  $\mathcal{G}$ , and consequently  $\mathcal{G}_\lambda$ , are circulant matrices. Then, the eigenvalue condition  $\det(\mathcal{M}) = 0$  for (4.16) reduces to the  $k$  transcendental equations for  $\lambda$  given by*

$$f_j \equiv 1 + \nu \hat{B}_c + 2\pi\nu\omega_{\lambda_j}(\tau\lambda) = 0, \quad (4.17)$$

where  $\omega_{\lambda_j}(\tau\lambda)$  for  $j = 1, \dots, k$  is any eigenvalue of the matrix  $\mathcal{G}_\lambda$ . The  $k$ -distinct eigenvectors  $\mathbf{v}$  of  $\mathcal{G}_\lambda$  determine the choices for  $\mathbf{c} = (C_1, \dots, C_k)^T$ . By equating real and imaginary parts, (4.17) can be reduced to

$$\text{Re}(f_j) \equiv 1/\nu + \text{Re}(\hat{B}_c) + 2\pi\text{Re}(\omega_{\lambda_j}(\tau\lambda)) = 0, \quad \text{Im}(f_j) \equiv \text{Im}(\hat{B}_c) + 2\pi\text{Im}(\omega_{\lambda_j}(\tau\lambda)) = 0. \quad (4.18)$$

When  $\mathcal{G}_\lambda$  is a circulant and symmetric matrix, then its spectrum, as needed in Principal Result 4.3, can be determined analytically. To do so, let the row vector  $\mathbf{a} = (a_1, \dots, a_k)$  denote the first row of  $\mathcal{G}$ . Since  $\mathcal{G}_\lambda$  is circulant it follows that all of the other rows of  $\mathcal{G}$  can be obtained by cycling the components of the vector  $\mathbf{a}$ . In addition, since  $\mathcal{G}_\lambda$  is also necessarily a symmetric matrix it follows that  $a_2 = a_k$ ,  $a_3 = a_{k-1}$ ,  $\dots$ , and  $a_j = a_{k+2-j}$  for  $j = 2, \dots, \lceil k/2 \rceil$ , where the ceiling function  $\lceil x \rceil$  is the smallest integer not less than  $x$ . We recall that if a  $k \times k$  matrix is circulant, its eigenvectors  $\mathbf{v}_j$  and eigenvalues  $\omega_{\lambda_j}$ , which consist of the  $k^{\text{th}}$  roots of unity, are given by

$$\omega_{\lambda_j} = \sum_{m=0}^{k-1} a_{m+1} e^{2\pi(j-1)m/k}, \quad \mathbf{v}_j = (1, e^{2\pi(j-1)/k}, \dots, e^{2\pi(j-1)(k-1)/k})^T, \quad j = 1, \dots, k. \quad (4.19)$$

Here  $a_m$  is the  $m^{\text{th}}$  component of the row vector  $\mathbf{a}$ .

For illustration, let  $k = 3$ . Then, the eigenpairs are  $\mathbf{v}_1 = (1, 1, 1)^T$  with  $\omega_{\lambda_1} = a_1 + a_2 + a_3$ ,  $\mathbf{v}_2 = (1, e^{2\pi i/3}, e^{4\pi i/3})^T$  with  $\omega_{\lambda_2} = a_1 + a_2 e^{2\pi i/3} + a_3 e^{4\pi i/3}$ , and  $\mathbf{v}_3 = (1, e^{4\pi i/3}, e^{2\pi i/3})^T$  with  $\omega_{\lambda_3} = a_1 + a_2 e^{4\pi i/3} + a_3 e^{2\pi i/3}$ . Then, since the matrix is also symmetric, we have  $a_2 = a_3$ , so that  $\omega_{\lambda_2} = \omega_{\lambda_3} = a_1 - a_2$ , which yields one eigenvalue of multiplicity two. Then, since any linear combination of  $\mathbf{v}_2$  and  $\mathbf{v}_3$  is also an eigenvector, we take the real part of  $\mathbf{v}_2$  as one such vector, and the imaginary part of  $\mathbf{v}_2$  as the other. In summary, we can take  $\mathbf{v}_1 = (1, 1, 1)^T$ ,  $\mathbf{v}_2 = (1, -0.5, -0.5)^T$  and  $\mathbf{v}_3 = (0, \sqrt{3}/2, -\sqrt{3}/2)^T$  as the three eigenvectors of  $\mathcal{G}_\lambda$  for the three-spot pattern.

In general, the symmetry of  $\mathcal{G}_\lambda$  implies that  $a_j = a_{k+2-j}$  and  $\mathbf{v}_j = \mathbf{v}_{k+2-j}$ , and  $v_{jm} = v_{j(k+2-m)}$  for  $m = 2, \dots, \lceil k/2 \rceil$  and  $j = 2, \dots, \lceil k/2 \rceil$ . Here  $v_{jm}$  denotes the  $m^{\text{th}}$  component of the column vector  $\mathbf{v}_j$ . Since the eigenvalue is  $\omega_{\lambda_j} = \mathbf{v}_j \cdot \mathbf{a}$ , we have  $\omega_{\lambda_j} = \omega_{\lambda_{k+2-j}}$ . This generates  $\lceil k/2 \rceil - 1$  eigenvalues with multiplicity two, whose eigenvectors can be obtained by taking any linear combination of two complex conjugate eigenvectors. For instance, for the  $j^{\text{th}}$  eigenvalue  $\omega_{\lambda_j}$  the corresponding two eigenvectors can be taken as the real and imaginary parts of  $\mathbf{v}_j$ , respectively. In summary, we know that all of the eigenvectors can be chosen to be real, but that the eigenvalues in general will be complex when  $\lambda$  is complex. This leads to the following result for the spectrum of the  $k \times k$  symmetric and circulant Green's matrix  $\mathcal{G}_\lambda$  whose first row vector is  $\mathbf{a} = (a_1, \dots, a_m)$ :

$$\begin{cases} \omega_{\lambda_1} &= \sum_{m=1}^k a_m, \quad v_1^T = (1, \dots, 1), \\ \omega_{\lambda_j} &= \sum_{m=0}^{k-1} \cos\left(\frac{2\pi(j-1)m}{k}\right) a_{m+1}, \quad \text{eigenvalues with multiplicity 2,} \\ \mathbf{v}_j^T &= \left(1, \cos\left(\frac{2\pi(j-1)}{k}\right), \dots, \cos\left(\frac{2\pi(j-1)(k-1)}{k}\right)\right), \\ \mathbf{v}_{k+2-j}^T &= \left(0, \sin\left(\frac{2\pi(j-1)}{k}\right), \dots, \sin\left(\frac{2\pi(j-1)(k-1)}{k}\right)\right), \quad j = 2, \dots, \lceil k/2 \rceil + 1. \end{cases} \quad (4.20)$$

Note that if  $k$  is even, then  $\omega_{\lambda_{\lceil k/2 \rceil + 1}} = \sum_{m=1}^k (-1)^{m-1} a_m$  is a simple eigenvalue with eigenvector  $(1, -1, \dots, 1, -1)^T$ .

For a symmetric spot pattern, we can simply substitute (4.20) into (4.18) of Principal Result 4.3 to derive the transcendental equation associated with the  $j^{\text{th}}$  eigenvector  $\mathbf{v}_j$  of  $\mathcal{G}_\lambda$ . This yields,

$$\nu^{-1} + \text{Re}(\hat{B}_c) + 2\pi \sum_{m=1}^k \text{Re}(a_m) v_{jm} = 0, \quad \text{Im}(\hat{B}_c) + 2\pi \sum_{m=1}^k \text{Im}(a_m) v_{jm} = 0, \quad j = 1, \dots, \lceil k/2 \rceil + 1. \quad (4.21)$$

Here the row vector  $\mathbf{a}$  has components  $a_1 = R_{\lambda 1,1}$ , and  $a_m = G_{\lambda 1,m}$  for  $m = 2, \dots, k$ , where  $G_{\lambda 1,m}$  and  $R_{\lambda 1,1}$  are determined from the  $\lambda$ -dependent Green's function and its regular part satisfying (4.11). In (4.21),  $v_{jm}$  denotes the  $m^{\text{th}}$  component of the column vector  $\mathbf{v}_j$ . We remark that when  $\lambda$  is real, (4.21) can be reduced to only one equation.

At the onset of a competition instability, where an unstable eigenvalue first enters the unstable right-half plane  $\text{Re}(\lambda) > 0$  along the real axis  $\text{Im}(\lambda) = 0$ , the result (4.21) can be simplified further. Upon differentiating the problem for  $U_j$  and  $V_j$  in (2.3) with respect to  $S_j$ , and then comparing the resulting system with the eigenvalue problem in (4.14), it readily follows that

$$\hat{\Phi}_j = \frac{\partial}{\partial S_j} V_j, \quad \hat{N}_j = \frac{\partial}{\partial S_j} U_j, \quad \text{when } \lambda = 0. \quad (4.22)$$

Therefore, for the special case where  $S_j = S_c$  for  $j = 1, \dots, k$ , the constant  $\hat{B}_c$  in (4.21) when  $\lambda = 0$  can be calculated in terms of the derivative of  $\chi$  by

$$\hat{B}_c = \chi'(S_c), \quad \text{when } \lambda = 0. \quad (4.23)$$

A plot of  $\chi'(S_c)$  is shown below in Fig. 10(a). Thus, for a configuration of spots for which the Green's matrix is circulant symmetric, the threshold condition for a competition instability, corresponding to setting  $\lambda = 0$  in (4.21)



and recalling (2.22), is to solve the coupled system

$$\chi'(S_c) + 2\pi\omega_{\lambda_j} = -\nu^{-1}, \quad \mathcal{A} = S_c(1 + 2\pi\nu\theta) + \nu\chi(S_c); \quad \mathcal{A} = \varepsilon^{-1}\nu A\sqrt{D}, \quad \nu = \frac{-1}{\ln \varepsilon}. \quad (4.24)$$

Since  $\mathcal{G}$  and  $\mathcal{G}_\lambda$  coincide at  $\lambda = 0$ , then  $\theta$  in (4.24) is the eigenvalue of  $\mathcal{G}$  with eigenvector  $\mathbf{e} = (1, \dots, 1)^T$ , i.e.  $\mathcal{G}\mathbf{e} = \theta\mathbf{e}$ , and  $\omega_{\lambda_j}$  for  $j = 1, \dots, \lceil k/2 \rceil + 1$  is any of the other eigenvalues of  $\mathcal{G}$  as given in (4.20) when  $\lambda = 0$ . We remark that when  $k$  is even, our computational results in §5–6 below will show that the most unstable mode for a competition instability is the sign-fluctuating mode  $(1, -1, \dots, 1, -1)^T$ , which corresponds to setting  $j = \lceil k/2 \rceil + 1$  in (4.24) and using  $\omega_{\lambda(\lceil k/2 \rceil + 1)} = \sum_{m=1}^k (-1)^{m-1} a_m$ . Here  $a_1 = R_{1,1}$ , and  $a_m = G_{1,m}$  for  $m = 2, \dots, k$ , is the first row of  $\mathcal{G}$ .

Owing to the considerable reduction in complexity of the global eigenvalue problem when  $\mathcal{G}$  and  $\mathcal{G}_\lambda$  are circulant matrices, in §5–6 we will only compute competition and oscillatory stability thresholds of quasi-equilibrium spot patterns that lead to this special matrix structure. The numerical approach used to compute these thresholds associated with the stability formulation of Principal Result 4.3 is outlined in Appendix C.

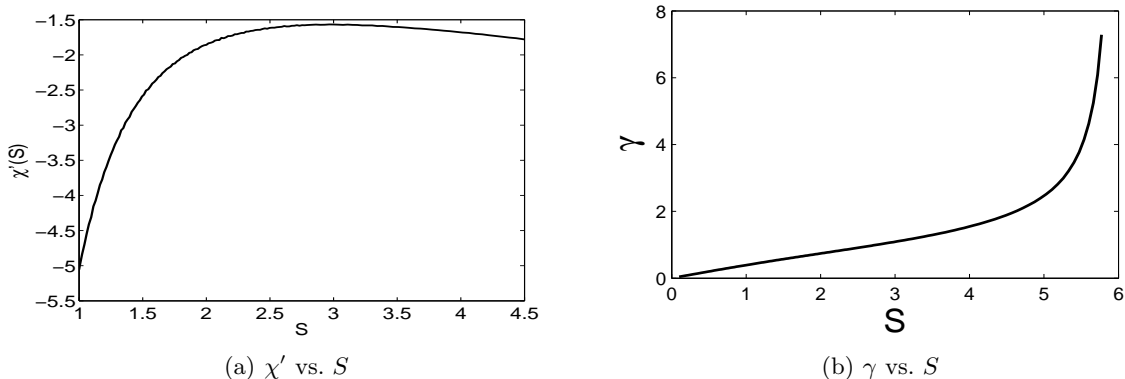


Figure 10. *Left figure: Plot of numerically computed  $\chi'(S)$ , as defined in (2.3). Right figure: Plot of the numerically computed  $\gamma(S)$  as defined in (3.7) of Principal Result 3.1.*

Finally, we remark that the numerical implementation of our asymptotic theory in §3 and §4 for spot dynamics and stability relies on the computation of the three functions  $\chi(S)$ ,  $\chi'(S)$ , and  $\gamma(S)$ , defined in terms of the core problem by (2.3) and (3.7). The result for  $\chi(S)$  was given previously in Fig. 1(b), while  $\chi'(S)$  and  $\gamma(S)$  are plotted in Fig. 10(a) and Fig. 10(b), respectively.

## 5 One- and Two-Spot Patterns on the Infinite Plane and in Large Domains

In this section we apply the asymptotic theory of §2–4 to the special case of either a one- or a two-spot pattern on the infinite plane  $\mathbb{R}^2$ . For this problem we can set  $D = 1$  in (1.1) without loss of generality. When  $\Omega = \mathbb{R}^2$ , the reduced-wave Green's function and its regular part satisfying (1.2) with  $D = 1$  is simply

$$G(\mathbf{x}; \mathbf{x}_j) = \frac{1}{2\pi} K_0(|\mathbf{x} - \mathbf{x}_j|), \quad R_{jj} = \frac{1}{2\pi}(\ln 2 - \gamma_e). \quad (5.1)$$

Here  $\gamma_e$  is Euler's constant, and  $K_0(r)$  is the modified Bessel function of the second kind of order zero.

A  $k$ -spot quasi-equilibrium solution with spots at  $\mathbf{x}_j \in \mathbb{R}^2$  for  $j = 1, \dots, k$  is given in (2.8) of Principal Result 2.1.

From (2.7) and (5.1), the source strengths  $S_1, \dots, S_k$  satisfy the nonlinear algebraic system

$$\mathcal{A} = S_j \left(1 + \nu(\ln 2 - \gamma_e)\right) + \nu \sum_{i \neq j}^k S_i K_0 |\mathbf{x}_i - \mathbf{x}_j| + \nu \chi(S_j), \quad j = 1, \dots, k; \quad \mathcal{A} = \varepsilon^{-1} \nu A, \quad \nu = -\frac{1}{\ln \varepsilon}. \quad (5.2)$$

To determine the stability of the  $k$ -spot quasi-equilibrium solution to locally radially symmetric perturbations, we must find the eigenvalues of the global eigenvalue problem of §4.2 consisting of (4.14) coupled to (4.15). The  $\lambda$ -dependent Green's function and its regular part, satisfying (4.11) with  $D = 1$  in  $\mathbb{R}^2$ , are

$$G_\lambda(\mathbf{x}; \mathbf{x}_j) = \frac{1}{2\pi} K_0 \left( \sqrt{1 + \tau\lambda} |\mathbf{x} - \mathbf{x}_j| \right), \quad R_{\lambda jj} = \frac{1}{2\pi} \left( \ln 2 - \gamma_e - \log \sqrt{1 + \tau\lambda} \right). \quad (5.3)$$

Since  $\lambda$  can be complex, we must take  $\log z$  to be the principal branch of the logarithm function, and choose for  $z = \sqrt{1 + \tau\lambda}$  the principal branch of the square root, in order that  $K_0(z)$  decays when  $z \rightarrow \infty$  along the positive real axis. In terms of this Green's function, the homogeneous linear system (4.15) becomes

$$C_j \left(1 + \nu(\ln 2 - \gamma_e - \log \sqrt{1 + \tau\lambda} + \hat{B}_j)\right) + \nu \sum_{i \neq j}^k C_i K_0 \left( \sqrt{1 + \tau\lambda} |\mathbf{x}_i - \mathbf{x}_j| \right) = 0, \quad j = 1, \dots, k. \quad (5.4)$$

Below, we consider the specific cases of one- and two-spot solutions in  $\mathbb{R}^2$ . The numerical procedure used below to compute the competition and oscillatory instability thresholds is summarized in Appendix C.

### 5.1 A One-Spot Solution in $\mathbb{R}^2$

For a one-spot solution with spot at the origin, (5.2) reduces to the scalar nonlinear algebraic equation

$$\mathcal{A} = S_1 + \nu S_1 (\ln 2 - \gamma_e) + \nu \chi(S_1), \quad \mathcal{A} = \varepsilon^{-1} \nu A, \quad \nu = -\frac{1}{\ln \varepsilon}. \quad (5.5)$$

In order that  $C_1 \neq 0$  in (5.4), we require that  $\lambda$  satisfy the nonlinear transcendental equation

$$\hat{B}_1 + \frac{1}{\nu} + \left( \ln 2 - \gamma_e - \log \sqrt{1 + \tau\lambda} \right) = 0. \quad (5.6)$$

Here  $\hat{B}_1 = \hat{B}_1(\lambda, S_1)$  is to be computed from (4.14) in terms of the solution  $U_1$  and  $V_1$  to the core problem (2.3). Our computational results lead to a phase diagram in the  $A$  versus  $\tau$  parameter-plane characterizing the stability of a one-spot solution. In the numerical results below we have fixed  $\varepsilon = 0.02$ .

From (5.5) we compute that there is no quasi-equilibrium one-spot solution when  $A \geq A_f = 0.1766$ . This existence threshold for  $A$ , which was obtained by varying  $S_1$  in (5.5) on  $S_1 \in [0.22, 7.41]$ , is shown by the lower thin solid line in Fig. 11(a). From §4.1, the spot self-replication threshold  $A_s \approx 0.311$  for  $A$  is obtained by setting  $S_1 = \Sigma_2 \approx 4.31$  and  $\chi(\Sigma_2) \approx -1.783$  in (5.5). It is shown by the upper horizontal dotted line in Fig. 11(a). Moreover, in Fig. 11(a) the solid curve is the Hopf bifurcation threshold  $A$  versus  $\tau_H$  as computed from (5.6). At this Hopf bifurcation value, a complex conjugate pair of eigenvalues first enters the right half-plane. The resulting parameter-plane as shown in Fig. 11(a) is divided into four regions with the following solution behavior. In Regime  $\sigma$  with  $A < A_f$ , the quasi-equilibrium solution does not exist; in Regime  $\beta$ , enclosed by the thin solid horizontal line  $A_f = 0.1766$  and the heavy solid Hopf bifurcation curve, the quasi-equilibrium solution is unstable to an oscillatory profile instability; in Regime  $\zeta$  it is stable; and in Regime  $\theta$ , it is unstable to spot self-replication. In Fig. 11(b), we fix  $A = 0.18$  and we show that the real part  $\text{Re}(\lambda)$  increases with  $\tau$  on the range  $\tau \in [30, 40]$ . Note that for  $A = 0.18$ , the Hopf bifurcation threshold  $\tau_H = 36.06$  is where the complex conjugate pair of eigenvalues intersect the imaginary axis.

For three values of  $\varepsilon$ , in Fig. 12 we compare the stability threshold obtained from (5.6) with that obtained from

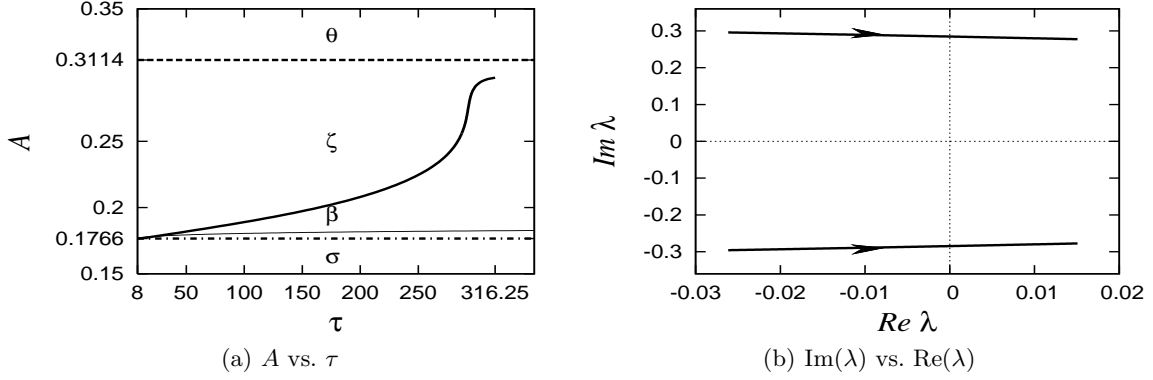


Figure 11. *One-spot solution in  $\mathbb{R}^2$  with  $\varepsilon = 0.02$ . (a) Phase-diagram in the parameter-plane  $A$  vs.  $\tau$ . The solid curve shows the Hopf bifurcation threshold  $\tau_H$ , the lower horizontal thin solid line plots our existence threshold  $A_f \approx 0.1766$ , the dot-dashed horizontal line is the existence threshold  $A_{fw} \approx 0.1758$  from NLEP theory, and the upper heavy dotted horizontal line indicates the spot-splitting threshold  $A_s = 0.311$ . Regime  $\sigma$ : No quasi-equilibrium solution exists; Regime  $\beta$ : Oscillations in the spot amplitude; Regime  $\zeta$ : Stable one-spot solution; Regime  $\theta$ : spot self-replication regime. (b) Fix  $A = 0.18$ , the spectrum in the complex  $\lambda$  plane is shown for  $\tau \in [30, 40]$ . At  $\tau = 30$ ,  $\lambda = -0.026 \pm 0.296 i$ . At  $\tau = 36.05$ ,  $\lambda = -0.000049 \pm 0.285 i$ . At  $\tau = 40$ ,  $\lambda = 0.015 \pm 0.278 i$ . As  $\tau$  increases a complex conjugate pair of eigenvalues enters the right half-plane.*

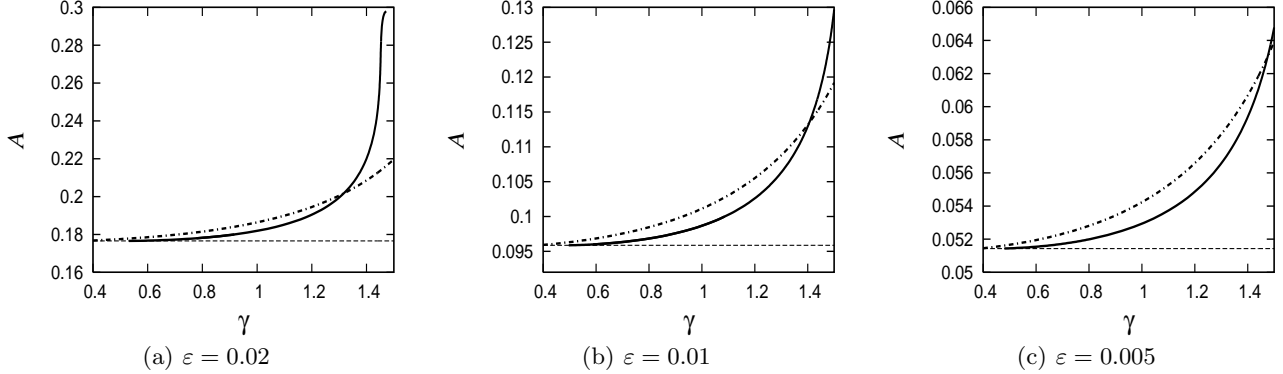


Figure 12. *One-spot solution in  $\mathbb{R}^2$ . In the  $A$  vs.  $\gamma \equiv -\ln \tau / \ln \varepsilon$  plane, we plot our existence threshold  $A_f$  by the thin dashed horizontal line, our Hopf bifurcation threshold  $A$  by the heavy solid curve, and the stability threshold  $A_{sw}$  from the NLEP theory by the dot-dashed curve (a)  $\varepsilon = 0.02$ ,  $A_f = 0.17659$ ;  $A_{fw} = 0.17575$ ; (b)  $\varepsilon = 0.01$ ,  $A_f = 0.095875$ ,  $A_{fw} = 0.095342$ ; (c)  $\varepsilon = 0.005$ ,  $A_f = 0.051432$ ,  $A_{fw} = 0.051133$ . Here  $A_{fw}$  is the existence threshold from NLEP theory given in (5.7).*

the NLEP analysis of [60], as summarized in Appendix B. From (B.3) and (B.5) of Appendix B, there are two threshold values  $A_{fw}$  and  $A_{sw}$  predicted from the leading-order-in- $\nu$  NLEP theory of [60]. For  $A < A_{fw}$  a one-spot quasi-equilibrium solution does not exist. For  $A < A_{sw}$  this solution is unstable to an oscillatory instability. These threshold values, with  $A_{sw}$  depending on  $\tau$  and the ground-state solution  $w$  of (B.1), are

$$A_{fw} \equiv 2\varepsilon \sqrt{\frac{b_0}{\nu}}, \quad b_0 \equiv \int_0^\infty w^2 \rho \, d\rho \approx 4.9347; \quad A_{sw} \equiv A_{fw} \left[ 1 - \left( \frac{\gamma}{4-\gamma} \right)^2 \right]^{-1/2}, \quad \gamma \equiv -\frac{\ln \tau}{\ln \varepsilon}. \quad (5.7)$$

For  $\varepsilon = 0.02$ , we get  $A_{fw} \approx 0.1757$ , which agrees very well with our existence threshold  $A_f \approx 0.1766$ . In Fig. 12 we compare the NLEP stability threshold  $A_{sw}$  versus  $\gamma = -\ln \tau / \ln \varepsilon$  with our Hopf bifurcation threshold  $A$  versus  $\gamma =$

$-\ln \tau_H / \ln \varepsilon$ . We recall from Appendix B that the NLEP theory predicts instability when  $A < A_{sw}$  for  $0 \leq \tau \leq \varepsilon^{-2}$ , but has no conclusion regarding stability or instability if  $A > A_{sw}$ . Our Hopf bifurcation threshold predicts that stability changes when we cross the heavy solid curves in Fig. 12.

Next, we study the possibility of real-valued unstable eigenvalues that have crossed along the real-axis  $\text{Im}(\lambda) = 0$  into the unstable half-plane  $\text{Re}(\lambda) > 0$ . The threshold condition for this is to set  $\lambda = 0$  and  $\hat{B}_1 = \chi'(S_1)$  in (5.6) to obtain that  $S_1$  satisfies  $\chi_1'(S_1) + \nu^{-1} + \ln 2 = \gamma_e$ . By differentiating (5.5) for  $\mathcal{A}$  with respect to  $S_1$ , we obtain that this threshold coincides with the minimum value  $S_{1m}$  of  $S_1$  for the curve  $\mathcal{A}$  versus  $S_1$  as defined by (5.5). For  $S > S_{1m}$ , we compute numerically that  $\text{Re}(\lambda) < 0$ , while  $\text{Re}(\lambda) > 0$  for  $S < S_{1m}$ . The critical value  $S_{1m}$ , for which  $\lambda = 0$ , corresponds to the fold point in the bifurcation diagram of  $u(0)$  versus  $\mathcal{A}$  (such as shown in Fig. 5(b)).

## 5.2 A Two-Spot Solution in $\mathbb{R}^2$

Next, we consider the case of two spots centered at  $\mathbf{x}_1 = (\alpha, 0)$  and  $\mathbf{x}_2 = (-\alpha, 0)$ , where  $\alpha > 0$  and  $\alpha \gg \mathcal{O}(\varepsilon)$ . We look for a symmetric solution where  $S_1 = S_2 = S_c$ . Then, from (5.2),  $S_c$  satisfies the nonlinear algebraic equation

$$\mathcal{A} = S_c [1 + \nu(\ln 2 - \gamma_e) + \nu K_0(2\alpha)] + \nu \chi(S_c), \quad \mathcal{A} = \varepsilon^{-1} \nu A, \quad \nu = -1/\ln \varepsilon. \quad (5.8)$$

For  $\varepsilon = 0.02$ , we first discuss the existence of the quasi-equilibrium two-spot solution. In Fig. 13(a) we plot  $\mathcal{A}$  versus  $S_c$  for three different values of  $\alpha$ , showing the existence of a fold point  $\mathcal{A}_f$  in the graph of  $S_c$  versus  $\mathcal{A}$ . This fold point  $\mathcal{A}_f(\alpha)$  is shown in Fig. 13(b) by the dotted curve. The solid curve in Fig. 13(b) is the corresponding two-term asymptotic result for  $\mathcal{A}_f$  obtained by expanding (5.8) in powers of  $\nu$  as in (2.23). This result shows that a quasi-equilibrium two-spot pattern exists for a spot separation distance of  $2\alpha$  only when  $\mathcal{A} > \mathcal{A}_f(\alpha)$ .

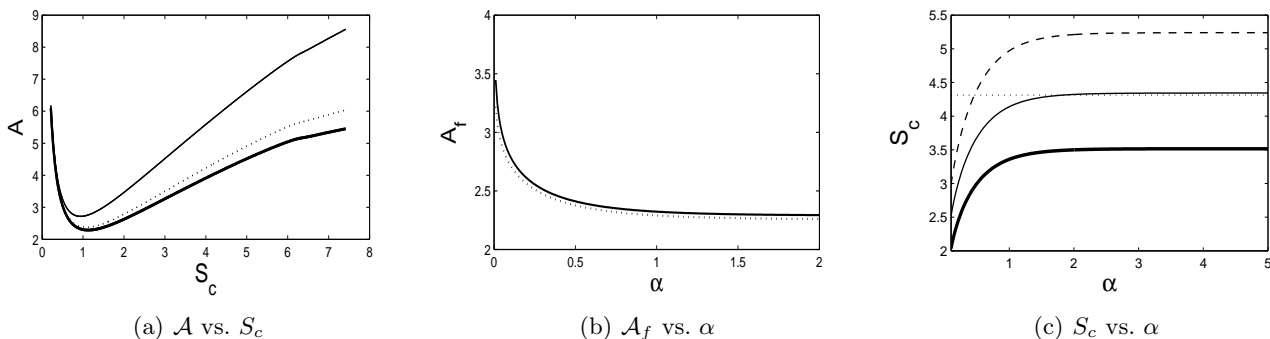


Figure 13. *Two spots at  $(\pm\alpha, 0)$  in  $\mathbb{R}^2$  with  $\varepsilon = 0.02$ . (a)  $\mathcal{A}$  vs.  $S_c$  for  $\alpha = 0.1$  (solid curve),  $\alpha = 0.5$  (dashed curve) and  $\alpha = 1.0$  (heavy solid curve). (b) The fold point  $\mathcal{A}_f$  vs.  $\alpha$ ; two-term asymptotic result (solid curve), and numerical result from (5.8) (dotted curve). (c)  $S_c$  vs.  $\alpha$  for  $\mathcal{A} = 3.5$  (heavy solid curve),  $\mathcal{A} = 4.0$  (solid curve) and  $\mathcal{A} = 4.5$  (dashed curve).*

Next, we discuss the possibility of self-replicating instabilities for an inter-spot separation of  $2\alpha$ . In Fig. 13(c), we plot  $S_c$  versus  $\alpha$  for  $\mathcal{A} = 3.5$  (solid curve),  $\mathcal{A} = 4.0$  (dashed curve) and  $\mathcal{A} = 4.5$  (heavy solid curve). Notice that for a fixed  $\mathcal{A} > \mathcal{A}_f$ , there are two solutions for  $S_c$  for a given  $\alpha$ . Since the solution branch with the smaller value for  $S_c$  is unstable, we only plot the large solution branch for  $S_c$  in this figure. Fig. 13(c) shows that for a fixed  $\alpha$ ,  $S_c$  is an increasing function of  $\mathcal{A}$ , whereas for a fixed  $\mathcal{A}$ , then  $S_c$  increases as  $\alpha$  increases. For the solid curve in Fig. 13(c) with  $\mathcal{A} = 3.5$ ,  $S_c < \Sigma_2$  for all  $\alpha$ , so that the spots never split for any inter-separation distance. Alternatively, the dashed curve for  $\mathcal{A} = 4.0$  and the heavy solid curve for  $\mathcal{A} = 4.5$  in Fig. 13(c) intersect the spot-splitting threshold

$S_c = \Sigma_2$  at  $\alpha \approx 1.81$  and  $\alpha \approx 0.46$ , respectively. This threshold initiates a spot-replication event. The self-replication threshold  $\mathcal{A}_s$  versus  $\alpha$  is obtained by setting  $S_c = 4.31$  in (5.8). Moreover, from (5.8), we readily observe that  $\mathcal{A}_s$  is a decreasing function of  $\alpha$  and asymptotes to its minimum value  $\mathcal{A}_{sm} = 3.98$  as  $\alpha \rightarrow \infty$ . This minimum value is obtained by setting  $S_c = \Sigma_2$  and  $K_0(2\alpha) \rightarrow 0$  in (5.8). We conclude that for any  $\mathcal{A} > \mathcal{A}_{sm}$ , a two-spot pattern on  $\mathbb{R}^2$  will be linearly unstable to a peanut-splitting instability if the inter-spot separation distance  $2\alpha$  is sufficiently large. Thus, for  $\mathcal{A} > \mathcal{A}_{sm}$ , a spot self-replication instability is, essentially, *under-crowding instability*, that is triggered only when the two spots are too isolated from each other. In terms of the original feed-rate parameter  $A$ , the spot-splitting threshold  $A_s \equiv \varepsilon \mathcal{A}_s / \nu$  is given by the heavy solid curve in the phase diagram of Fig. 14(a).

Next, we compute the stability thresholds for either competition and oscillatory instabilities. The  $\lambda$ -dependent Green's function is given in (5.3). Since the  $\lambda$ -dependent Green's matrix  $\mathcal{G}_\lambda$  is circulant, then Principal Result 4.3 applies. The eigenvectors  $\mathbf{v}_j$  and eigenvalues  $\omega_{\lambda j}$  of  $\mathcal{G}_\lambda$  for  $i = j, 2$  are

$$\begin{aligned} \omega_{\lambda 1} = \omega_{\lambda 1}(\tau\lambda) &= G_{\lambda 12} + R_{\lambda 11} = \frac{1}{2\pi} \left[ (\ln 2 - \gamma_e - \log \sqrt{1 + \tau\lambda}) + K_0(2\alpha\sqrt{1 + \tau\lambda}) \right], & \mathbf{v}_1 &\equiv (1, 1)^T, \\ \omega_{\lambda 2} = \omega_{\lambda 2}(\tau\lambda) &= R_{\lambda 11} - G_{\lambda 12} = \frac{1}{2\pi} \left[ (\ln 2 - \gamma_e - \log \sqrt{1 + \tau\lambda}) - K_0(2\alpha\sqrt{1 + \tau\lambda}) \right], & \mathbf{v}_2 &\equiv (1, -1)^T. \end{aligned}$$

Then, from (4.17) of Principal Result 4.3, we must determine the roots  $\lambda$  of the two transcendental equations

$$\nu^{-1} + \hat{B}_c + 2\pi\omega_{\lambda j}(\tau\lambda) = 0, \quad j = 1, 2, \quad (5.9)$$

where  $\hat{B}_c(\lambda, S_c)$  is to the common value for  $\hat{B}_j$  for  $j = 1, 2$  in (4.14).

Our numerical results below show that in some region of the  $A$  versus  $\alpha$  parameter-plane, the two-spot solution becomes unstable when  $\tau$  is increased due to the creation of an unstable eigenvalue  $\lambda$  from  $\omega_{\lambda 1}$  as a result of a Hopf bifurcation. Since this oscillatory instability is associated with the eigenvector  $\mathbf{v}_1 = (1, 1)^t = (C_1, C_2)^T$ , it leads to the initiation of a simultaneous in-phase oscillation in the amplitudes of the two spots. In another region of the  $A$  versus  $\alpha$  parameter plane we will show numerically that an unstable real positive eigenvalue  $\lambda$  for  $\omega_{\lambda 2}$  can occur, even when  $\tau = 0$ , if the inter-spot distance  $2\alpha$  is below some threshold. Since this instability is associated with the eigenvector  $\mathbf{v}_2 = (1, -1)^t = (C_1, C_2)^T$ , it leads to the initiation of a sign-fluctuating instability in the amplitudes of the two spots, which leads ultimately to the annihilation of one of the two spots. Since this instability is triggered when  $2\alpha$  is sufficiently small, it is also referred to as a competition or an overcrowding instability. The threshold for a competition instability associated with the dominant sign-fluctuating mode  $\mathbf{v}_2 = (1, -1)^T$  is obtained from the formulation (4.24). The threshold condition for this instability is reduced to finding the curve  $A = A(\alpha)$ , by eliminating the source strength  $S_c$  from the following nonlinear algebraic system:

$$\chi'(S_c) + \ln 2 - \gamma_e - K_0(2\alpha) = -\nu^{-1}, \quad A = \frac{\varepsilon}{\nu} (S_c [1 + \nu (\ln 2 - \gamma_e + K_0(2\alpha))] + \nu \chi(S_c)). \quad (5.10)$$

We fix  $\varepsilon = 0.02$  in the computations below. In Fig. 14(a) the two-spot existence threshold  $A_f$  as a function of  $\alpha \in [0.02, 2.02]$  is shown by the lower solid curve, while the spot self-replication threshold  $A_s$  versus  $\alpha$  discussed above is shown by the top heavy solid curve. To obtain  $A_f$  we determined the minimum value of  $A$  as  $S_c$  is varied in (5.8). In Fig. 14(a) the middle dotted curve is the threshold for the onset of a competition instability, obtained from (5.10). These three curves separate the  $A$  versus  $\alpha$  parameter-plane of Fig. 14(a) into four distinct regions. In Regime  $\sigma$ , the quasi-equilibrium two-spot solution does not exist. In Regime  $\beta$ , the two-spot quasi-equilibrium solution undergoes a competition instability for any  $\tau \geq 0$ . This instability ultimately leads to the annihilation of one of the spots. We note that the competition threshold approaches the existence threshold when  $\alpha$  becomes large.

This is because when  $\alpha \gg 1$  the spots are uncoupled, and there is no competition instability for a one-spot solution in  $\mathbb{R}^2$ . In Regime  $\zeta$ , the two-spot pattern is stable to a competition instability, but becomes unstable to an oscillatory profile instability when  $\tau$  is large enough. As  $\tau$  increases above a certain threshold  $\tau_H$ , a Hopf bifurcation occurs and the two-spot solution is unstable to the dominant in-phase, or synchronous, spot amplitude oscillation. In Regime  $\theta$  the two-spot quasi-equilibrium solution is unstable to spot self-replication for any  $\tau \geq 0$ .

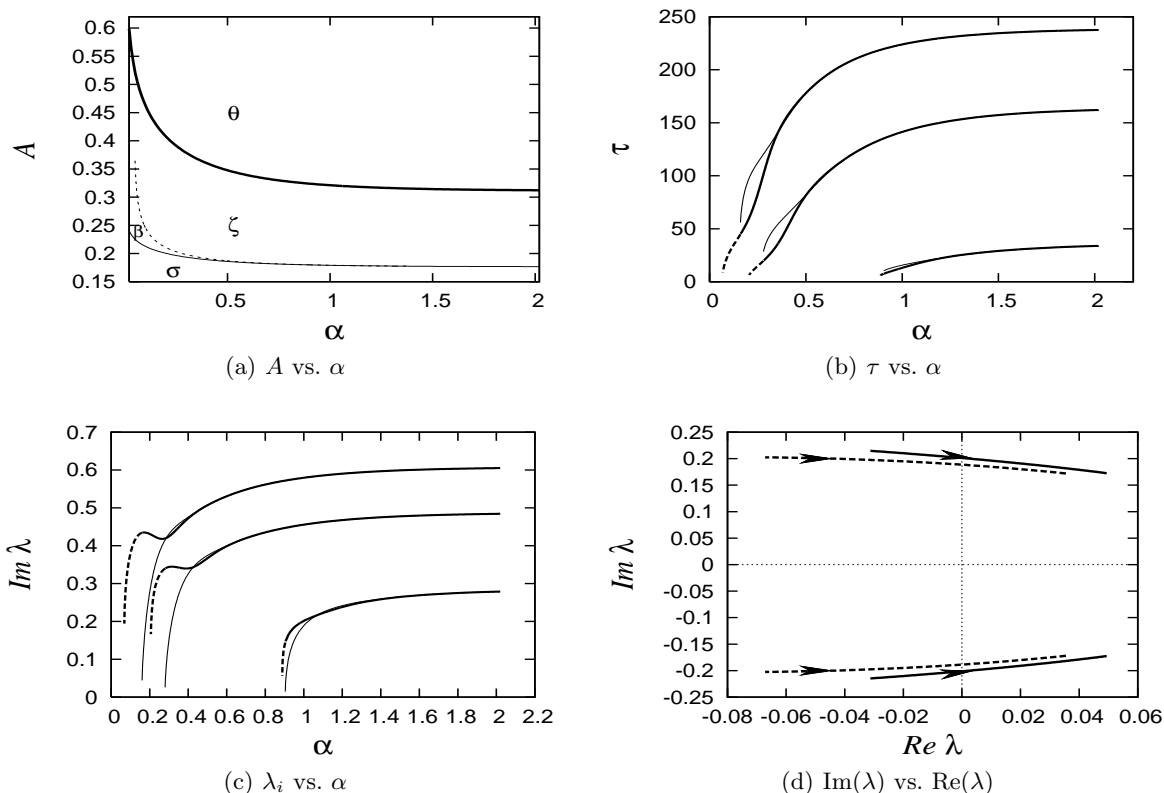


Figure 14. *Two-spot solution in  $\mathbb{R}^2$ . (a) We plot the existence threshold  $A_f$  vs.  $\alpha$  (lower curve), the spot-splitting threshold  $A_s$  vs.  $\alpha$  (top curve), and the competition instability threshold (dotted curve). (b) Hopf bifurcation threshold  $\tau_{H1}$  for in-phase oscillations (bottom of each pair of curves) and  $\tau_{H2}$  for out-of-phase oscillations (top of each pair of curves), are plotted versus  $\alpha$  for  $A = 0.18$  (bottom pair),  $A = 0.2$  (middle pair), and  $A = 0.22$  (top pair). The dotted portions on  $\tau_{H1}$  correspond to the parameter regime  $\beta$  in subfigure a) where competition instabilities occur for any  $\tau$ . (c) Imaginary part  $\lambda_i$  of  $\lambda$  vs.  $\alpha$  at the Hopf bifurcation thresholds for  $A = 0.18$  (bottom),  $A = 0.2$  (middle), and  $A = 0.22$  (top). The heavy solid curves are the eigenvalues for in-phase oscillations, and the thin solid curves are the eigenvalues for out-of-phase oscillations. The dotted portions lie on  $\tau_{H1}$  where a competition instability occurs. (d) Eigenvalue path in the complex plane for  $A = 0.18$  and  $\alpha = 1$  on the range  $\tau \in [10, 20]$ , with the arrow indicating the direction as  $\tau$  increases. The eigenvalues associated with in-phase (solid curves) and out-of-phase (dashed curves) oscillations enter the right half plane at  $\tau_{H1}$  and  $\tau_{H2}$ , respectively.*

For three values of  $A$ , in Fig. 14(b) we plot the Hopf bifurcation thresholds  $\tau_{H1}$  and  $\tau_{H2}$  associated with the eigenvectors  $\mathbf{v}_1 = (1, 1)^T$  and  $\mathbf{v}_2 = (1, -1)^T$ , respectively. From this figure we observe that in the limit  $\alpha \rightarrow \infty$ , corresponding to two isolated spots, the thresholds  $\tau_{H1}$  and  $\tau_{H2}$  approximate the Hopf bifurcation threshold  $\tau_H$  of an isolated one-spot solution.

From Fig. 14(b), the Hopf bifurcation curves for  $\tau_{H1}$ , which each have a dotted portion, end at the values  $\alpha_f =$

0.888, 0.206, 0.068 for the curves  $A = 0.18, 0.2, 0.22$ , respectively. These critical values of  $\alpha$  correspond to the existence threshold  $A = A_f(\alpha)$  for the quasi-equilibrium solution. Moreover, the Hopf bifurcation threshold  $\tau_{H2}$  terminates at another set of critical values  $\alpha_c = 0.904, 0.28, 0.16$  for the curves  $A = 0.18, 0.2, 0.22$ , respectively. The reason for this disappearance is seen in Fig. 14(c), where we plot the imaginary part of the eigenvalues at the Hopf bifurcation thresholds for  $\mathbf{v}_1 = (1, 1)^T$  (curves with dotted portions) and  $\mathbf{v}_2 = (1, -1)^T$  (curves without dotted portions). From this figure it is clear that as  $\alpha \rightarrow \alpha_c$  from above, the complex conjugate pair of eigenvalues associated with  $\tau_{H2}$  merge onto the real axis at the origin, which is precisely the crossing point for the onset of a competition instability.

When the spots are too close in the sense that  $\alpha_f < \alpha < \alpha_c$ , then there is a positive real (unstable) eigenvalue for any  $\tau \geq 0$ , which initiates a competition instability. If in addition,  $\tau < \tau_{H1}$ , it is the only unstable eigenvalue. In Fig. 14(b) and Fig. 14(c), the dotted segments of the curves correspond to the range of  $\alpha$  where this competition instability occurs. Finally, we observe from Fig. 14(b) that  $\tau_{H1} < \tau_{H2}$ . Therefore, for each  $\alpha > \alpha_c$ , the in-phase synchronous oscillatory instability of the spot amplitudes is always the dominant instability as  $\tau$  is increased.

For  $A = 0.18$ ,  $\alpha = 1.0$ , and  $10 \leq \tau \leq 20$ , in Fig. 14(d) we plot the path of the eigenvalues in the complex plane, corresponding to both  $\mathbf{v}_1$  (solid curves) and  $\mathbf{v}_2$  (dotted curves), as  $\tau$  is increased. For each case,  $\text{Re}(\lambda)$  increases as  $\tau$  increases. The two Hopf bifurcation values are, respectively,  $\tau_{H1} = 13.1$  and  $\tau_{H2} = 15.6$ .

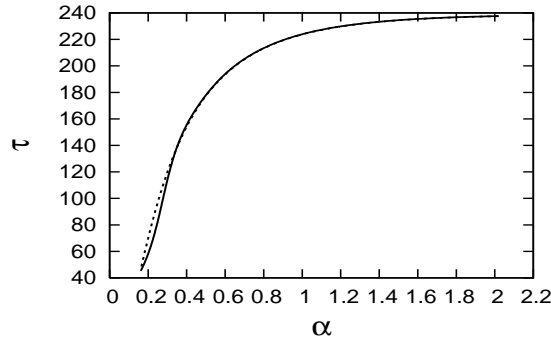


Figure 15. *Two-spot solution in  $\mathbb{R}^2$ . Fix  $A = 0.22$  and  $\varepsilon = 0.02$ . The Hopf bifurcation threshold  $\tau_{H1}$  vs.  $\alpha$  for a synchronous oscillatory instability obtained from the full stability problem (5.9) (solid curve) is compared with that obtained from the approximate system (5.11) resulting from the large- $\tau$  approximation (dotted curve).*

Next, we derive an approximation for the Hopf bifurcation threshold valid for  $\tau \gg 1$ . For  $\tau \gg 1$  and  $\alpha$  not too small, we exploit the exponential decay of the modified Bessel-function for large argument to obtain that the  $\lambda$ -dependent Green's matrix  $\mathcal{G}_\lambda$  is essentially a diagonal matrix. Therefore, in this large- $\tau$  limit we can substitute  $\omega_{\lambda_j} \approx R_{\lambda_{11}}$  for  $j = 1, 2$  into (5.9). In this way, and by using (5.3) for  $R_{\lambda_{11}}$ , we obtain that the limiting Hopf bifurcation threshold  $\tau_H$  and the critical eigenvalue  $\lambda = i\lambda_i$  are the solutions to the approximate system

$$\text{Im}(\hat{B}_c) = \frac{\pi}{4}, \quad \text{Re}(\hat{B}_c) + \ln 2 - \gamma_e - \frac{1}{2} \ln(\tau \lambda_i) = -\nu^{-1}. \quad (5.11)$$

For  $\varepsilon = 0.02$  and  $A = 0.22$ , in Fig. 15 we compare the threshold obtained from (5.11) with that obtained from the full transcendental equation (5.9) (as shown initially in Fig. 14(b)). This comparison, on the range  $\alpha \geq 0.16$  for which no competition instabilities occur, shows that (5.11) gives a good approximation provided that  $\alpha$  is not too small.

Finally, we derive the ODE system that determines the slow dynamics of the two-spot pattern when  $S_c < \Sigma_2$ . Provided that no other profile instabilities are present, and that  $\mathcal{A} > \mathcal{A}_f(\alpha)$ , we can explicitly evaluate the terms in

(3.7) of Principal Result 3.1 to obtain the DAE ODE system

$$\frac{d\alpha}{d\xi} = -\gamma(S_c)S_c K'_0(2\alpha), \quad \gamma(S_c) \equiv \frac{-2}{\int_0^\infty \phi^* V'_0 \rho d\rho}, \quad \xi = \varepsilon^2 t, \quad (5.12)$$

with  $S_c$  determined in terms of  $\alpha$  by (5.8). Since  $K'_0(r) < 0$  for any  $r > 0$  and  $|K'_0(r)|$  is a decreasing function of  $r$ , (5.12) shows that the two spots are repelling and that their common speed  $\alpha_c \equiv |\frac{d\alpha}{d\xi}|$  is a decreasing function of  $\alpha$ . Since  $K_0(2\alpha)$  is an exponentially small when  $\alpha \gg 1$ , the two-spot dynamics (5.12) is metastable in this limit, and is similar to the metastable repulsive dynamics studied in [25] for a two-spot solution to the GM model in  $\mathbb{R}^2$ .

Next, we discuss the possibility of dynamically-triggered instabilities induced by the slow evolution of the two-spot pattern. With regards to spot self-replication, we observe that since the two spots are dynamically repelling, and  $S_c$  is a monotonically increasing function of  $\alpha$  (see Fig. 13(c)), it follows that a dynamically-triggered spot self-replication instability will occur when  $\mathcal{A} > \mathcal{A}_{sm} \approx 3.98$ . To illustrate this let  $\mathcal{A} = 4.0$ . Then, the dashed curve of  $S_c$  versus  $\alpha$  in Fig. 13(c) shows that  $S_c > \Sigma_2$  only if  $\alpha \geq 1.81$ . Now consider an initial two-spot quasi-equilibrium solution with  $\alpha = 1$  at  $t = 0$ . For this initial value of  $\alpha$ , then  $\mathcal{A} > \mathcal{A}_f$  (see Fig. 13(b)). Then, since  $\alpha' > 0$  and  $\alpha \rightarrow \infty$  as  $t \rightarrow \infty$  from the ODE (5.12), it follows that  $\alpha = 1.81$  at some long time  $t = \mathcal{O}(\varepsilon^{-2})$ , which triggers the spot self-replication instability. From Principal Result 3.2 of §3, the spots will split in a direction perpendicular to the  $x$ -axis.

Thus, for the GS model (1.1), we conclude that there is a wide parameter range for which two spots in  $\mathbb{R}^2$  will undergo a dynamically-triggered spot self-replication event that is induced by their slow repulsive dynamics. In contrast, we remark that since the Schnakenburg model of [38] involves the Neumann Green's function rather than the reduced-wave Green's function, the infinite-plane problem for this related RD model is ill-posed.

Finally, we remark that the monotone increasing behavior of the Hopf bifurcation threshold  $\tau_{H1}$  versus  $\alpha$  (see Fig. 14(b)), coupled to the repulsive spot dynamics of the two-spot pattern, precludes the existence of any dynamically-triggered oscillatory instability for a two-spot solution in  $\mathbb{R}^2$ . Namely, consider an initial two-spot quasi-equilibrium with initial inter-separation distance  $2\alpha_0$ , and with a fixed  $\tau$  with  $\tau < \tau_{H1}(\alpha_0)$ , where  $\alpha_0 > \alpha_c$ . Then, since  $\alpha$  increases as  $t$  increases, and  $\tau_{H1}$  is monotone increasing in  $\alpha$ , it follows that  $\tau < \tau_{H1}(\alpha)$  for any  $t > 0$ . In a similar way, we can show that there are no dynamically-triggered competition instabilities in  $\mathbb{R}^2$ .

### 5.3 Two-Spot Patterns in a Large Square Domain

Next, we consider a two-spot pattern in the square domain  $[0, L] \times [0, L]$  with spots located symmetrically about the midline of the square at  $\mathbf{x}_{1,2} = (L/2 \pm \alpha, L/2)$ , where  $\alpha > 0$ . For this arrangement,  $\mathcal{G}$  in (2.10) is circulant symmetric, with matrix entries that can be numerically calculated from (A.11) of Appendix A. We fix the parameter values  $D = 1$ ,  $\mathcal{A} = 4.2$ , and  $\varepsilon = 0.02$ . Since the limiting solution for  $L \rightarrow \infty$  reduces to the infinite-plane problem, a large square domain can be used to approximate a two-spot evolution for the infinite-plane problem of §5.2. Our goal here is to examine the asymptotic prediction of spot self-replication.

In Fig. 16 we plot  $S_c$  versus  $\alpha$  for a square of side-lengths  $L = 6, 8, 10$ . By symmetry, the equilibrium spot locations are at  $\alpha_e = L/4$ . In this figure, we also plot the infinite-plane result for  $S_c$  versus  $\alpha$ , obtained from (5.8). The resulting four curves of  $S_c$  versus  $\alpha$  are essentially indistinguishable on the range  $\alpha \ll L$  where the finite-boundary effects are insignificant. From this figure, we observe that the spot-splitting threshold  $S_c = \Sigma_2 \approx 4.31$ , represented by the thin solid line, intersects each of the four curves at some critical values of  $\alpha$ , which initiates a spot self-replication event. We observe from Fig. 16 that  $S_c < \Sigma_2$  when  $\alpha$  becomes close to  $L/2$ . Therefore, for a spot near an edge of the square,



the Neumann boundary condition effectively introduces an image spot outside of the square in close proximity to the interior spot, which then eliminates the possibility of spot self-replication.

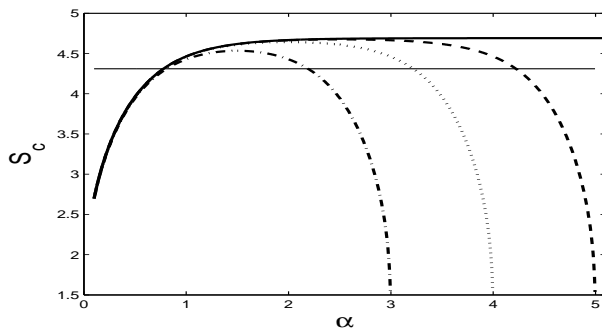


Figure 16. Comparison of two-spot patterns in a square domain and in an infinite domain. Fixing  $\varepsilon = 0.02$ ,  $D = 1$  and  $\mathcal{A} = 4.2$ , we plot  $S_c$  vs.  $\alpha$  for an infinite domain (heavy solid curve), and for square domains with side-lengths  $L = 10$  (dashed curve),  $L = 8$  (dotted curve), and  $L = 6$  (dot-dashed curve). The thin solid line is the peanut-splitting threshold  $\Sigma_2 \approx 4.31$ , which intersects the four curves at  $\alpha_s \approx 0.775$  for the infinite domain,  $\alpha_{s1} \approx 0.775$  for  $L = 10$ ,  $\alpha_{s2} \approx 0.780$  for  $L = 8$ , and  $\alpha_{s3} \approx 0.805$  for  $L = 6$ .

For  $L = 8$ , we now compare our asymptotic prediction for spot self-replication with corresponding full numerical results computed from (1.1) using VLUGR (cf. [6]). We take an initial two-spot pattern with  $\alpha = 0.4 < \alpha_s$  at time  $t = 0$ . At this initial time, we calculate from (2.22) that  $S_c \approx 3.77$ , so that the initial two-spot pattern is stable to spot self-replication. Then, since the equilibrium state is at  $\alpha_e = 2.0$  and the two-spot dynamics is repulsive, it follows that  $\alpha$  increases as  $t$  increases and will eventually exceed the spot-splitting threshold  $\alpha_{s3} \approx 0.780$ . This prediction of a dynamically-triggered instability, which very closely approximates that for the infinite-plane problem of §5.2, is confirmed by the full numerical results shown in Fig. 17.

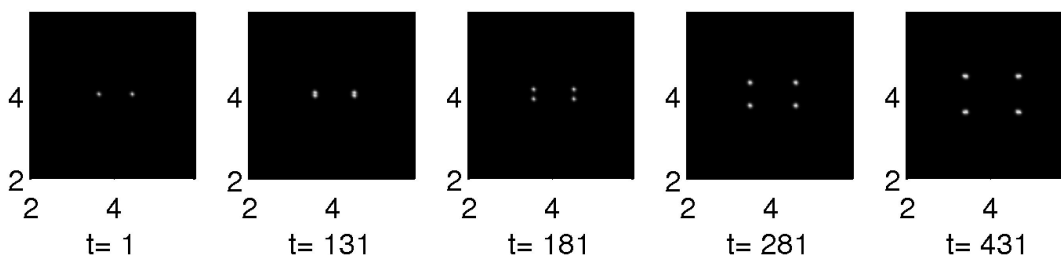


Figure 17. A two-spot pattern in the square  $[0, 8] \times [0, 8]$ . Let  $\mathcal{A} = 4.2$ ,  $D = 1.0$ ,  $\varepsilon = 0.02$  with initial spot locations  $\mathbf{x}_{1,2} = (4 \pm 0.4, 4)$  at time  $t = 0$ . Then,  $S_c \approx 3.77$  at  $t = 0$ , but  $S_c > \Sigma_2 \approx 4.31$  at a later time. The numerical solution to (1.1), represented as a gray-scale image of  $v$ , is plotted in the zoomed region  $[2, 6] \times [2, 6]$  at times  $t = 1, 41, 131, 181, 231, 281, 331, 431$ . The spots undergo splitting in a direction perpendicular to their motion consistent with Principal Result 3.2.

## 6 Symmetric Spot Patterns in the Square and Disk

In this section, we implement the asymptotic theory of §2–4 to study competition, oscillatory, and spot self-replication instabilities for various spot patterns for which the Green’s matrix  $\mathcal{G}$  in (2.9) has a circulant matrix structure. The

thresholds for these instabilities are favorably compared with results from full numerical simulations obtained by using the PDE solver VLUGR (cf. [6]) for a square domain and the finite element code of [36] for the disk.

In all of the numerical simulations below and in §7 we have set  $\varepsilon = 0.02$  so that  $\nu = -1/\ln \varepsilon = 0.2556$ . For given GS parameters  $\mathcal{A}$  and  $D$ , and for an initial configuration of spot locations  $\mathbf{x}_1, \dots, \mathbf{x}_k$ , we compute the source strengths  $S_1, \dots, S_k$  from the nonlinear algebraic system (2.7). The initial condition for the full numerical simulations is the quasi-equilibrium solution (2.8) with the values for  $V_j(0)$  as plotted in Fig. 1(b), corresponding to the computed values of  $S_j$ . Since this initial condition provides a decent, but not sufficiently precise, initial  $k$ -spot pattern, we only begin to track the spot locations from the full numerical simulations after the completion of a short transient period. To numerically identify the locations of the spots at any time, we determine all local maxima of the computed solution  $v$  by identifying the maximal grid values. This simple procedure is done since it is expensive to interpolate the grid values to obtain more accurate spot locations at every time step. In this way, both the spatial trajectories and the amplitudes of the spots are obtained from the full numerical results. In many of the numerical experiments below, we show a gray-scale contour plot of the numerical solution for  $v$ . The bright (white) regions correspond to the spot regions where  $v$  has a large amplitude, while the dark region is where  $v$  is exponentially small.

### 6.1 A Four-Spot Pattern in the Unit Square

We first consider a four-spot pattern in the unit square  $\Omega = [0, 1] \times [0, 1]$  with  $\varepsilon = 0.02$  fixed. The four spots are centered at the corners of a square symmetrically placed inside  $\Omega$  as shown in Fig. 20. For this configuration, the Green's matrix  $\mathcal{G}$  is circulant symmetric, so that there is a solution to (2.10) for which the spots have a common source strength  $S_c$ . From (2.22), this common source strength  $S_c$  satisfies the nonlinear algebraic equation

$$\mathcal{A} = S_c + 2\pi\nu\theta S_c + \nu\chi(S_c), \quad \mathcal{A} = \mathcal{A}\varepsilon/(\nu\sqrt{D}), \quad \nu \equiv -1/\ln \varepsilon, \quad \theta \equiv R_{1,1} + G_{1,2} + G_{1,3} + G_{1,4}. \quad (6.1)$$

Numerical values for  $R_{11}$  and  $G_{1j}$  for  $j = 2, \dots, 4$  are obtained from the reduced-wave Green's function for the unit square as given in (A.11) of Appendix A.

We let  $r$  denote the distance from each spot to the center  $(0.5, 0.5)$  of the square, so that  $r \in (0, 1/\sqrt{2})$ . For  $D = 1$ , in Fig. 18 we plot the phase diagram of  $\mathcal{A}$  versus  $r$  for  $0.1 \leq r \leq 0.7$ . In this phase diagram, the spot self-replication threshold is obtained by setting  $\chi(\Sigma_2) \approx -1.79$  and  $\Sigma_2 \approx 4.31$  in (6.1). The existence threshold for the four-spot quasi-equilibrium pattern is obtained by determining, for each fixed  $r$ , the minimum point of the curve  $\mathcal{A}$  versus  $S_c$  from (6.1). Finally, as similar to the case of a two-spot pattern on the infinite plane as studied in §5.2, the competition instability threshold in Fig. 18 is set by the sign-fluctuating eigenvector. Therefore, from (4.24) this threshold of  $\mathcal{A}$  versus  $r$  is obtained by numerically solving

$$\chi'(S_c) + 2\pi \sum_{m=1}^4 (-1)^{m-1} a_m = -\nu^{-1}; \quad a_1 = R_{11}; \quad a_j = G_{1j}, \quad j = 2, \dots, 4, \quad (6.2)$$

together with (6.1). Recall that a plot of  $\chi'(S_c)$ , as needed in (6.2), was shown in Fig. 10(a).

The phase diagram of Fig. 18 consists of four distinct parameter regimes. In Regime  $\sigma$  the four-spot quasi-equilibrium solution does not exist. In Regime  $\beta$  the quasi-equilibrium solution exists but is unstable to a competition instability. In Regime  $\zeta$  the solution is unstable to an oscillatory profile instability when  $\tau$  exceeds a Hopf bifurcation threshold  $\tau_H$ . In Regime  $\theta$  the solution is unstable to spot self-replication.

Next, we calculate the Hopf bifurcation threshold  $\tau_H$  and the pure imaginary eigenvalue  $\text{Im}\lambda$  corresponding to an oscillatory profile instability. For  $D = 1$ , and for a few values of  $\mathcal{A}$ , in Fig. 19(a) we plot  $\tau_H$  vs.  $r$  associated with

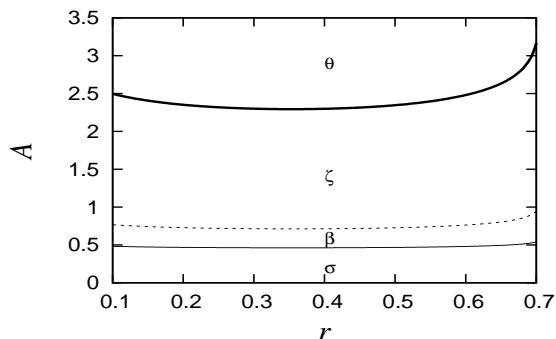


Figure 18. For  $\varepsilon = 0.02$ ,  $k = 4$ ,  $D = 1$ , we plot the phase diagram  $A$  vs.  $r$  for a four-spot quasi-equilibrium pattern in a square with spots centered along the diagonals of the unit square at a distance  $r$  from the midpoint of the square.

the in-phase oscillation eigenvector  $(1, 1, 1, 1)^T$  (heavy solid curves) and with the out-of-phase oscillation eigenvector  $(1, -1, 1, -1)^T$  (thin solid curves). The dotted portions of the heavy solid curves correspond to where a competition instability occurs. From Fig. 19(a), we observe that  $\tau_H$  is set by the synchronous oscillatory instability and that, at each fixed  $r$ ,  $\tau_H$  increases with  $A$ . In Fig. 19(b), we plot  $\text{Im}\lambda$  vs.  $r$  at the Hopf threshold. From this figure, we observe that as  $r$  decreases, the pure imaginary eigenvalue for the out-of-phase oscillation eigenvector  $(1, -1, 1, -1)^T$  (thin solid curve) approaches zero, which implies the onset of a competition instability with eigenvalue  $\lambda = 0$ .

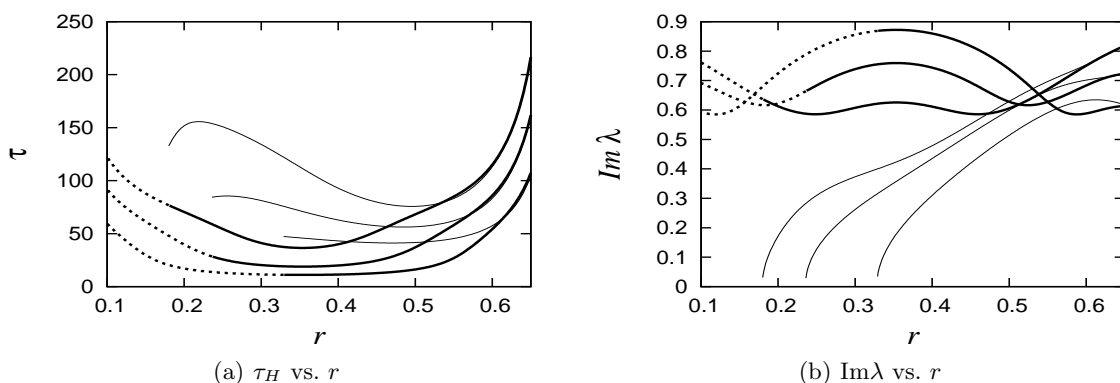


Figure 19. Fix  $\varepsilon = 0.02$ ,  $k = 4$ , and  $D = 1$ . For a few values of  $A$  we plot the Hopf bifurcation threshold  $\tau_H$  (left figure) and pure imaginary eigenvalue  $\lambda$  (right figure) for a four-spot pattern in the unit square. The in-phase oscillation eigenvector  $(1, 1, 1, 1)^T$  corresponds to the heavy solid curves, while the out-of-phase oscillation eigenvector  $(1, -1, 1, -1)^T$  corresponds to the thin solid curves. From top to bottom, the three heavy solid curves at  $r = 0.65$  correspond to  $A = 1.0, 0.9, 0.8$ .

We now perform a few numerical experiments to test the predictions of the asymptotic theory. In Experiments 6.1–6.3 we fix  $D = 1$  and  $\varepsilon = 0.02$ , and we vary  $A$ ,  $\tau$ , and the initial distance  $r(0)$  of the spots from the midpoint of the square. In these experiments we will focus on competition and oscillatory instabilities of the four-spot pattern.

Experiment 6.1: (Slow Drift of the Spots): We fix  $r(0) = 3/(5\sqrt{2})$  and  $A = 1$ , corresponding to Regime  $\zeta$  of the phase diagram in Fig. 18. We set  $\tau = 1$ , which is below the numerically computed Hopf bifurcation threshold of  $\tau_H = 44.8$  at  $r(0)$ . Thus, the initial four-spot pattern is predicted to be stable to all three instabilities. From the dynamics in Principal Result 3.1 we can verify that the four spots drift slowly towards the midpoint of the square,

and reach an equilibrium state with  $r \approx 1/(2\sqrt{2})$  for  $t \gg 1$ . For  $\tau = 1$ , there is no dynamically-triggered oscillatory profile instability. The full numerical results in Fig. 20 confirm this prediction of the asymptotic theory.

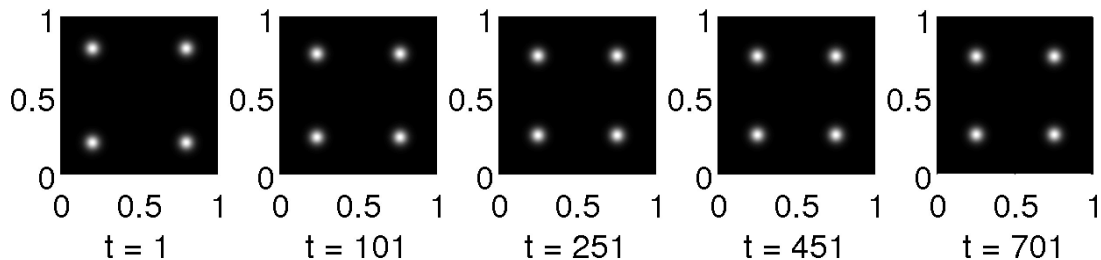


Figure 20. *Experiment 6.1:* Fix  $\varepsilon = 0.02$ ,  $k = 4$ ,  $D = 1$ ,  $A = 1.0$ , and  $\tau = 1$ . Starting from  $r(0) = 3/(5\sqrt{2})$ , we observe the slow drift of the four spots towards their equilibrium locations within the unit square. At  $t = 701$ , they are at (approximately)  $(0.75, 0.75)$ ,  $(0.25, 0.75)$ ,  $(0.25, 0.25)$  and  $(0.75, 0.25)$ , namely  $r = 0.5/\sqrt{2}$ .

Experiment 6.2: (*A Competition Instability*): Let  $r = 1/(2\sqrt{2})$ , corresponding (roughly) to the equilibrium distance from the midpoint for the four-spot pattern. We choose  $A = 0.6$  corresponding to Regime  $\beta$  in the phase diagram of Fig. 18. In addition, we take  $\tau = 1$  for which  $\tau < \tau_H$ . Therefore, we predict that the initial four-spot pattern is unstable to a competition instability. This is confirmed by the full numerical results computed from the GS model (1.1) shown in Fig. 21. In this figure, we observe that the two spots at  $(0.25, 0.75)$  and  $(0.75, 0.25)$  decay very fast, and that after  $t = 20$ , these two spots are annihilated. The spot amplitudes as a function of  $t$  are shown in Fig. 22.

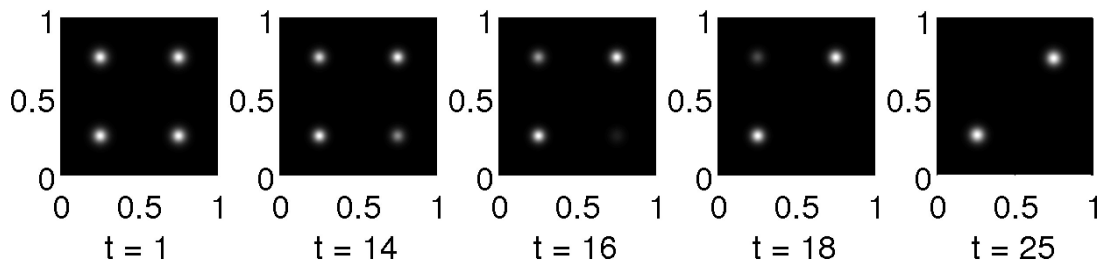


Figure 21. *Experiment 6.2:* Fix  $\varepsilon = 0.02$ ,  $D = 1$ ,  $A = 0.6$ , and  $\tau = 1$ . This plot shows a competition instability for the four-spot pattern with spots initially located at a distance  $r = 1/(2\sqrt{2})$  from the midpoint of the square.

Experiment 6.3: (*An Oscillatory Instability*): We fix  $r = 1/(2\sqrt{2})$  at  $t = 0$  and choose  $A = 0.8$ . This choice corresponds to Regime  $\zeta$  in Fig. 18. With these parameter values, the numerically computed Hopf bifurcation threshold predicted by the asymptotic theory is  $\tau_H = 11.0$  when  $t = 0$ . To confirm this prediction, we compute full numerical solutions to the GS model (1.1) for  $\tau = 10, 11, 12$ . For these three choices of  $\tau$ , in Fig. 23 we plot the numerically computed amplitude  $v_m = v_m(t)$  of the spot at  $(0.75, 0.75)$ . Our full numerical computations show that all the spot amplitudes coincide with the one in Fig. 23. This synchronous oscillatory instability was predicted by the asymptotic theory. Our numerical results show that an unstable oscillation develops on the range  $11 < \tau < 12$ , which was

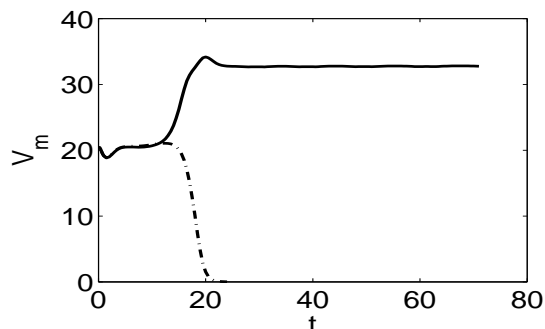


Figure 22. *Experiment 6.2:* Fix  $\varepsilon = 0.02$ ,  $r(0) = 1/(2\sqrt{2})$ ,  $D = 1$ ,  $A = 0.6$ , and  $\tau = 1$ . We plot the amplitude of the two spots at  $(0.25, 0.25)$  (heavy solid curve) and  $(0.25, 0.75)$  (dashed curve).

closely predicted by our asymptotic theory. Our numerical results show that this unstable oscillation leads to the annihilation of the spot (not shown). As a result, we conjecture that the Hopf bifurcation is subcritical.

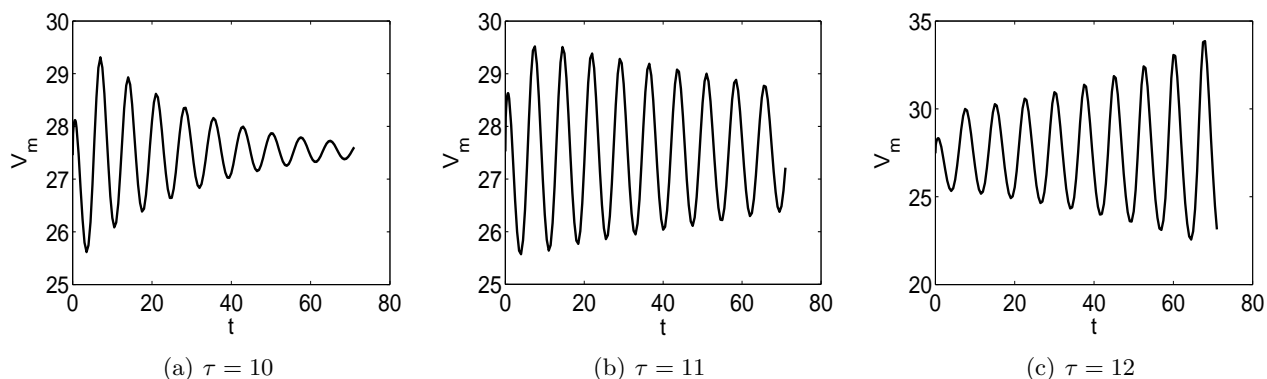


Figure 23. *Experiment 6.3:* Fix  $\varepsilon = 0.02$ ,  $r(0) = 1/(2\sqrt{2})$ ,  $D = 1$ , and  $A = 0.8$ . For the initial four-spot pattern in a square, we plot the numerically computed spot amplitude  $v_m = v_m(t)$  for the spot at  $(0.75, 0.75)$  for  $\tau = 10, 11, 12$ . When  $\tau = 12 > \tau_H$ , the oscillation is unstable.

## 6.2 A One-Spot Pattern in the Unit Disk

Let  $\Omega$  be the unit disk, and consider a one-spot quasi-equilibrium solution centered at  $\mathbf{x}_1 \in \Omega$ , with  $r \equiv |\mathbf{x}_1|$ . From (2.22) and (2.5), the source strength  $S$  for this spot is determined in terms of  $A$  by

$$A = S + 2\pi\nu R_{1,1}S + \nu\chi(S), \quad A = \mathcal{A}\varepsilon/(\nu\sqrt{D}), \quad \nu \equiv -1/\ln \varepsilon. \quad (6.3)$$

Here the regular part  $R_{1,1} \equiv R(\mathbf{x}_1; \mathbf{x}_1)$  of  $G$ , which depends on  $r = |\mathbf{x}_1|$ , is calculated from (A.8) of Appendix A. For this case, the spot dynamics from Principal Result 3.1 shows that the spot will drift with speed  $\mathcal{O}(\varepsilon^2)$  along a ray towards the center of the disk.

For a one-spot solution centered at the origin, the spot self-replication threshold  $A = A_s(D)$  is given by

$$A_s(D) = \frac{\varepsilon}{\nu\sqrt{D}} [\Sigma_2 (1 + 2\pi\nu R_{1,1}) + \nu\chi(\Sigma_2)], \quad (6.4)$$

where  $\chi(\Sigma_2) \approx -1.79$  and  $\Sigma_2 \approx 4.31$ . Here  $R_{1,1} \equiv R_{1,1}(\mathbf{0}; \mathbf{0})$  is given explicitly in (2.15). Moreover, the existence threshold for a one-spot solution centered at the origin is obtained by replacing  $\Sigma_2$  in (6.4) with  $S$ , and then computing

the minimum value, denoted by  $A_f = A_f(D)$ , of the resulting expression with respect to  $S$ . The self-replication and existence thresholds for a one-spot solution centered at the origin are shown in the phase diagram of Fig. 24.

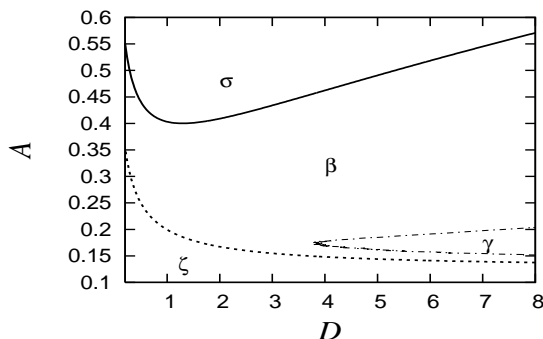


Figure 24. Plot of the phase diagram  $A$  vs.  $D$  for  $\varepsilon = 0.02$  for a one-spot solution centered at the origin in the unit disk. It is only in Regime  $\sigma$  that spot self-replication can occur. The solid curve is the spot self-replication threshold  $A_s(D)$  of (6.4), while the lower dotted curve is the existence threshold  $A_f(D)$ . In Regime  $\zeta$  a one-spot solution does not exist. In Regimes  $\beta$  and  $\gamma$  an oscillatory instability for a spot at the origin occurs only if  $\tau > \tau_H(0)$ . In Regime  $\gamma$ ,  $\tau_H''(0) > 0$ , while in Regime  $\beta$ ,  $\tau_H''(0) < 0$ , where  $\tau_H = \tau_H(r)$ . Thus, only in Regime  $\gamma$  can we find a value of  $\tau$  and an initial spot location for which a dynamical oscillatory instability is triggered for a spot that slowly drifts to the center of the unit disk.

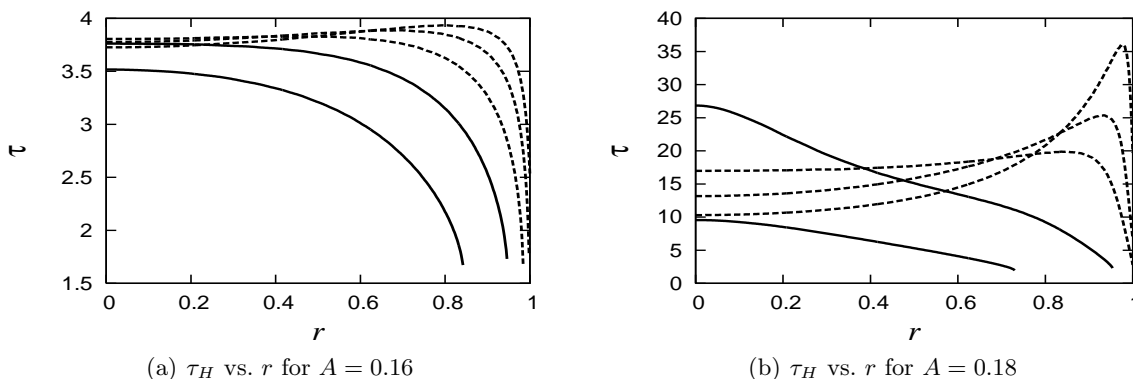


Figure 25. A One-spot solution in the unit disk at a distance  $r = |\mathbf{x}_1|$  from the origin. Plots of  $\tau_H$  vs.  $r$  for different  $A$  and  $D$ . (a) Fix  $A = 0.16$ . The solid curves are for  $D = 4, 5$ , arranged from lower to upper  $y$ -intercepts, respectively. The dashed curves are for  $D = 6, 7, 8$ , arranged from upper to lower  $y$ -intercepts, respectively. (b) Fix  $A = 0.18$ . The solid curves are for  $D = 2, 3$  arranged from lower to upper  $y$ -intercepts, respectively. The dashed curves are for  $D = 4, 3, 5, 6$ , arranged from upper to lower  $y$ -intercepts, respectively.

Next, we study oscillatory instabilities of the spot profile. For each  $r = |\mathbf{x}_1|$  in  $0 < r < 1$ , we suppose that  $A > A_f(D, r)$ , where  $A_f = A_f(D, r)$  is the existence threshold for a one-spot quasi-equilibrium solution centered at  $\mathbf{x}_1$ . In Fig. 25(a), we plot the numerically computed Hopf bifurcation threshold  $\tau_H$  versus  $r$  for fixed  $A = 0.16$ , but for different values of  $D$ . The computations were done using the global eigenvalue problem of Principal Result 4.3. For  $D = 4$  and  $D = 5$  we observe from Fig. 25(a) that the maximum of  $\tau_H = \tau_H(r)$  is obtained at the equilibrium location  $r = 0$ , and that  $\tau_H$  decreases monotonically as  $r$  increases. In contrast, for  $D = 6, 7, 8$  Fig. 25(a) shows that the curves of  $\tau_H = \tau_H(r)$  are convex near  $r = 0$ , so that  $\tau_H$  has a local minimum at  $r = 0$ . Therefore, when  $D$  is sufficiently large, we conclude that we can obtain a dynamically-triggered oscillatory instability in the spot

amplitude. To illustrate this, suppose that  $D = 8$ . Then, we calculate  $\tau_H(0) \approx 3.73$  and  $\tau_H(0.612) \approx 3.88$ . Suppose that we take  $\tau = 3.8$  with the initial spot location at time  $t = 0$  at  $r = 0.612$ . Then, since  $\tau < \tau_H(0.612)$ , the spot is stable at  $t = 0$ . However, since the motion of the spot is towards the origin and  $\tau > \tau_H(0)$ , it follows that a dynamically-triggered oscillatory profile instability will occur before the spot reaches the center of the disk. A qualitatively similar scenario occurs for other values of  $A$ . In particular, for  $A = 0.18$ , in Fig. 25(b) we plot  $\tau_H$  versus  $r$  for various fixed values of  $D$ . For the values  $D = 4.3, 5, 6$ , we observe that  $\tau_H(r)$  has a local minimum at the equilibrium location  $r = 0$ . Thus, for these values of  $D$ , we can choose a value of  $\tau$  and an initial spot location that will lead to a dynamically-triggered oscillatory instability.

For a spot centered at the origin of the unit disk, and with  $\varepsilon = 0.02$ , in Fig. 26 we plot the Hopf bifurcation threshold  $\tau_H$  vs.  $D$  for  $A = 0.16, \dots, 0.21$ . We observe that each curve is not monotone in  $D$ , and has a local maximum at some value of  $D$ , with  $\tau_H$  decreasing as  $D$  increases.

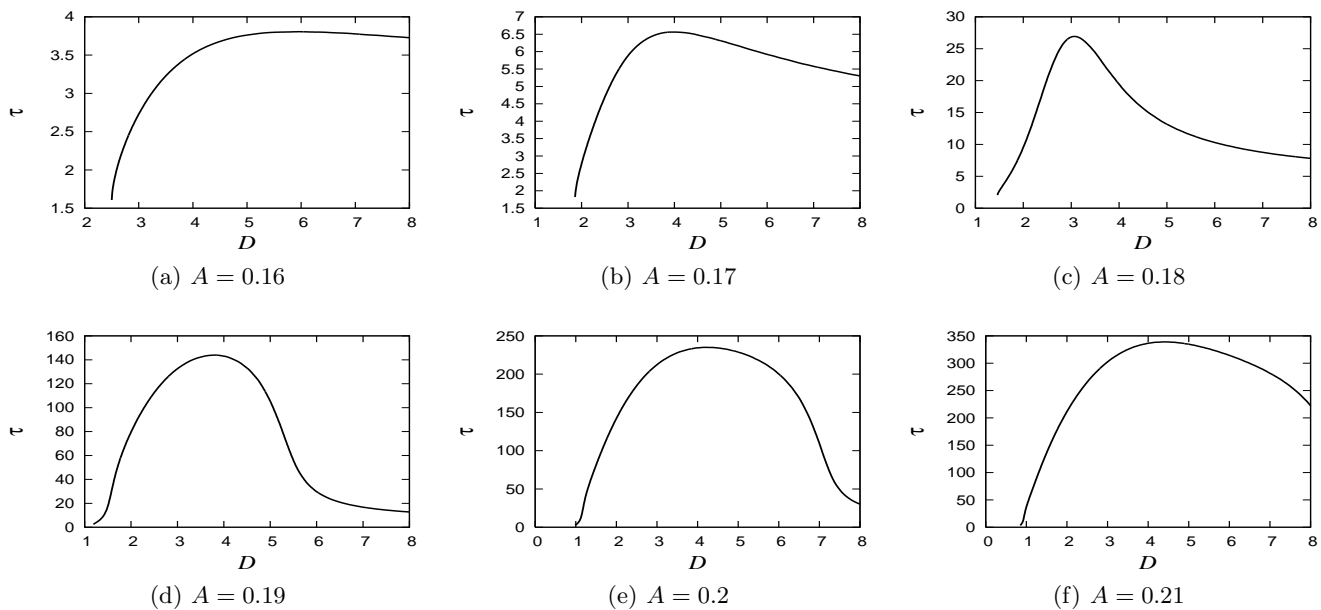


Figure 26. One-spot solution centered at the origin in the unit disk. The Hopf bifurcation threshold  $\tau_H$  vs.  $D$  is plotted for  $A = 0.16, \dots, 0.21$ . This shows that  $\tau_H(D)$  has a maximum at some critical value of  $D$ .

In Fig. 24 we plot a phase diagram in the  $A$  versus  $D$  parameter plane for  $\varepsilon = 0.02$  for a one-spot solution centered at the origin in the unit disk. From this figure, there are four distinct regions with different solution behavior. In Regime  $\sigma$  the spot at the origin will undergo self-replication. In Regime  $\zeta$  there is no one-spot solution centered at the origin. In Regime  $\beta$  the one-spot solution undergoes a Hopf bifurcation if  $\tau$  is large enough and the Hopf bifurcation threshold  $\tau_H = \tau_H(r)$ , shown in Fig. 25, satisfies  $\tau_H''(0) < 0$ , and so has a local maximum at  $r = 0$ . Finally, in Regime  $\gamma$ , the one-spot solution has a Hopf bifurcation if  $\tau$  is large enough, but now the Hopf bifurcation threshold satisfies  $\tau_H''(0) > 0$ , and so has a local minimum at  $r = 0$ . Therefore, in Regime  $\gamma$  one can choose an initial spot location inside the unit disk, together with a value of  $\tau$ , for which a dynamic oscillatory instability of a one-spot quasi-equilibrium solution will be triggered as the spot drifts towards its equilibrium location at the center of the unit disk.

We now argue that the solid curve  $A = A_s(D)$  in Fig. 24 not only corresponds to the threshold condition for the self-replication of a spot centered at the origin, but also corresponds to the threshold for a dynamically-triggered spot self-

replication event for a one-spot pattern in the unit disk starting from the initial spot location at radius  $r = |\mathbf{x}_1|$  with  $0 < r < 1$ . To show this, we differentiate (6.3) with respect to  $r$  to obtain that  $dS/dr = -2\pi\nu S (dR_{1,1}/dr) + \mathcal{O}(\nu^2)$ . It is readily verified numerically by using (A.8) of Appendix A that  $R_{1,1}$  has a global minimum at  $r = 0$  with  $R_{1,1}$  an increasing function of  $r$  on  $0 < r < 1$ , and  $R_{1,1} \rightarrow +\infty$  as  $r \rightarrow 1^-$ . Therefore, we have  $dS/dr < 0$  on  $0 < r < 1$ , so that  $S$  is a monotone decreasing function of  $r$  for any fixed values of  $A$  and  $D$ . Moreover, by differentiating (6.3), we readily observe that  $S$  is a monotone increasing function of  $A$  at each fixed  $r$  and  $D$ . Therefore, it follows that the threshold curve for a dynamically-triggered spot self-replication event is obtained by setting  $S = \Sigma_2$  and  $r = 0$  in (6.3) to obtain  $A_s(D)$  as given in (6.4). Therefore, in Regime  $\sigma$  of Fig. 24 it follows that we can choose an initial spot location and a value of  $A$  for which a dynamic spot self-replication instability will occur for a spot which slowly drifts towards the center of the unit disk.

*Experiment 6.4: (One-spot solution in the unit disk: Comparison with full numerical simulations):* For a one-spot solution centered at the origin of the unit disk we now compare our numerically computed Hopf bifurcation threshold, as obtained from our global eigenvalue problem, with full numerical results as computed from the full GS model (1.1). For three values of  $\tau$ , in the top row of Fig. 27, we plot  $v_m \equiv v(0, t)$  versus  $t$  for the GS parameters  $\varepsilon = 0.02$ ,  $A = 0.16$ , and  $D = 4$ . This figure shows that an unstable oscillation occurs near  $\tau = 3.4$ , which agrees rather closely with the Hopf bifurcation threshold  $\tau_H \approx 3.5$  computed from our global eigenvalue formulation of Principal Result 4.3 (see Fig. 25(a)). We remark that if we changed the parameters to  $A = 0.18$  and  $D = 6$ , then  $\tau_H \approx 10.3$  (see Fig. 25(b)), as predicted by our global eigenvalue problem. This compares rather closely with the result  $\tau \approx 10$  computed from the full GS model (1.1) observed in the bottom row of Fig. 27.

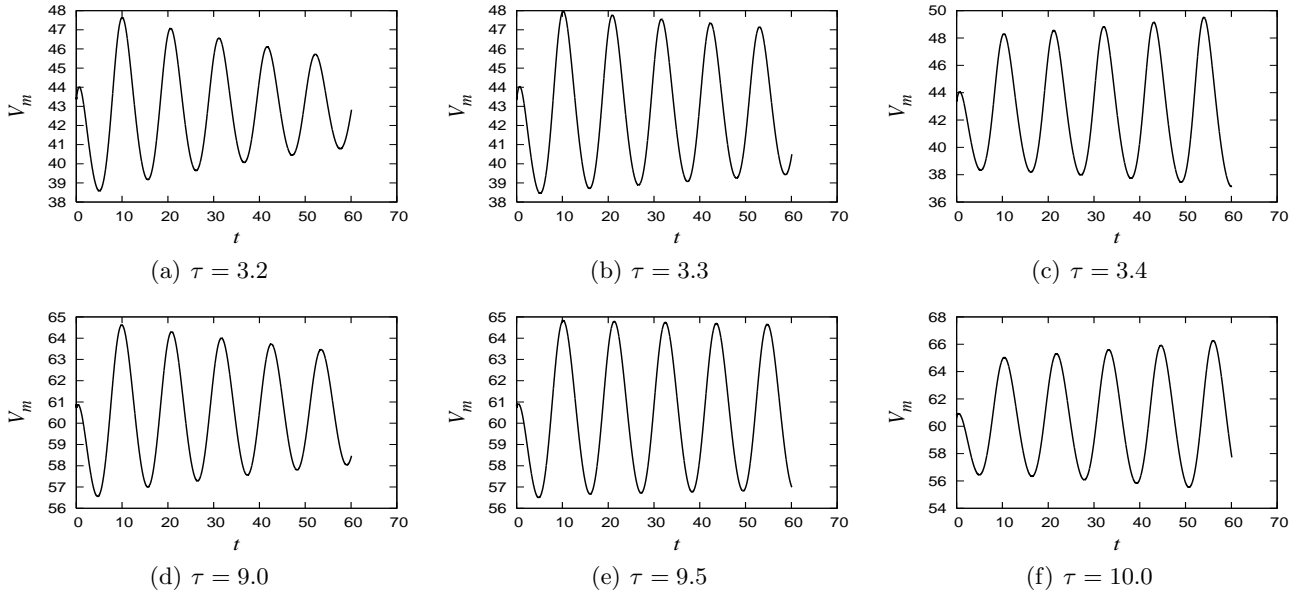


Figure 27. *Experiment 6.4: One-spot solution with spot at the center of the unit disk. We fix  $\varepsilon = 0.02$ . Top Row: For  $A = 0.16$  and  $D = 4$ , the spot amplitude  $v_m$  vs.  $t$  is plotted for (a)  $\tau = 3.2$ ; (b)  $\tau = 3.3$ ; (c)  $\tau = 3.4$ . Bottom Row: For  $A = 0.18$  and  $D = 6$ , the spot amplitude  $v_m$  vs.  $t$  is plotted for (d)  $\tau = 9.0$ ; (e)  $\tau = 9.5$ ; (f)  $\tau = 10.0$ .*



| $D$ | $r_e$   | $D$ | $r_e$   |
|-----|---------|-----|---------|
| 0.8 | 0.45779 | 2.0 | 0.45540 |
| 1.0 | 0.45703 | 3.0 | 0.45483 |
| 1.3 | 0.45630 | 4.0 | 0.45454 |
| 1.5 | 0.45596 | 5.0 | 0.45436 |

Table 1. Equilibrium ring radius  $r_e$  for a two-spot pattern of the form (6.5) in the unit disk for different values of  $D$ .

### 6.3 A One-Ring Pattern of $K$ -Spots in the Unit Disk

Next, we consider the special case when  $k$  spots are equally-spaced on a ring of radius  $r$  centered at the origin of the unit disk. Representing points as complex numbers in the unit disk, the centers of the spots are at

$$\mathbf{x}_j = re^{2\pi ij/k}, \quad j = 1, \dots, k, \quad i \equiv \sqrt{-1}. \quad (6.5)$$

For this symmetric arrangement of spots, the matrix  $\mathcal{G}$  in (2.10) is circulant symmetric and is a function of the ring radius  $r$ . Hence,  $\mathcal{G}\mathbf{e} = \theta\mathbf{e}$  with  $\mathbf{e} = (1, \dots, 1)^T$ , where  $\theta = p_k(r)/k$  with  $p_k(r) \equiv \sum_{i=1}^k \sum_{j=1}^k \mathcal{G}_{i,j}$ . For  $D \gg 1$ , we can analytically determine a two-term expansion for  $p_k(r)$  by using (2.12), the simple explicit form (A.9) for the Neumann Green's function, and Proposition 4.3 of [32]. In this way, for  $D \gg 1$ , we get

$$p_k(r) \equiv \sum_{i=1}^k \sum_{j=1}^k \mathcal{G}_{i,j} \sim \frac{k^2 D}{|\Omega|} + \sum_{i=1}^k \sum_{j=1}^k \mathcal{G}_{i,j}^{(N)} = \frac{k^2 D}{\pi} - \frac{k}{2\pi} \left[ \ln(kr^{k-1}) + \ln(1 - r^{2k}) - r^2 k + \frac{3k}{4} \right] + \mathcal{O}(D^{-1}). \quad (6.6)$$

Since  $\mathcal{G}$  is circulant, (2.10) has a solution for which the source strengths  $S_j$  for  $j = 1, \dots, k$  have a common value  $S_c$ . From (2.22) of §2, it follows that  $S_c$  satisfies the scalar nonlinear algebraic equation

$$\mathcal{A} = S_c \left( 1 + \frac{2\pi\nu}{k} p_k(r) \right) + \nu\chi(S_c), \quad \mathcal{A} = \frac{\varepsilon}{\nu\sqrt{D}} \mathcal{A}, \quad \nu = \frac{-1}{\ln \varepsilon}. \quad (6.7)$$

To determine the dynamics of the  $k$  spots, we calculate  $\mathbf{f}_j$  in (3.3) as  $\mathbf{f}_j = \pi k^{-1} S_c p'_k(r) e^{2\pi ij/k}$ . Then, the dynamics (3.7) of Principal Result 3.1 shows that all the spots remain on a ring of radius  $r(t)$ , which satisfies the ODE

$$\frac{dr}{dt} \sim -\frac{\pi\varepsilon^2}{k} \gamma(S_c) S_c p'_k(r). \quad (6.8)$$

This ODE is coupled to the nonlinear algebraic equation (6.7) for  $S_c$  in terms of  $r$ .

The equilibrium ring radius  $r_e$  for (6.8) satisfies  $p'_k(r) = 0$ , and is independent of  $\mathcal{A}$ . For a two-spot pattern, where  $k = 2$ , then  $r_e$  is given in Table 1 for various values of  $D$ . There is no simple explicit formula for  $p_k(r)$  when  $D = \mathcal{O}(1)$ . However, for  $D \gg 1$ ,  $p_k(r)$  is given asymptotically in (6.6). By differentiating this asymptotic result, it readily follows that  $r_e$ , for  $D \gg 1$ , is the unique root on  $0 < r_e < 1$  of  $[k-1]/(2k) - r^2 = r^{2k}/(1-r^{2k})$  for any  $k \geq 2$ . It is also readily shown from (6.6) that  $p''_k(r_e) > 0$ , with  $p'_k(r) < 0$  for  $r < r_e$  and  $p'_k(r) > 0$  for  $r > r_e$ . Hence, for  $D \gg 1$ ,  $p_k(r)$  attains its global minimum value at the equilibrium radius  $r_e$ . Therefore, since  $\gamma(S_c) > 0$ , then  $r_e$  is a stable equilibrium point for the ODE (6.8) when  $D \gg 1$  and, moreover,  $r \rightarrow r_e$  for any initial point  $r(0)$ , with  $0 < r(0) < 1$ , as  $t \rightarrow \infty$ . By differentiating (6.7) for the source strength, this condition on  $p_k(r)$  also implies that  $S_c(r)$  has a maximum value at  $r = r_e$  when  $D \gg 1$ .

**Spot Self-Replication Instabilities:** We first discuss spot self-replication instabilities for equally spaced spots on a ring. For  $\varepsilon = 0.02$  and  $D = 3.912$ , in Fig. 28 we plot the minimum value  $\mathcal{A}_f = \mathcal{A}_f(r)$  of  $\mathcal{A}$  for which a quasi-equilibrium ring pattern exists at each fixed  $r$  for  $k = 3, 4, 5$  equally spaced spots on a ring. These plots are obtained

by determining the minimum point of the  $\mathcal{A}$  versus  $S_c$  curve in (6.7). In these plots we also show the spot-splitting threshold  $\mathcal{A}_s = \mathcal{A}_s(r)$  obtained by setting  $S_c = \Sigma_2 \approx 4.31$  and  $\chi(\Sigma_2) \approx -1.79$  in (6.7).

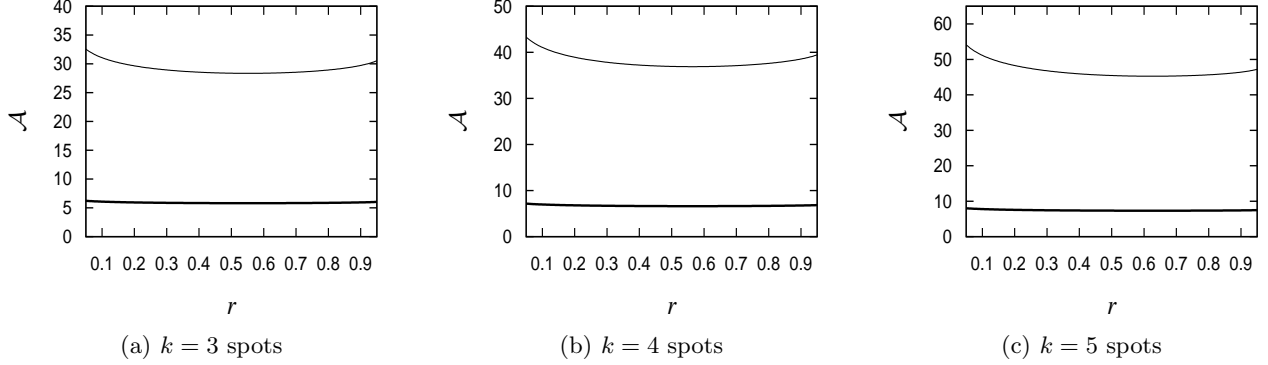


Figure 28. For  $\varepsilon = 0.02$  and  $D = 3.912$  we plot the existence threshold  $\mathcal{A}_f$  (heavy solid curves) and the spot-splitting threshold  $\mathcal{A}_s$  (solid curves) as a function of the ring radius  $r$  for either  $k = 3$  (left figure),  $k = 4$  (middle figure), or  $k = 5$  (right figure) equally spaced spots on a ring.

In Fig. 29(a), we fix  $D = 3.912$  and plot  $S_c$  versus  $r$  for  $k = 3$ ,  $\mathcal{A} = 30$ , for  $k = 4$ ,  $\mathcal{A} = 40$ , and for  $k = 5$ ,  $\mathcal{A} = 48$ . For these three patterns, the equilibrium states are, respectively,  $(r_{e1}, S_{ce1}) = (0.55, 4.57)$ ,  $(r_{e2}, S_{ce2}) = (0.60, 4.70)$ , and  $(r_{e3}, S_{ce3}) = (0.63, 4.58)$ . These points are the circular dots in Fig. 29(a). The square dots in this figure correspond to the spot-replicating threshold  $\Sigma_2 \approx 4.31$ , which occurs at  $r_{s1} = 0.17$ ,  $r_{s2} = 0.14$ , and  $r_{s3} = 0.22$ . Any portion of these curves above the square dots correspond to ring radii where simultaneous spot-splitting will occur.

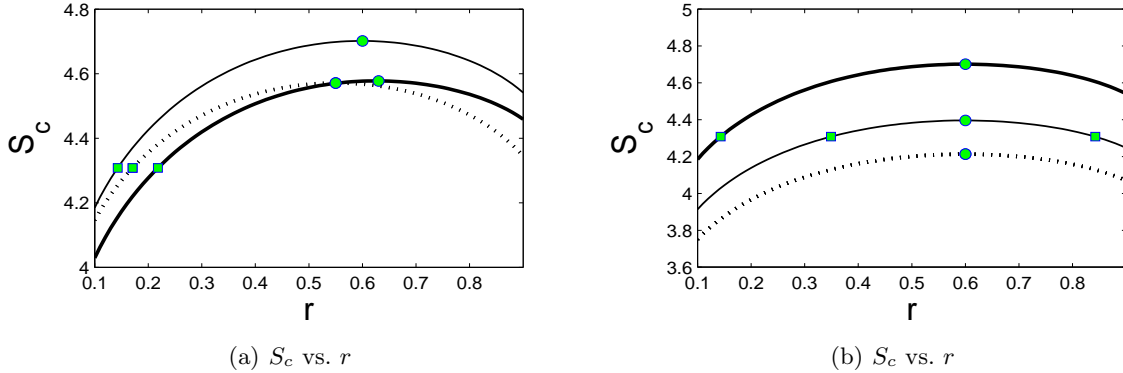


Figure 29. Fix  $D = 3.912$ . (a)  $S_c$  vs.  $r$  with  $k = 3$ ,  $\mathcal{A} = 30$  (dotted curve),  $k = 4$ ,  $\mathcal{A} = 40$  (solid curve) and  $k = 5$ ,  $\mathcal{A} = 48$  (heavy solid curve). (b) Fix  $k = 4$ , we plot  $S_c$  vs.  $r$  with  $\mathcal{A} = 36$  (dotted curve),  $\mathcal{A} = 37.5$  (solid curve), and  $\mathcal{A} = 40$  (heavy solid curve). The square dots indicate spot-splitting thresholds  $S_c = \Sigma_2 \approx 4.31$ , and the circular dots, where  $S_c$  achieves its maxima, denote equilibrium ring radii.

In Fig. 29(b), we fix  $k = 4$  and  $D = 3.912$  and plot  $S_c$  versus  $r$  for  $\mathcal{A} = 36$ ,  $\mathcal{A} = 37.5$ , and  $\mathcal{A} = 40$ . The equilibria are at  $(r_{e4}, S_{ce4}) = (0.60, 4.21)$ ,  $(r_{e5}, S_{ce5}) = (0.60, 4.40)$ , and  $(r_{e2}, S_{ce2}) = (0.60, 4.70)$ , respectively. These points correspond to maxima of  $S_c(r)$ . In this figure the spot-splitting thresholds are the square dots. For  $\mathcal{A} = 36$  and  $k = 4$ , we observe that since  $S_{ce4} = 4.21 < \Sigma_2 \approx 4.31$  when  $r = r_e$ , then  $S_c < \Sigma_2$  for  $r \neq r_e$ , and hence this four-spot pattern is stable to spot self-replication for all values of the ring radius. In contrast, consider the solid curve in Fig. 29(b) for  $\mathcal{A} = 37.5$  and  $k = 4$ . Then, if the initial ring radius  $r(0)$  is in the interval between the two square dots in this

figure, i.e.  $0.35 < r(0) < 0.84$ , we predict that all four spots will begin to split simultaneously starting at  $t = 0$ . Similarly, from the heavy solid curve for  $\mathcal{A} = 40$  and  $k = 4$  in Fig. 29(b), we predict that the four spots will split simultaneously when  $r(0) > r_{s2} = 0.14$ . This prediction is confirmed in the full numerical results below.

The plots of  $\mathcal{A}_s = \mathcal{A}_s(r)$  and  $S_c = S_c(r)$  in Fig. 28 and Fig. 29, respectively, also clearly show the possibility of a dynamically-triggered spot-splitting instability. For instance, consider the solid curve in Fig. 29(b) for  $\mathcal{A} = 37.5$  and  $k = 4$  and an initial ring radius  $r(0) = 0.2$ . This initial point is below the spot-splitting threshold shown in Fig. 28(b), and so the initial pattern is stable to spot-splitting. However, eventually as  $t$  increases the ring radius will cross the threshold value  $r \approx 0.35$  for spot-splitting, and a dynamically-triggered simultaneous spot-splitting event will occur.

This possibility of a dynamically-triggered spot-splitting instability for equally spaced spots on a ring for the GS model is in distinct contrast to the behavior found in [38] for the Schnakenburg model. For this related RD model, the common source strength for a pattern of  $k$  equally-spaced spots on a ring is independent of the ring radius  $r$ . This precludes the existence of a dynamically-triggered spot-splitting instability for the Schakenburg model.

*Experiment 6.5: (One-ring pattern and spot-splitting when  $D \gg \mathcal{O}(1)$ ):* For  $\mathcal{A} = 40$  and  $D = 3.912$ , we consider an initial four-spot pattern with equally-spaced spots on an initial ring of radius  $r = 0.5 > r_{s2}$  at time  $t = 0$ . Since  $S_c \approx 4.69$  at  $t = 0$ , as computed from (6.7), our asymptotic theory predicts that all four spots will begin to split simultaneously at  $t = 0$ . The full numerical results for  $v$  computed from the GS model (1.1), as shown in Fig. 30, confirm this prediction, and also show that the direction of splitting is perpendicular to the direction of spot motion, as predicted by Principal Result 3.2. The splitting process generates an equilibrium pattern of eight equally-spaced spots on a ring.

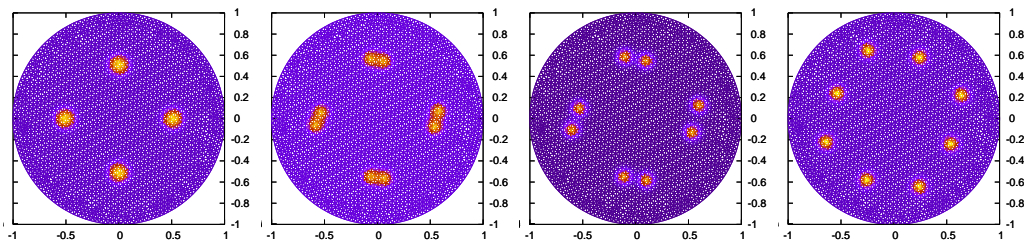


Figure 30. *Experiment 6.5: Fix  $D = 3.912$ ,  $\mathcal{A} = 40$ ,  $\tau = 1$ , and  $\varepsilon = 0.02$ . Consider an initial four-spot pattern with equally-spaced spots on a ring of radius  $r = 0.5$ . The initial common source strength is  $S_c \approx 4.69$ . From left to right we plot  $v$  at times  $t = 4.6, 70, 93, 381$ . All spots undergo splitting, and the dynamics leads to an equilibrium eight-spot pattern on a ring.*

**Phase Diagrams for Existence, Self-Replication, and Competition:** Next, we use our global eigenvalue problem of Principal Result 4.3 of §4.2 to compute the competition instability threshold as a function of the ring radius  $r$  for various values of the parameters. Our results are shown in terms of phase diagrams of  $A$  versus  $r$ .

For  $\varepsilon = 0.02$ , in Fig. 31 we plot the phase diagram  $A$  versus  $r$  for  $D = 0.2$ ,  $D = 1.0$ , and  $D = 5.0$ , for a two-spot quasi-equilibrium solution, showing the thresholds for the existence of a quasi-equilibrium pattern, for a competition instability, and for a spot self-replication instability. For each fixed  $r$ , the existence thresholds in these figures were computed by determining the minimum of the curve  $\mathcal{A}$  versus  $S_c$  in (6.7), while the spot self-replication thresholds were obtained by substituting  $S_c = \Sigma_2 \approx 4.31$  and  $\chi(\Sigma_2) \approx -1.79$  in (6.7). In addition, the competition instability thresholds were computed from (6.9), as we discuss below.

The solution behavior in the four distinct parameter regimes of Fig. 31 is described in the caption of Fig. 31. As

expected, the subfigure for  $D = 0.2$  on the range  $0 \leq r \leq 0.5$  is qualitatively similar to the phase diagram shown in Fig. 14(a) for a two-spot solution on the infinite plane. In Fig. 32 we show similar phase diagrams for  $D = 0.2$  and  $\varepsilon = 0.02$ , but for  $k = 4$ ,  $k = 8$ , and  $k = 16$ , equally-spaced spots on a ring of radius  $r$ .

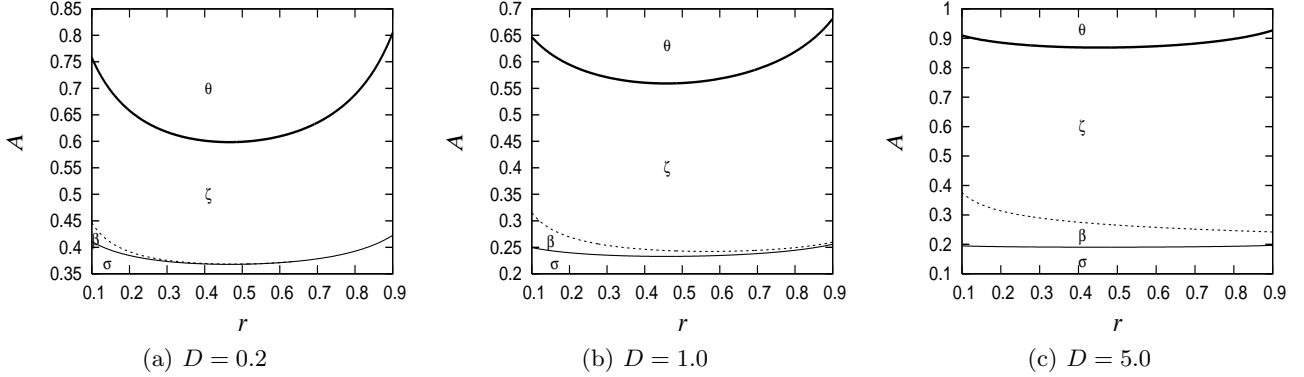


Figure 31. *The phase diagram  $A$  vs.  $r$  for a two-spot quasi-equilibrium solution on a ring of radius  $r$  in the unit disk when  $\varepsilon = 0.02$ . The solid curve is the existence threshold  $A_f$ , the dotted curve is the competition instability threshold; the heavy solid curve is the spot self-replication threshold  $A_s$ . Regime  $\sigma$ : no two-spot solution; Regime  $\beta$ : the two-spot solution is unstable to competition; Regime  $\zeta$  the two-spot solution is unstable to a oscillation if  $\tau > \tau_H(r)$ ; Regime  $\theta$ : the two-spot solution is unstable to spot self-replication. Subfigures from left to right: (a)  $D = 0.2$ ; (b)  $D = 1$ ; (c)  $D = 5$ .*

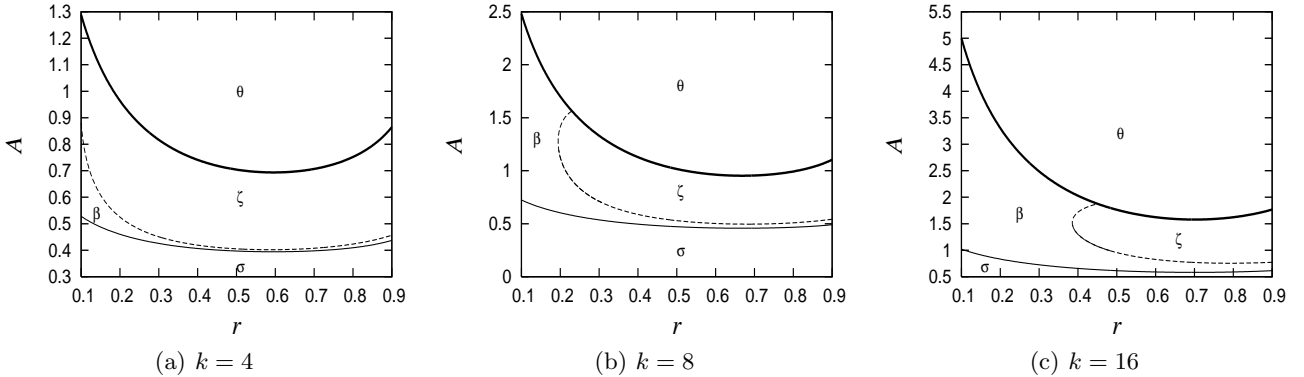


Figure 32. *The phase diagram  $A$  vs.  $r$  for a  $k$ -spot quasi-equilibrium solution on a ring of radius  $r$  in the unit disk with  $\varepsilon = 0.02$  and  $D = 0.2$ . The thin solid curves are the existence threshold  $A_f$  for the quasi-equilibrium solution, the dotted curves are the critical values of  $A$  for a competition instability; the heavy solid curves are the spot self-replication threshold  $A_s$ . In Regime  $\sigma$  the quasi-equilibrium solution does not exist. In Regime  $\beta$  the quasi-equilibrium solution exists but is unstable to competition. In Regime  $\zeta$  the solution is unstable to an oscillatory instability if  $\tau$  exceeds a Hopf bifurcation threshold  $\tau_H(r)$ . In Regime  $\theta$  the solution is unstable to spot self-replication. Subfigures from left to right: (a)  $k = 4$ ; (b)  $k = 8$ ; (c)  $k = 16$ .*

From §4.2 and the result (4.20) for the spectrum of the  $\lambda$ -dependent circulant Green's matrix  $\mathcal{G}_\lambda$ , it follows for  $k = 4$  that the eigenvectors of  $\mathcal{G}_\lambda$  are  $\mathbf{v}_1 = (1, 1, 1, 1)^T$ ,  $\mathbf{v}_2 = (1, 0, -1, 0)^T$ ,  $\mathbf{v}_3 = (1, -1, 1, -1)^T$ , and  $\mathbf{v}_4 = (0, 1, 0, -1)^T$ . Note that the last three of these vectors have components with different signs. Our computational results show that the competition instability threshold is set by the sign-fluctuating instability  $\mathbf{v}_3$ , which has a larger competition instability regime in the phase diagram of  $A$  versus  $r$  than does either  $\mathbf{v}_2$  or  $\mathbf{v}_4$ . There is no competition instability

threshold associated with  $\mathbf{v}_1$ . Similarly for  $k = 8$  and  $k = 16$ , the instability associated with the eigenvector of the form  $\mathbf{v} = (1, -1, 1, -1, \dots, 1, -1)^T$  is always the dominant competition mechanism. In contrast, as we discuss below, our numerical results show that the Hopf bifurcation threshold  $\tau_H$  for an oscillatory profile instability is set by the eigenvector  $\mathbf{v}_1$ , which corresponds to a synchronous oscillatory instability.

Since the sign-fluctuating eigenvector determines the competition instability threshold in Fig. 31 and Fig. 32, we get from (4.24) that, for  $k$  even, this threshold is obtained by numerically solving the simple coupled system

$$\chi'(S_c) + 2\pi \sum_{m=1}^k (-1)^{m-1} a_m = -\nu^{-1}, \quad A = \frac{\varepsilon}{\nu\sqrt{D}} [S_c(1 + 2\pi\nu\theta) + \nu\chi(S_c)], \quad \nu \equiv -\frac{1}{\ln \varepsilon}, \quad (6.9 a)$$

$$\theta = \sum_{m=1}^k a_m, \quad a_1 = R_{11}; \quad a_j = G_{1j}, \quad j = 2, \dots, k. \quad (6.9 b)$$

Here  $\theta$  is the eigenvalue of  $\mathcal{G}$  with eigenvector  $\mathbf{e} = (1, \dots, 1)^T$ . Numerical values for  $R_{11}$  and  $G_{1j}$ , for  $j = 2, \dots, k$ , are obtained from the reduced-wave Green's function for the unit disk given in (A.8) of Appendix A.

**Oscillatory and Competition Instabilities:** Next, we use our global eigenvalue problem to compute Hopf bifurcation thresholds  $\tau_H$  for an oscillatory instability of  $k$  equally-spaced spots on a ring. Such an instability is the only instability mechanism in each Regime  $\zeta$  of Fig. 32 and Fig. 31. Since this instability is not readily depicted in a phase diagram of the type shown in Fig. 32 and Fig. 31, we now discuss it some detail.

To focus the discussion, we will only consider an equally-spaced two-spot pattern on a ring of radius  $r$  in the unit disk. We show that both dynamically-triggered oscillatory and competition instabilities are possible for different ranges of the GS parameters, and we study the spectrum of the linearization in some detail.

For  $A = 0.26$ ,  $k = 2$ , and  $\varepsilon = 0.02$ , the Hopf bifurcation threshold  $\tau_H$  versus the ring radius  $r$ , corresponding to  $\mathbf{v}_1 = (1, 1)^T$ , is shown by the solid curves in Fig. 33. The dotted segments on these curves is where a competition instability occurs. In Fig. 33(a) we plot  $\tau_H(r)$  for  $D = 0.8, 1.0, 1.3, 1.5$ , while in Fig. 33(b) we plot  $\tau_H(r)$  for  $D = 2, 3, 4, 5$ . From the convexity of  $\tau_H$  versus  $r$  in Fig. 33(b), we conclude that a dynamically-triggered oscillatory profile instability can occur for a two-spot pattern when  $A = 0.26$  and  $D \geq 2$ . We also observe that when  $D = 5$ , a competition instability occurs when  $r \approx 0.568$ . Therefore, since the equilibrium ring radius is  $r_e \approx 0.455$  for  $D = 5$  (see Table 1), we conclude that there can be a dynamically-triggered competition instability for this value of  $D$ . To illustrate this, let  $D = 5$  and  $\tau = 1$  and suppose that we have an initial two-spot pattern with initial value  $r = 0.7$  at  $t = 0$ . Then, as the two spots move slowly towards each other, a dynamically-triggered competition instability will be initiated before the ring reaches its equilibrium radius at  $r_e \approx 0.455$ .

Next we fix  $A = 0.26$  and  $D = 3$ . In Fig. 34(a) we plot the Hopf bifurcation thresholds  $\tau_{H1}$  and  $\tau_{H2}$  for in-phase and out-of-phase spot amplitude oscillations, respectively. Since  $\tau_{H1} < \tau_{H2}$ , the oscillatory instability triggered as  $\tau$  increases is a synchronous spot amplitude oscillation. The dotted portion on  $\tau_{H1}$ , representing the continuation of the heavy solid curve in Fig. 34(a), shows where a competition instability occurs for any  $\tau \geq 0$ . In Fig. 34(b), we fix two spots on an equilibrium ring of radius  $r_e = 0.45483$ , and we plot the path of the complex conjugate pair of eigenvalues in the complex plane for the range  $\tau \in [3.7, 36]$ . We note that as  $\tau$  increases, the real parts of both pairs of eigenvalues increase. The eigenvalue for in-phase oscillations  $\mathbf{v}_1 = (1, 1)^T$ , which is given by the solid curve in Fig. 34(b), enters the right half-plane at  $\tau \approx 11.5$ . Note that the imaginary part of the eigenvalue for the out-of-phase oscillation  $\mathbf{v}_2 = (1, -1)^T$  becomes very close to the negative real axis when  $\tau < 3.7$ .

Next, for  $\varepsilon = 0.02$  and  $A = 0.26$ , we treat  $D$  as the bifurcation parameter and we relate our results with those

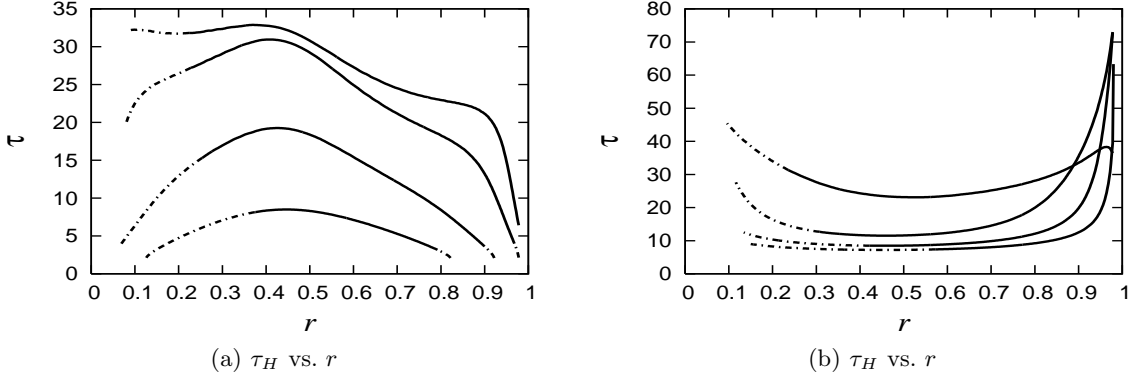


Figure 33. Two equally-spaced spots on a ring of radius  $r$  in the unit disk for  $\varepsilon = 0.02$ : (a) For  $A = 0.26$ , the Hopf bifurcation threshold  $\tau_H$  vs.  $r$  is plotted for  $D = 0.8, 1.0, 1.3, 1.5$ , with the lower curves corresponding to smaller values of  $D$ . The solid curves correspond to regions in  $r$  where an oscillatory profile instability occurs, and the dotted portions of these curves correspond to where a competition instability occurs for any  $\tau > 0$ . (b)  $\tau_H$  vs.  $r$  for the larger values of  $D$  given by  $D = 2, 3, 4, 5$ . The lower curves at  $r = 0.6$  correspond to larger values of  $D$ .

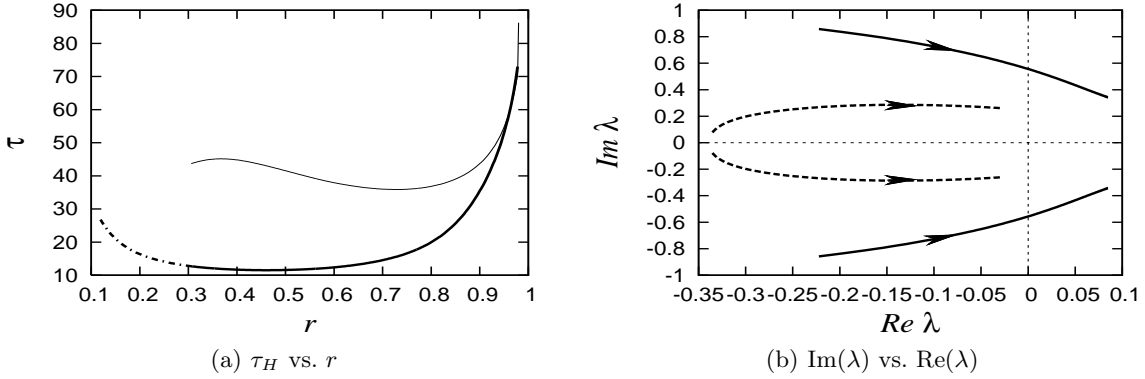


Figure 34. Two equally-spaced spots on a ring of radius  $r$  in the unit disk. Fix  $A = 0.26$ ,  $\varepsilon = 0.02$ , and  $D = 3$ . (a)  $\tau_H$  vs.  $r$  for in-phase spot amplitude oscillation  $\mathbf{v}_1 = (1, 1)^T$  (lower heavy solid curve), and  $\tau_{H2}$  for the out-of-phase oscillation  $\mathbf{v}_2 = (1, -1)^T$  (upper solid curve). The dotted portions on  $\tau_{H1}$  are where a competition instability occurs for any  $\tau \geq 0$ . (b) For the equilibrium ring radius  $r_e = 0.45483$ , we plot  $\lambda$  in the complex plane on the range  $\tau \in [3.7, 36]$ . The solid curve is for  $\mathbf{v}_1 = (1, 1)^T$ , while the dotted curve is for  $\mathbf{v}_2 = (1, -1)^T$ . As  $\tau$  increases (direction of the arrows),  $\text{Re}(\lambda)$  increases.

obtained from the NLEP theory of [62]. In Theorem 2.3 of [62], as summarized in Appendix B, the leading-order-in- $\nu$  NLEP analysis proves that if  $D = \mathcal{O}(\nu^{-1})$  and  $L_0 < \frac{\eta_0}{(2\eta_0+k)^2}$ , then the small solution  $u^-, v^-$  of (1.1) is stable for any  $\tau$  sufficiently small. In addition, the NLEP theory proves that if  $L_0 > \frac{\eta_0}{(2\eta_0+k)^2}$ , then this solution is unstable for any  $\tau > 0$ . From (B.7), we recall that  $L_0 = \lim_{\varepsilon \rightarrow 0} \frac{2\varepsilon^2 \pi b_0}{A^2 |\Omega|}$  and  $\eta_0 = \lim_{\varepsilon \rightarrow 0} \frac{|\Omega|}{2\pi D \nu}$ , where  $b_0 = \int_0^\infty w^2 \rho d\rho \approx 4.9347$  and  $w(\rho)$  satisfies (B.1). With  $|\Omega| = \pi$  and  $\nu = -1/\ln \varepsilon$ , and for the other GS parameter values as given, this stability bound is  $1.158 < D < 3.303$ . For this range of  $D$ , the leading-order-in- $\nu$  NLEP theory predicts that this solution is stable for  $\tau$  sufficiently small. Outside of this bound for  $D$ , the NLEP theory of [62] predicts that a competition instability occurs for any  $\tau > 0$ . This conclusion from NLEP theory is independent of the ring radius  $r$ .

For  $\varepsilon = 0.02$  and  $A = 0.26$ , in Fig. 35(a) we plot  $D_c$  versus  $r$  by the solid curve, where  $D_c$  denotes the critical value of  $D$  where a competition instability is initiated, as computed from (6.9). To the left of this curve, oriented

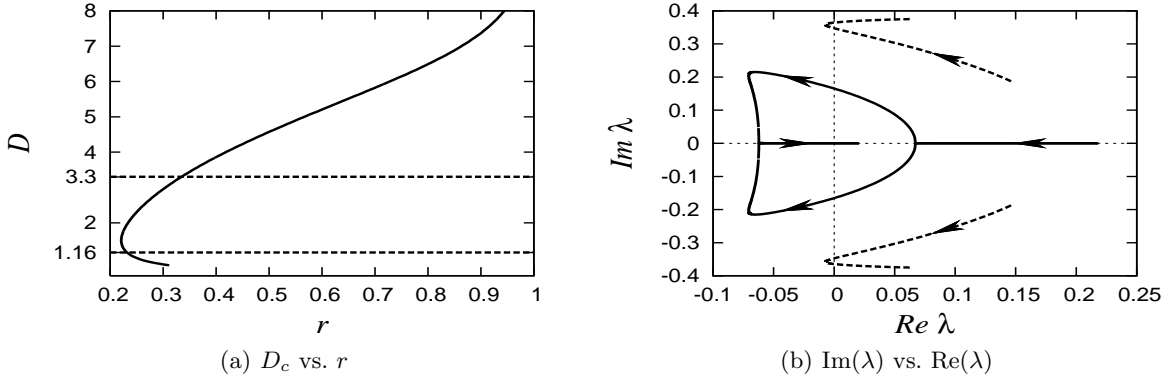


Figure 35. Two equally-spaced spots on a ring of radius  $r$  in the unit disk. Fix  $A = 0.26$  and  $\varepsilon = 0.02$ . (a) Plot of  $D_c$  vs.  $r$  (solid curve), where  $D_c$  is the critical value of  $D$  at which a competition instability is initiated. The region  $1.1583 < D < 3.3030$  between the two horizontal dotted lines is where the leading-order-in- $\nu$  NLEP theory predicts that no competition instability occurs. (b) For  $\tau = 30$  and  $r = 0.3$ , a plot of the spectrum in the complex plane is shown when  $D$  varies on the range  $[0.8, 3.1]$ , which corresponds to taking a vertical slice in Fig. 35(a) at  $r = 0.3$ . The solid path in the spectrum corresponds to  $\mathbf{v}_2 = (1, -1)^T$ , while the dotted path is for  $\mathbf{v}_1 = (1, 1)^T$ . The arrows show the path as  $D$  increases.

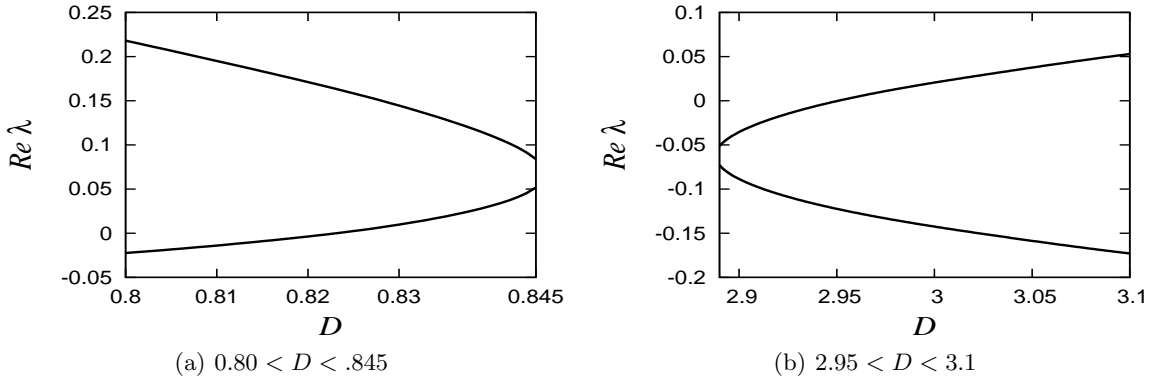


Figure 36. Two equally-spaced spots on a ring of radius  $r = 0.3$  in the unit disk. Fix  $A = 0.26$ ,  $\varepsilon = 0.02$ , and  $\tau = 30$ , and consider the sign-fluctuating eigenvector  $\mathbf{v}_2 = (1, -1)^T$ . We plot the eigenvalues of the global eigenvalue problem for two ranges of  $D$  where they are real. Left figure:  $D \in [0.8, 0.845]$ . Right figure:  $D \in [2.95, 3.10]$ .

with respect to the direction of increasing  $D$ , we predict that a competition instability occurs for any  $\tau > 0$ , while to the right of this curve we predict that the solution is stable when  $\tau$  is small enough. The two horizontal dotted lines with  $D_1 = 1.158$  and  $D_2 = 3.303$  in this figure bound a region of stability as predicted by the leading-order-in- $\nu$  NLEP theory of [62]. This prediction from NLEP theory does not capture the dependence of the stability threshold on the ring radius  $r$ . Our stability formulation, which accounts for all orders in  $\nu = -1/\ln \varepsilon$ , shows that  $D_c = D_c(r)$ . For  $\varepsilon = 0.02$ ,  $\nu$  is certainly not very small, and this dependence of the threshold on  $r$  is very significant.

In Fig. 35(b), for  $A = 0.26$ ,  $\tau = 30$ , and  $r = 0.3$ , we plot the spectrum in the complex plane as  $D$  varies over the range  $[0.8, 3.0]$ . This range of  $D$  corresponds to taking a vertical slice at  $r = 0.3$  in Fig. 35(a) that cuts across the stability boundary  $D_c(r)$  at two values of  $D$ . The arrows in Fig. 35(b) indicate the direction of the path of eigenvalues as  $D$  is increased from  $D = 0.8$ . The loop of spectra, depicted by the solid curves in Fig. 35(b), shows the eigenvalues associated with the eigenvector  $\mathbf{v}_2 = (1, -1)^T$ . From Fig. 35(a) we predict instability when  $D$  is near  $D = 0.8$  or

when  $D$  is near  $D = 3.0$ . This behavior is shown by the closed loop of spectra in the complex  $\lambda$  plane of Fig. 35(b), and in Fig. 36 where the eigenvalues are plotted for the range of  $D$  where they are real.

More specifically, with regards to the loop of spectra (solid curves) in Fig. 35(b) associated with the  $\mathbf{v}_2 = (1, -1)^T$  eigenvector, our results show that for  $D = 0.8$  there are two real eigenvalues at  $\lambda \approx 0.218$  and  $\lambda \approx -0.0224$  (the negative eigenvalue is not shown in Fig. 35(b)). From Fig. 36(a) we observe that as  $D$  is increased above  $D = 0.8$  the positive real eigenvalues move along the horizontal axis in different directions, and collide at  $D \approx 0.845$ , producing a complex conjugate pair of unstable eigenvalues at this value of  $D$ . Then, for  $D \approx 1.0$ , the complex conjugate pair of eigenvalues enters the stable left half-plane  $\text{Re}(\lambda) < 0$ . For  $D = 2.89$  the eigenvalues merge onto the negative real axis, as shown in Fig. 36(b). One eigenvalue then enters the right half-plane at  $D \approx 2.95$ , while the other slides along the negative real axis. Therefore, for  $D > 2.95$ , there is a positive real eigenvalue associated with the eigenvector  $\mathbf{v}_2 = (1, -1)^T$ , which generates a competition instability.

Alternatively, the dotted curves in Fig. 35(b) correspond to the path of eigenvalues associated with the  $\mathbf{v}_1 = (1, 1)^T$  eigenvector, representing synchronous oscillatory instabilities. This path depends sensitively on the value chosen for  $\tau$ . For  $\tau = 30$ , our computational results show that as  $D$  is increased above  $D = 0.8$ , the real part of these eigenvalues first starts to decrease and then crosses into the stable left half-plane  $\text{Re}(\lambda) < 0$  at  $D \approx 1.33$ . The real part of these eigenvalues starts increasing when  $D \approx 1.59$  and the path then re-enters the unstable right half-plane at  $D = 1.89$  where stability is lost at a Hopf bifurcation corresponding to synchronous oscillations of the two spot amplitudes. This path of eigenvalues remain in the unstable right half-plane  $\text{Re}(\lambda) > 0$  for  $D > 1.89$ .

For  $\tau = 30$ ,  $A = 0.26$ , and  $\varepsilon = 0.02$ , we conclude that if  $1.33 < D < 1.89$ , then the two-spot pattern is stable to both competition and synchronous oscillatory instabilities. When  $D > 2.95$  there is an unstable real eigenvalue in the right half-plane associated with a competition instability as well as a synchronous oscillatory instability associated with the complex conjugate pair of eigenvalues. On the range  $1.89 < D < 2.95$  there is only a synchronous oscillatory instability. We remark that if  $\tau$  is taken to be much smaller than our chosen value  $\tau = 30$ , then for  $D > 2.95$  there would be only a competition instability from a positive real eigenvalue, and no oscillatory instability would occur.

*Experiment 6.6: (One-ring pattern with two equally-spaced spots on a ring: Simultaneously occurring instabilities):*

For an equally-spaced two-spot pattern on a ring of radius  $r = 0.3$ , we now validate the theoretical prediction, based on Fig. 35, of having both a competition and oscillatory instability occurring simultaneously for the GS parameter values  $A = 0.26$ ,  $D = 3$ ,  $\tau = 30$ , and  $\varepsilon = 0.02$ . For these values, Fig. 35(b) shows that there is an unstable real eigenvalue together with an unstable complex conjugate pair of eigenvalues. In Fig. 37 we plot the maxima of  $v$  versus  $t$  of the two spots, as computed from a full numerical solution of (1.1). This figure shows that one of the two spots is annihilated before  $t = 13$ , consistent with a competition instability. In contrast, the amplitude of the other spot begins to oscillate, but the oscillation ceases after the first spot is annihilated. This occurs since after one spot has been destroyed, the value  $\tau = 30$  is below the Hopf bifurcation threshold for a one-spot solution in the unit disk.

## 7 Some Asymmetric Spot Patterns in the Unit Square and Disk

In this section we study spot self-replication instabilities for some spot patterns for which the Green's matrix is not circulant. The GS parameters are chosen so that competition and oscillatory instabilities do not occur. The asymptotic results for spot self-replication and spot dynamics are favorably compared with full numerical results.



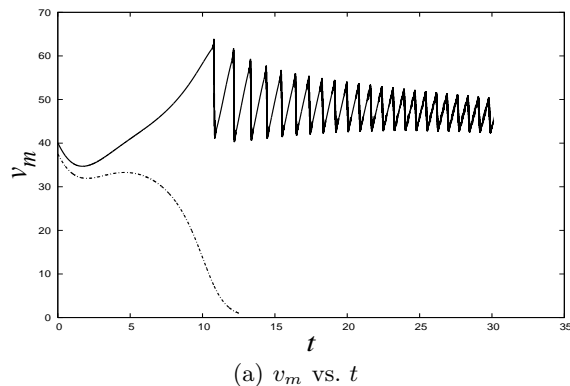


Figure 37. *Experiment 6.6: Two equally-spaced spots on a ring of radius  $r = 0.3$  in the unit disk. Fix  $\varepsilon = 0.02$ ,  $A = 0.26$ ,  $D = 3$ , and  $\tau = 30$ . The dot-dashed curve plots the amplitude  $v_{m1}$  vs.  $t$  of one the spots, while the solid curve shows the amplitude  $v_{m2}$  vs.  $t$  of the other spot. Both a competition and an oscillatory instability occur for the initial pattern.*

| $j$ | $x_j$ | $y_j$ | $S_j$ | $V_j(0)$ | $x_{jn}$ | $y_{jn}$ | $S_{jn}$ | $x_{je}$ | $y_{je}$ | $S_{je}$ |
|-----|-------|-------|-------|----------|----------|----------|----------|----------|----------|----------|
| 1   | 0.40  | 0.67  | 3.71  | 34.2     | 0.33     | 0.77     | 3.68     | 0.33     | 0.77     | 3.68     |
| 2   | 0.40  | 0.33  | 3.71  | 34.2     | 0.33     | 0.23     | 3.68     | 0.33     | 0.23     | 3.68     |
| 3   | 0.70  | 0.50  | 3.71  | 34.2     | 0.79     | 0.50     | 3.95     | 0.79     | 0.50     | 3.95     |

Table 2. *Experiment 7.1: The columns of  $x_j$ ,  $y_j$ ,  $S_j$  and  $V_j(0)$  correspond to the initial condition. The remaining data is with regards to the numerical and asymptotic results, respectively, for the equilibrium state.*

### 7.1 The Unit Square

We will consider three examples for the unit square  $[0, 1] \times [0, 1]$  for  $\varepsilon = 0.02$  and  $\tau = 1.0$ .

*Experiment 7.1: (A three-spot pattern: Slowly drifting spots):* Let  $\mathcal{A} = 20$  and  $D = 1$ , and consider an initial three-spot pattern with spots equally-spaced on a ring of radius  $r = 0.2$  centered at the midpoint of the unit square. The initial spot coordinates at  $t = 0$  are given in Table 2. For this pattern, the matrix  $\mathcal{G}$  in (2.10) is not circulant. However, by evaluating the entries of  $\mathcal{G}$  by using (A.11) of Appendix A, we compute that the three spots still have an initial common source strength  $S_c \approx 3.71$ . Since  $S_c < \Sigma_2$ , we predict that there is no spot self-replication initiated at  $t = 0$ . From the full numerical results shown in Fig. 38, we observe that all three spots drift slowly outwards, and approach equilibrium locations inside  $\Omega$  when  $t$  is large. During this evolution, the source strengths never exceed the threshold  $\Sigma_2$ , and so there is no dynamically-triggered spot self-replication instability.

In Fig. 39 we show a very favorable comparison between the spot trajectories, as obtained from the dynamics (3.7) of Principal Result 3.1, and the corresponding numerical results computed from (1.1). Since the initial locations of the 1<sup>st</sup> and 2<sup>nd</sup> spots are exactly symmetric, it follows that  $G_{1,3} = G_{2,3}$ ,  $R_{1,1} = R_{2,2}$ , and  $G_{1,2} = G_{2,1}$  in the Green's matrix  $\mathcal{G}$ . Thus, from Principal Result 3.1, these two spots move at the same speed and their trajectories in the  $x$ -direction exactly overlap, as shown in Fig. 39(a). Moreover, from the spot equilibrium condition (3.8), we can calculate the equilibrium locations  $x_{je}, y_{je}$ , and source strengths  $S_{je}$  for  $j = 1, \dots, 3$ . These values are given in Table 2, where we observe that our equilibrium result closely predicts the final equilibrium state  $x_{jn}, y_{jn}, S_{jn}$  computed from full numerical solutions of the GS model (1.1).

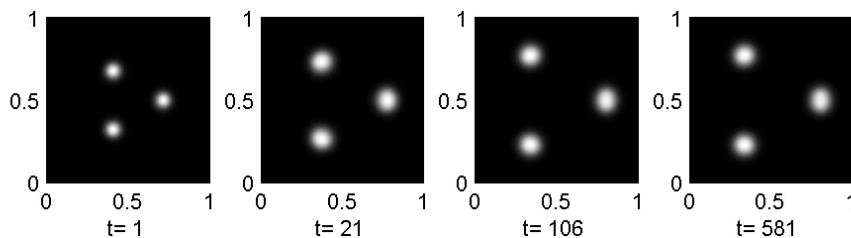


Figure 38. *Experiment 7.1: Fix  $\mathcal{A} = 20$ ,  $D = 1$ ,  $\tau = 1$ , and  $\varepsilon = 0.02$ . Consider a three-spot initial pattern with spots equally-spaced on a ring of radius  $r = 0.2$  centered at  $(0.5, 0.5)$  at time  $t = 0$  in the unit square. The initial common source strength is  $S_c \approx 3.71$  (see Table 2). The numerical solution  $v$  is shown at various times.*

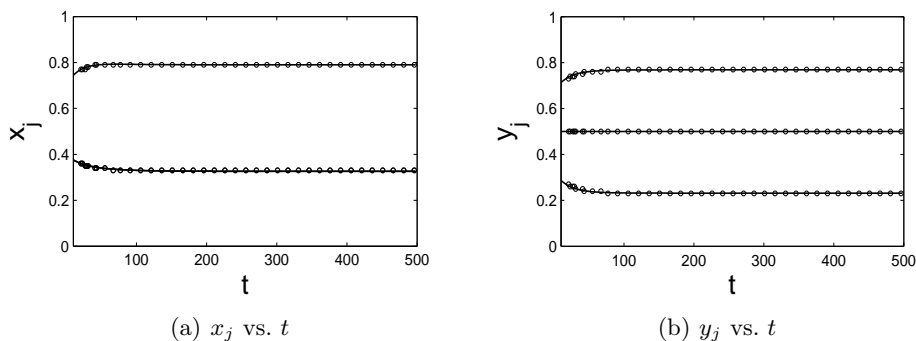


Figure 39. *Experiment 7.1: Fix  $\mathcal{A} = 20$ ,  $D = 1$ ,  $\tau = 1$ , and  $\varepsilon = 0.02$ . Comparison of the asymptotic dynamics of a 3-spot pattern (solid curves) with full numerical results (discrete markers) starting from  $t = 10$ . (a)  $x_j$  vs.  $t$ ; (b)  $y_j$  vs.  $t$ .*

Experiment 7.2: (*A three-spot pattern: Spot-splitting and dynamics after splitting*): Next, we fix  $\mathcal{A} = 20$  and  $D = 1$  and consider an initial three-spot pattern on a ring of radius  $r = 0.3$  centered at  $(0.4, 0.4)$  in the unit square. These GS parameter values are the same as in Experiment 7.1, except that here the initial spot configuration is different. The initial data are given in the left side of Table 3. Since  $S_3 > \Sigma_2$ , the asymptotic theory predicts that the 3<sup>rd</sup> spot will undergo splitting beginning at  $t = 0$ . In Fig. 40, we plot the numerical solution  $v$  at different instants in time. From this figure we observe that the 3<sup>rd</sup> spot (the brightest one at  $t = 1$ ) deforms into a peanut shape at  $t = 31$ , and then splits into two spots at  $t = 46$  in a direction perpendicular to its motion. Subsequently, the four spots drift slowly to a symmetric four-spot equilibrium state.

After the splitting event, we use the new 4-spot pattern  $x_{jt}, y_{jt}$  for  $j = 1, \dots, 4$  at  $t = 61$ , as given in Table 3, as the initial conditions for the asymptotic DAE system of Principal Result 3.1. At  $t = 61$ , the source strengths  $S_{1t}, \dots, S_{4t}$ , as given in Table 3, are all below the spot-splitting threshold. In Fig. 41, we show a very favorable comparison between the asymptotic trajectories of the spots for  $t \geq 61$  and the full numerical results computed from (1.1). Therefore, Principal Result 3.1 closely predicts the motion of a collection of spots after a spot self-replication event. We remark that in Fig. 41(a), the  $x$ -coordinates of the 1<sup>st</sup> and 2<sup>nd</sup> spots, as well as the 3<sup>rd</sup> and 4<sup>th</sup> spots, essentially overlap as a result of their almost symmetric locations.

From the spot equilibrium condition (3.8), we calculate the asymptotic result for the symmetric equilibrium locations  $x_{je}, y_{je}$  and source strengths  $S_{je}$ , for  $j = 1, \dots, 4$ . These results are given in Table 3, and compare almost exactly with the results from the full numerical simulations of the GS model (1.1) at  $t = 421$  (not shown).

| $j$ | $x_j$ | $y_j$ | $S_j$ | $V_j(0)$ | $x_{jt}$ | $y_{jt}$ | $S_{jt}$ | $x_{je}$ | $y_{je}$ | $S_{je}$ |
|-----|-------|-------|-------|----------|----------|----------|----------|----------|----------|----------|
| 1   | 0.25  | 0.66  | 4.05  | 32.54    | 0.30     | 0.75     | 3.44     | 0.25     | 0.75     | 2.87     |
| 2   | 0.25  | 0.14  | 2.37  | 35.48    | 0.28     | 0.20     | 3.01     | 0.25     | 0.25     | 2.87     |
| 3   | 0.70  | 0.40  | 4.79  | 27.65    | 0.76     | 0.36     | 2.40     | 0.75     | 0.25     | 2.87     |
| 4   | -     | -     | -     | -        | 0.77     | 0.59     | 2.55     | 0.75     | 0.75     | 2.87     |

Table 3. *Experiment 7.2: The columns of  $x_j$ ,  $y_j$ ,  $S_j$  and  $V_j(0)$  correspond to the initial condition. The data  $x_{jt}$ ,  $y_{jt}$ , and  $S_{jt}$  correspond to the initial conditions used for the asymptotic dynamics at  $t = 61$  after the spot-splitting event. The final columns are the equilibrium results for the 4-spot pattern obtained from the asymptotic theory.*

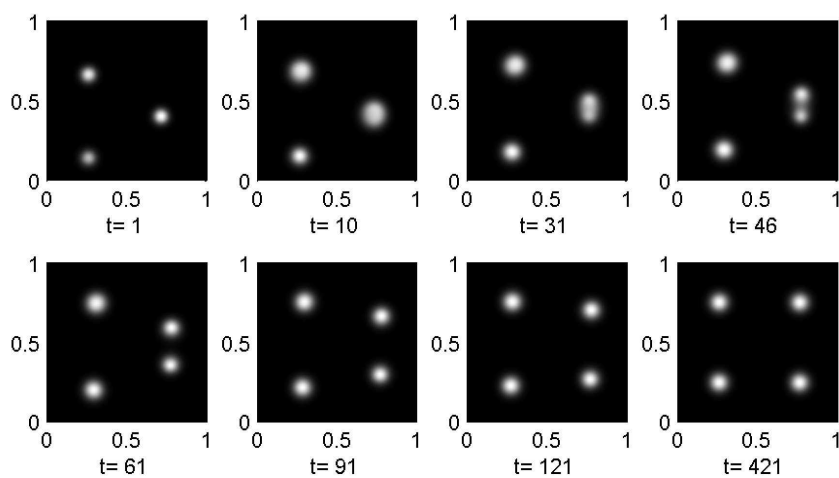


Figure 40. *Experiment 7.2: Fix  $A = 20$ ,  $D = 1$ ,  $\tau = 1$ , and  $\varepsilon = 0.02$ . Consider a three-spot initial pattern with spots equally-spaced on a ring of radius  $r = 0.3$  centered at  $(0.4, 0.4)$  in the unit square. The initial source strengths  $S_j$  for  $j = 1, \dots, 3$  are given in Table 3, for which  $S_3 > \Sigma_2$ . The full numerical solution for  $v$  is plotted at different instants in time. The 3<sup>rd</sup> spot undergoes self-replication. Subsequently, all four spots slowly drift towards a symmetric equilibrium 4-spot pattern.*

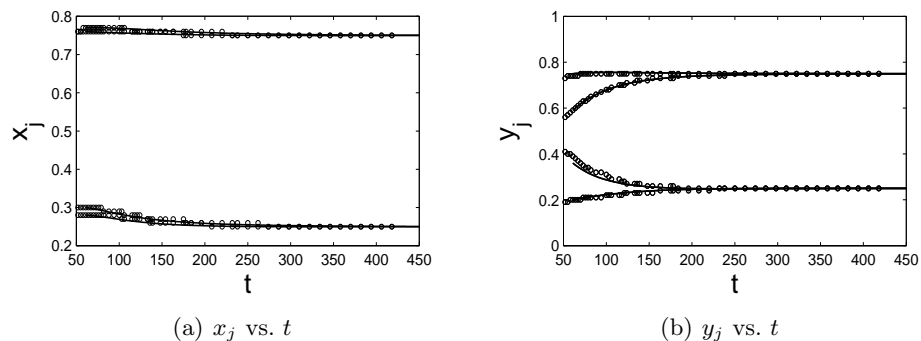


Figure 41. *Experiment 7.2: Fix  $A = 20$ ,  $D = 1$ ,  $\tau = 1$ , and  $\varepsilon = 0.02$ . Starting from  $t = 61$  after the spot-splitting event, and using the initial values as in Table 3, we compare the dynamics of the 4-spot pattern from the asymptotic analysis (solid curves) with the full numerical results (discrete markers). (a)  $x_j$  vs.  $t$ ; (b)  $y_j$  vs.  $t$ .*

| $j$ | $x_j$ | $y_j$ | $S_j$ | $V_j$ | $x_{jt}$ | $y_{jt}$ | $S_{jt}$ | $x_{je}$ | $y_{je}$ | $S_{je}$ |
|-----|-------|-------|-------|-------|----------|----------|----------|----------|----------|----------|
| 1   | 0.80  | 0.60  | 2.82  | 36.21 | 0.84     | 0.58     | 3.13     | 0.83     | 0.61     | 2.91     |
| 2   | 0.60  | 0.80  | 2.82  | 36.21 | 0.58     | 0.84     | 3.13     | 0.61     | 0.83     | 2.91     |
| 3   | 0.40  | 0.60  | 5.69  | 19.07 | 0.25     | 0.49     | 2.93     | 0.17     | 0.39     | 2.91     |
| 4   | 0.60  | 0.40  | 5.69  | 19.07 | 0.26     | 0.66     | 2.73     | 0.21     | 0.79     | 3.07     |
| 5   | -     | -     | -     | -     | 0.49     | 0.25     | 2.93     | 0.39     | 0.17     | 2.91     |
| 6   | -     | -     | -     | -     | 0.66     | 0.26     | 2.73     | 0.79     | 0.21     | 3.07     |

Table 4. *Experiment 7.3: The columns of  $x_j$ ,  $y_j$ ,  $S_j$  and  $V_j(0)$  correspond to the initial condition. The data  $x_{jt}$ ,  $y_{jt}$ , and  $S_{jt}$  correspond to the initial conditions used for the asymptotic dynamics at  $t = 21$  after the two spot-splitting events. The final columns are the equilibrium results for the 6-spot pattern.*

*Experiment 7.3: (An asymmetric four-spot pattern):* We fix  $\mathcal{A} = 30$  and  $D = 1$ , and consider an initial 4-spot pattern with equally-spaced spots on a ring of radius 0.2 centered at  $(0.6, 0.6)$  in the unit square. The initial spot locations and source strengths are given on the left side of Table 4. For this case, we find that  $S_3 > \Sigma_2$  and  $S_4 > \Sigma_2$ , so that our asymptotic theory predicts that these two specific spots undergo self-replication events starting at  $t = 0$ . The full numerical results for this pattern are given in Fig. 42, where we observe that the 3<sup>rd</sup> and 4<sup>th</sup> spots split in a direction perpendicular to their motion. The resulting 6-spot pattern, with initial locations  $x_{jt}$ ,  $y_{jt}$  for  $j = 1, \dots, 6$  at  $t = 21$ , as given in Table 4, are used as initial conditions for the asymptotic DAE system in Principal Result 3.1. These six spots evolve outwards as  $t$  increases and eventually approach their equilibrium states  $x_{je}$ ,  $y_{je}$ , and  $S_{je}$ , for  $j = 1, \dots, 6$ , as given in Table 4, when  $t = 581$ . The asymptotic result obtained from the spot equilibrium condition (3.8) for the 6-spot equilibrium state is found to compare very favorably with the full numerical results at  $t = 581$ .

A very favorable comparison of analytical (solid curves) and full numerical results (discrete markers) for the spot trajectories after  $t = 21$  is shown in Fig. 43. This agreement further validates our spot equilibrium condition (3.8).

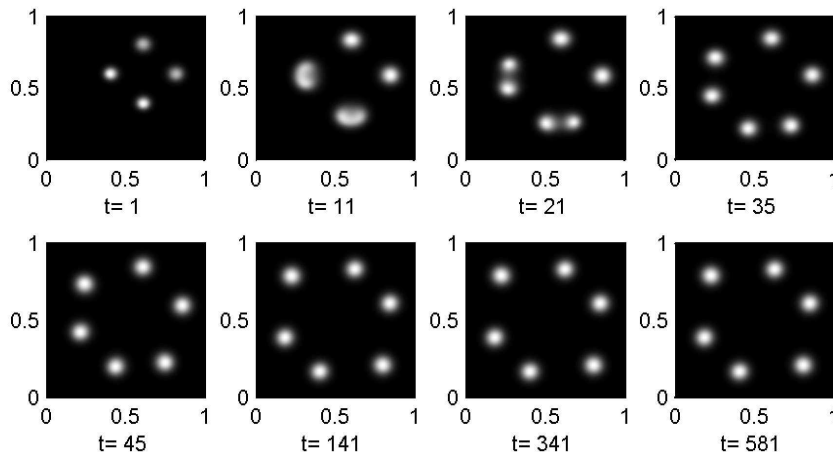


Figure 42. *Experiment 7.3: Fix  $\mathcal{A} = 30$ ,  $D = 1$ ,  $\tau = 1$ , and  $\varepsilon = 0.02$ . Consider a four-spot initial pattern with spots equally spaced on a ring of radius  $r = 0.2$  centered at  $(0.6, 0.6)$  in the unit square. The initial source strengths  $S_j$  for  $j = 1, \dots, 4$  are given in Table 4, for which  $S_3 > \Sigma_2$  and  $S_4 > \Sigma_2$ . The full numerical solution for  $v$  is shown at different instants in time. The 3<sup>rd</sup> and 4<sup>th</sup> spots undergo self-replication. Subsequently, all six spots move towards a symmetric 6-spot equilibrium pattern.*

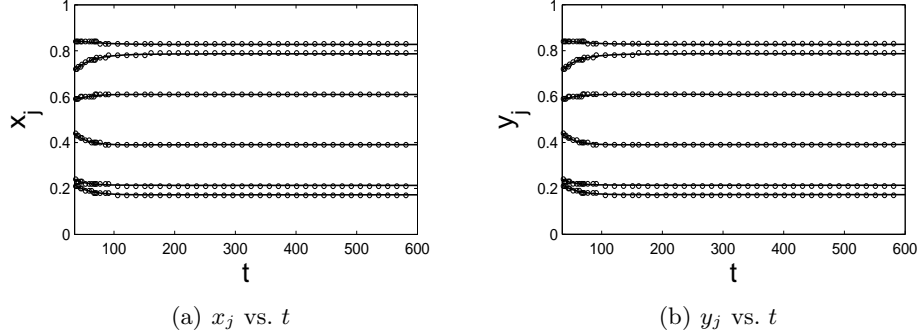


Figure 43. *Experiment 7.3: Fix  $\mathcal{A} = 30$ ,  $D = 1$ ,  $\tau = 1$ , and  $\varepsilon = 0.02$ . For  $t \geq 21$ , after the two spot-splitting events, we compare the asymptotic dynamics of the 6 spots (solid curves) with full numerical results (discrete markers). (a)  $x_j$  vs.  $t$ ; (b)  $y_j$  vs.  $t$ .*

## 7.2 The Unit Disk: A Ring Pattern of Spots with a Center Spot

In this subsection, we let  $\varepsilon = 0.02$  and  $\tau = 1$ , and we construct a spot pattern for which  $k - 1$  spots are equally spaced on a ring of radius  $r$ , with  $0 < r < 1$ , and with an additional spot located at the center of the unit disk. The  $k - 1$  spots on the ring have a common source strength  $S_c$ , while the  $k^{\text{th}}$  spot at the origin has a source strength denoted by  $S_k$ . For this pattern, the centers of the spots, written as complex numbers inside the unit disk, are at

$$\mathbf{x}_j = r e^{2\pi i j / (k-1)}, \quad j = 1, \dots, k-1; \quad \mathbf{x}_k = 0, \quad k \geq 3.$$

We will analyze the dynamics of the spots and the possibility of spot-splitting for this pattern for the limiting case  $D \gg 1$ , for which the Green's function  $G$  can be approximated by the Neumann Green's function  $G^{(N)}$ . Recall, that  $G^{(N)}$  has a very simple analytical formula in the unit disk (see Appendix A.2). As a result, the dynamics of the spots and the conditions for spot self-replication can be obtained in a very explicit form.

For this pattern, Principal Result 3.1 shows that the  $k^{\text{th}}$  spot at the center of the disk is stationary. In addition, by differentiating (6.6), it readily follows that the dynamics of the remaining  $k - 1$  spots on the ring satisfy

$$\mathbf{x}'_j \sim -2\pi\varepsilon^2\gamma(S_c) \left[ \left( \frac{S_c}{2} \right) \frac{p'_{k-1}(r)}{k-1} e^{2\pi i j / (k-1)} + S_k G_r(r; 0) e^{2\pi i j / (k-1)} \right], \quad j = 1, \dots, k-1. \quad (7.1)$$

Here  $G(r; 0)$  is the radially symmetric reduced-wave Green's function with singularity at the origin, and  $p_{k-1}(r)$  is defined in (6.6), with limiting asymptotics for  $D \gg 1$  also given in (6.6). Since  $\mathbf{x}_j = r e^{2\pi i j / (k-1)}$  for  $j = 1, \dots, k-1$ , then (7.1) reduces to an ODE for the ring radius given by

$$\frac{dr}{dt} \sim -2\pi\varepsilon^2\gamma(S_c) \left[ \left( \frac{S_c}{2} \right) \frac{p'_{k-1}(r)}{k-1} + S_k G_r(r; 0) \right], \quad (7.2 a)$$

in terms of  $S_c = S_c(r)$  and  $S_k = S_k(r)$ . From (2.7), we obtain that  $S_c = S_c(r)$  and  $S_k = S_k(r)$  are the solutions to the coupled two-component nonlinear algebraic system

$$\mathcal{A} = S_c \left( 1 + \frac{2\pi\nu}{k-1} p_{k-1}(r) \right) + \nu\chi(S_c) + 2\pi\nu G(r; 0) S_k, \quad \mathcal{A} = 2\pi\nu(k-1)G(r; 0)S_c + \nu\chi(S_k) + S_k (1 + 2\pi\nu R_{0,0}), \quad (7.2 b)$$

where  $R_{0,0}$  is the regular part of  $G(r; 0)$  at the origin. The problem (7.2) is a DAE system for the ring radius, consisting of the ODE (7.2 a) coupled to the two nonlinear constraints (7.2 b). The core problem for an individual spot enters only through the determination of  $\chi(S)$  and  $\gamma(S)$ .

Since  $p_{k-1}(r)$  is only known explicitly when  $D \gg 1$ , we use the large  $D$  asymptotics (6.6), together with

$$G(r; 0) \sim D + G^{(N)}(r; 0) = D - \frac{1}{2\pi} \ln r + \frac{r^2}{4\pi} - \frac{3}{8\pi}, \quad R_{0,0} \sim D + R_{0,0}^{(N)} = D - \frac{3}{8\pi}, \quad D \gg 1, \quad (7.3)$$

to calculate the equilibrium ring radius. By setting  $r' = 0$  in (7.2 a), we obtain the following transcendental equation for the equilibrium ring radius  $r_e$  when  $D \gg 1$ :

$$\frac{S_k}{S_c} (1 - r^2) + \frac{(k-2)}{2} - r^2(k-1) - (k-1) \frac{r^{2k-2}}{1 - r^{2k-2}} = 0. \quad (7.4)$$

By solving the three nonlinear algebraic equations in (7.2 b) and (7.4) we obtain equilibrium values  $r_e$ ,  $S_{ce}$ , and  $S_{ke}$ .

In Fig. 44(a) and Fig. 44(b), we fix  $D = 3.912$  and we plot the numerically computed source strengths  $S_c$  and  $S_k$ , respectively, versus the ring radius  $r$  for  $k = 3, \mathcal{A} = 22$ , and for  $k = 4, \mathcal{A} = 38$ , as computed from (7.2 b). In this computation we used the large  $D$  asymptotics of (6.6) and (7.3) in (7.2 b). In Fig. 44(a) the upper (lower) branch of the  $S_c = S_c(r)$  curve corresponds to the lower (upper) branch of the  $S_k = S_k(r)$  curve shown in Fig. 44(b). For each pattern, there are two equilibrium ring radii, which are marked by the solid dots. The spot-splitting threshold  $\Sigma_2$  is also marked on the curves in Fig. 44(a) and Fig. 44(b) by the open dots. We now show how these figures can be readily used to predict spot-splitting behavior.

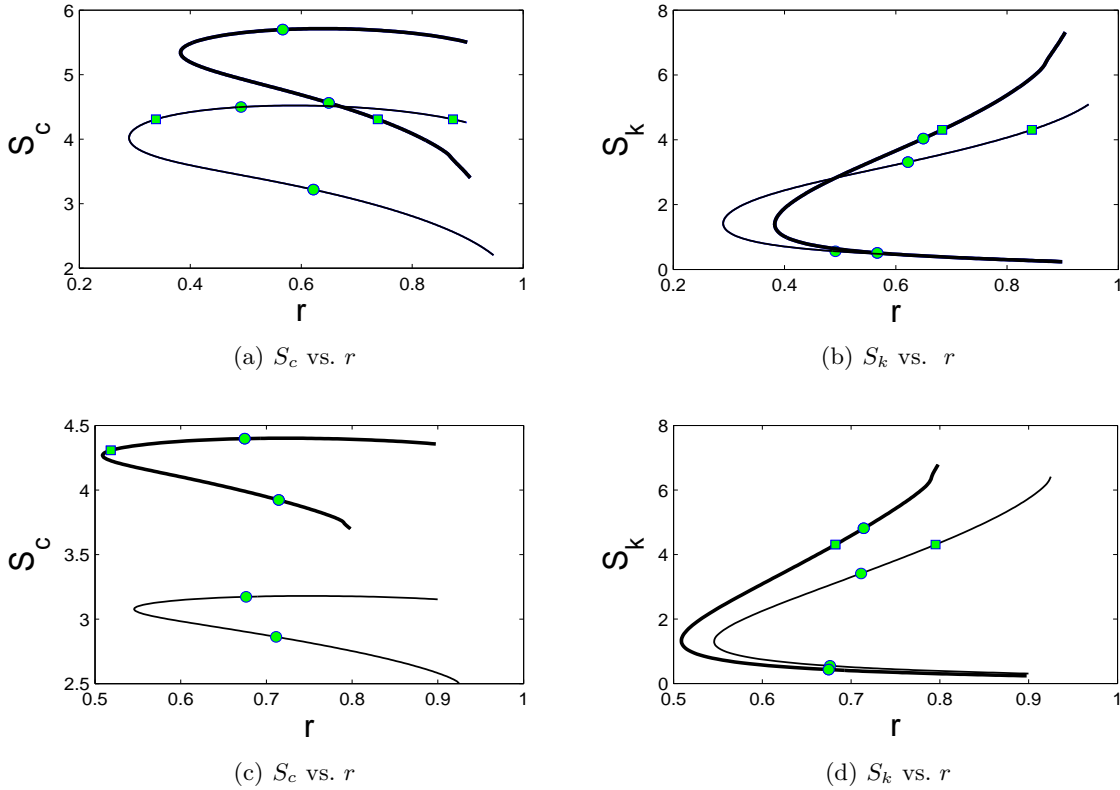


Figure 44. Fix  $D = 3.912$ ,  $\varepsilon = 0.02$ . (a) The solid curves correspond to  $\mathcal{A} = 22, k = 3$  and the heavy solid curves correspond to  $\mathcal{A} = 38, k = 4$ . The open dots correspond to spot-splitting thresholds, and the solid dots correspond to equilibrium ring radii. (b) The heavy solid curves correspond to  $\mathcal{A} = 82, k = 10$  and the solid curves correspond to  $\mathcal{A} = 60, k = 10$ . Left:  $S_c$  vs.  $r$ ; Right:  $S_k$  vs.  $r$ . Each upper (lower) branch for  $S_c(r)$  corresponds to the lower (upper) branch for  $S_k(r)$ .

*Experiment 7.4: (A one-ring pattern with a center-spot for  $D \gg \mathcal{O}(1)$ : Different types of spot-splitting):* We fix  $\mathcal{A} = 38$  and  $D = 3.912$  and consider an initial pattern of one center-spot and three equally-spaced spots on a ring of initial radius  $r = 0.8$  at time  $t = 0$ . We then predict the dynamical behavior of this initial spot pattern from the heavy solid curves in Fig. 44(a) and Fig. 44(b). From the data used to plot Fig. 44(b), we obtain from the upper branch of the  $S_k$  versus  $r$  curve that  $S_k = 5.38 > \Sigma_2$  at time  $t = 0$ . Correspondingly, from the lower branch of the  $S_c$  versus  $r$  curve in Fig. 44(a), we obtain that  $S_c < \Sigma_2$  at  $t = 0$ . Therefore, we predict that the center-spot will undergo spot-splitting starting at  $t = 0$ . The other three spots remain on a ring whose radius decreases slowly in time. For this parameter set, the full numerical results computed from the GS model (1.1), shown in the top row of Fig. 45, confirm the prediction based on the asymptotic theory.

In contrast, suppose that the initial ring radius is decreased from  $r = 0.8$  to  $r = 0.5$ . Then, from the heavy solid curve in Fig. 44(a), we now calculate that  $S_c \approx 4.92 > \Sigma_2$  from the lower branch of the  $S_c$  versus  $r$  curve. Correspondingly, from the upper branch of the  $S_k$  versus  $r$  curve in Fig. 44(b) we get  $S_k < \Sigma_2$  at  $t = 0$ . Thus, for this initial ring radius, we predict that the three spots on the ring undergo simultaneous spot-splitting starting at  $t = 0$ , while the center-spot does not split. The full numerical results shown in the second row of Fig. 45, as computed from the GS model (1.1), fully support this prediction based on the asymptotic theory.

We remark that based on the relative locations of the equilibrium ring radius and the spot-splitting threshold in Fig. 44(a) and Fig. 44(b), we conclude that it is not possible to obtain a dynamically-triggered spot-self replication instability for these parameter values. This more exotic instability is shown in our final example.

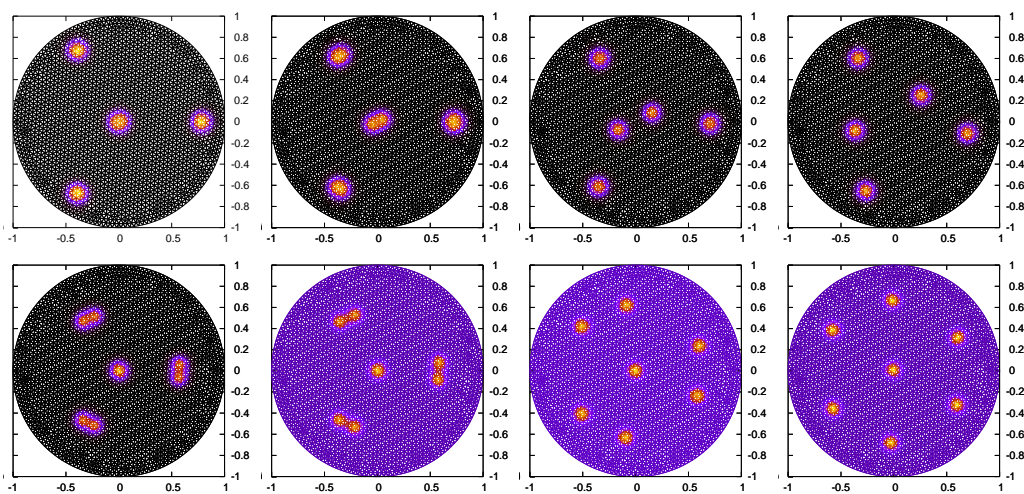


Figure 45. *Experiment 7.4: Fix  $\mathcal{A} = 38$ ,  $D = 3.912$ , and  $\varepsilon = 0.02$ . The numerical results for  $v$  computed from the GS model (1.1) at different instants in time are shown. The initial condition has three equally-spaced spots on a ring together with a center-spot. Top row: initial ring radius  $r = 0.8$ : Plots of  $v$  from left to right at times  $t = 4.6, 46, 102, 298$ . Bottom row: initial ring radius  $r = 0.5$ : Plots of  $v$  from left to right at times  $t = 4.6, 56, 140, 298$ .*

*Experiment 7.5: (A one-ring pattern with a center-spot for  $D \gg \mathcal{O}(1)$ : A dynamically-triggered instability):* In Fig. 44(c) and Fig. 44(d), we fix  $k = 10$  and  $D = 3.912$  and plot  $S_c$  and  $S_k$  versus  $r$  for  $\mathcal{A} = 82$  and  $\mathcal{A} = 60$ . In

these figures, each solid dot and empty circle denotes an equilibrium ring radius and the spot-splitting threshold, respectively.

Consider first the solid curve in Fig. 44(c) and Fig. 44(d) corresponding to  $\mathcal{A} = 60$ . For this value of  $\mathcal{A}$  it follows that only the center-spot can split and the minimum ring radius that leads to this spot-splitting is  $r = 0.80$ . Based on the relative locations of the equilibrium state and the spot-splitting threshold on the solid curve for  $S_k = S_k(r)$  in Fig. 44(d), we conclude that a dynamically-triggered spot self-replication instability is not possible.

Next, suppose that  $\mathcal{A}$  is increased to  $\mathcal{A} = 82$ , and consider an initial ring radius of  $r = 0.62$  at time  $t = 0$ . Then, from the heavy solid curve in Fig. 44(c) we calculate the initial source strengths as  $S_c \approx 4.03$  on the lower branch of the  $S_c$  versus  $r$  curve, and correspondingly  $S_k = 3.38$  at  $t = 0$  on the upper branch of the  $S_k$  versus  $r$  curve in Fig. 44(d). Therefore, we predict that the initial pattern is stable to spot-splitting. However, for  $t > 0$ , we predict from Fig. 44(d) that the center-spot will eventually split at the ring radius  $r = 0.68$  when  $S_k$  crosses above  $\Sigma_2$ . This occurs at a time before the ring radius has approached its equilibrium state at  $r_{e1} = 0.71$ . Therefore, our asymptotic theory predicts that a dynamical-triggered spot-splitting instability will occur for this parameter set. This behavior is confirmed by the full numerical results shown in Fig. 46 computed from the GS model (1.1).

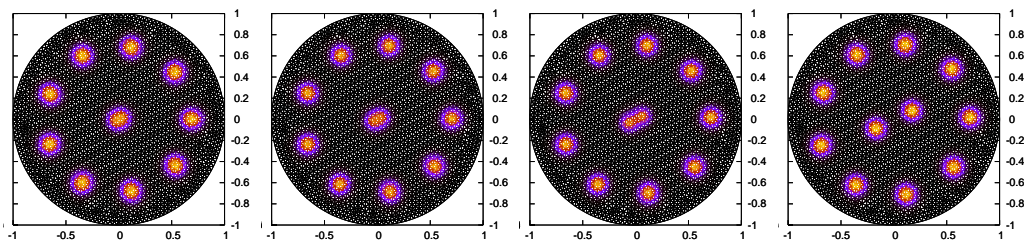


Figure 46. *Experiment 7.5: Fix  $\mathcal{A} = 82$ ,  $D = 3.912$ , and  $\varepsilon = 0.02$ . The full numerical results computed from the GS model (1.1) are shown at different instants in time. The initial pattern has nine spots equally spaced on a ring of initial radius  $r = 0.62$  together with a center-spot. From left to right the plots of  $v$  are shown at times  $t = 60, 93, 144, 214$ .*

## 8 Discussion

For the GS model (1.1) in a two-dimensional domain in the semi-strong interaction regime  $D = \mathcal{O}(1)$ , and for  $A = \mathcal{O}(-\varepsilon \ln \varepsilon)$ , the slow dynamics and instability mechanisms of quasi-equilibrium multi-spot patterns was studied by a hybrid asymptotic-numerical method. By using a singular perturbation approach that accounts for all terms in powers of  $\nu = -1/\ln \varepsilon$ , a multi-spot quasi-equilibrium pattern was constructed by asymptotically matching a local approximation of the solution near each spot to a global representation of the solution defined in terms of the reduced-wave Green's function. The local problem near each spot, referred to as the core problem, consisted of a radially-symmetric BVP system that must be solved numerically. In the global, or outer, representation of the solution, each spot at a given instant in time is asymptotically approximated as a Coulomb singularity for  $u$  of strength  $S_j$  at location  $\mathbf{x}_j \in \Omega$  for  $j = 1, \dots, k$ . In Principal Result 3.1 a DAE system was derived for the slow time evolution of the coordinates  $\mathbf{x}_j$  and  $S_j$  for  $j = 1, \dots, k$ , which characterizes the slow dynamics of the  $k$ -spot quasi-equilibrium pattern. The method used to construct quasi-equilibria is an extension of that developed in [57] (see also [32], [13], [49]) to sum logarithmic asymptotic expansions for linear PDE models in perforated 2-D domains.

The stability of the multi-spot quasi-equilibrium solution to three distinct types of  $\mathcal{O}(1)$  time-scale instabilities was studied. From a numerical study of a local eigenvalue problem near each spot, an explicit criterion for the initiation



of a peanut-splitting instability was obtained, and it was verified numerically that this instability triggers a nonlinear spot self-replication event. In addition, a singular perturbation method was used to formulate a global eigenvalue problem characterizing the onset of either oscillatory or competition instabilities for the multi-spot pattern. This global eigenvalue problem was studied for special multi-spot patterns for which a certain Green's matrix is circulant.

Our hybrid asymptotic-numerical framework for spot dynamics and stability was implemented numerically for some spot patterns in  $\mathbb{R}^2$  and in the unit disk and square. The results from our theory were shown to very compare favorably with those obtained from full numerical simulations of the GS model (1.1). One key finding is that dynamically-triggered instabilities can occur for the GS model in a wide parameter range. The qualitative differences in multi-spot solution behavior between the GS model (1.1) and the Schnakenburg model of [38] were highlighted.

The numerics required to implement the hybrid asymptotic-numerical theory is rather simple, provided that the reduced-wave Green's function for the domain can be readily determined. For the domains considered in this paper, this Green's function is available analytically, whereas for other domains it can be computed rapidly by using fast multipole methods for linear PDE's (cf. [12]). When this Green's function is available, the implementation of the hybrid asymptotic-numerical approach only requires the numerical solution of a coupled DAE system for the spot dynamics and a BVP to compute competition and oscillatory instability thresholds. The DAE system for  $\mathbf{x}_j$  and  $S_j$  involves two functions (i.e.  $\chi(S_j)$  and  $\gamma(S_j)$ ) that are determined in terms of the solution to the core problem. These functions are readily pre-computed by solving some simple BVP's. Similarly, from a BVP eigenvalue problem, the condition for the onset of self-replication is readily pre-computed in terms of a threshold value of the source strength  $S_j$ .

In this way, a similar hybrid approach should be readily applicable to study spot dynamics and spot stability for related two-component RD models of the general form

$$v_t = \varepsilon^2 \Delta v - v + f(u)v^p, \quad \tau u_t = D \Delta u - (u - u_0) + \varepsilon^{-2} g(u)v^m, \quad \mathbf{x} \in \Omega, \quad (8.1 a)$$

for  $p > 0$ ,  $m > 0$ , and for certain classes of  $f(u)$  and  $g(u)$ . The key conditions that are needed for our approach are that there is a core problem near each spot for which  $v \rightarrow 0$  and  $u$  has a logarithmic growth at infinity in terms of the stretched inner variable, and that the spots are coupled together via a quasi-static linear elliptic concentration field for  $u$ . Such a generalization of our overall approach for the GS model is undertaken in [10] for the simple case of a two-spot evolution in  $\mathbb{R}^2$ . The work in [10] is the two-dimensional counterpart of the study of [19] of two-spike solutions for a general class of RD systems on the infinite line.

We conclude this paper by discussing a few open problems for the GS model related to spot dynamics, equilibria, and stability. The first main problem is to develop a weakly nonlinear stability theory for the three different types of instabilities. Our numerical results suggest that both the peanut-splitting instability and the oscillatory instability are subcritical, as they lead to spot self-replication and spot-annihilation, respectively. In particular, with regards to self-replication, it would be interesting to perform a weakly nonlinear analysis of the time-dependent core problem (4.6) to show that the initial peanut-splitting instability does not saturate in the weakly nonlinear regime, but instead triggers a nonlinear spot self-replication event.

For the equilibrium problem, a main open problem is to use the spot equilibrium condition (3.8) to calculate detailed bifurcation diagrams in terms of  $A$  and  $D$  of steady-state  $k$ -spot patterns in arbitrary domains. One goal would be to determine whether asymmetric equilibria, characterized by equilibrium spot patterns with different source strengths, are possible and to then determine the multiplicity of equilibrium solutions. For these asymmetric

multi-spot equilibria, it should be possible to calculate oscillatory and competition instability thresholds from our global eigenvalue problem. The analysis in this paper has largely been restricted to the case where the Green's matrix is circulant, which allows for spot patterns with a common source strength.

Another open problem is to study weak translational instabilities associated with multi-spot equilibrium patterns. Such small eigenvalue instabilities, with growth rate  $\lambda = \mathcal{O}(\varepsilon^2)$ , are characterized by instabilities of stationary points of the DAE system of Principal Result 3.1 governing spot dynamics. Based on the numerical results in Fig. 15 of [38], one simple scenario where such a weak instability occurs is for a one-ring pattern of spots inside a disk. More specifically, we expect that an equilibrium pattern consisting of  $k$  equally-spaced spots on a ring concentric within the unit disk will be weakly unstable with growth rate  $\lambda = \mathcal{O}(\varepsilon^2)$  when  $k$  exceeds some threshold. Similar thresholds for weak instabilities have been studied in [27] for a ring of spots in the context of a simple interacting particle system model, and in [7] and [8] for a ring of Eulerian fluid point vortices on the surface of a sphere.

Finally, it would be very interesting to exhibit a parameter regime for the GS model where the quasi-equilibrium spot pattern undergoes repeated episodes of either spot self-replication, when a spot is too far from any of its neighbors, or spot-oscillation leading to annihilation, which is triggered when two slowly-drifting spots become too closely spaced. For  $D$  small, but with  $D \gg \mathcal{O}(\varepsilon^2)$ , such a replication-annihilation ‘‘attractor’’ should be realizable by considering the instability thresholds for two-spot interactions in  $\mathbb{R}^2$ . In this paper, a key first step in the construction of this ‘‘attractor’’ has been undertaken by showing that the GS model can robustly support the existence of dynamically-triggered instabilities for a collection of spots that are initially stable at  $t = 0$ .

### Acknowledgments

M. J. W. was supported by NSERC (Canada). We are grateful to Prof. P. Zegeling for the use of his code VLUGR2 to calculate full numerical solutions of the GS model. MJW is grateful to Prof. J. Wei for helpful comments. We are grateful to the referees for their very helpful comments.

## Appendix A The Reduced-Wave and Neumann Green's Function

In this appendix we give detailed analytical results for both the reduced-wave Green's function and the Neumann Green's function for the unit disk and for a rectangle. These results are needed in §6 and §7 in order to numerically implement the analytical theory of §2–4 for spot dynamics and instabilities.

### A.1 Green's Function for a Unit Disk

Let  $\Omega = \{\mathbf{x} : |\mathbf{x}| \leq 1\}$ . Upon introducing polar coordinates  $(x_0, y_0) = (\rho_0 \cos \theta_0, \rho_0 \sin \theta_0)$ , the reduced-wave Green's function of (1.2) satisfies

$$G_{\rho\rho} + \frac{1}{\rho}G_{\rho} + \frac{1}{\rho^2}G_{\theta\theta} - \frac{1}{D}G = -\frac{1}{\rho}\delta(\rho - \rho_0)\delta(\theta - \theta_0), \quad 0 < \rho < 1, \quad 0 \leq \theta < 2\pi, \quad (\text{A.1})$$

with boundary conditions  $G(\rho, \theta + 2\pi) = G(\rho, \theta)$ ,  $G_{\rho}(1, \theta) = 0$ , and where  $G$  is well-behaved as  $\rho \rightarrow 0$ .

To determine  $G$ , we first extract the  $\theta$  dependence by introducing the complex Fourier series

$$G(\rho, \theta; \rho_0, \theta_0) = \frac{1}{2\pi} \sum_{n=-\infty}^{\infty} \tilde{G}_n(\rho; \rho_0, \theta_0) e^{-in\theta}, \quad \tilde{G}_n(\rho; \rho_0, \theta_0) = \int_0^{2\pi} e^{in\theta} G(\rho, \theta; \rho_0, \theta_0) d\theta. \quad (\text{A.2})$$

From (A.1) we obtain that  $\tilde{G}_{n\rho\rho} + \rho^{-1}\tilde{G}_{n\rho} - n^2\rho^{-2}\tilde{G}_n - D^{-1}\tilde{G}_n = -\rho^{-1}\delta(\rho - \rho_0)e^{in\theta_0}$  on  $0 < \rho < 1$ , with boundary conditions  $\tilde{G}_{n\rho}(1; \rho_0, \theta_0) = 0$  and  $\tilde{G}_n(0; \rho_0, \theta_0) < \infty$ . The solution to this problem has the form

$$\tilde{G}_n(\rho; \rho_0, \theta_0) = \begin{cases} A_1 I_n\left(\frac{\rho}{\sqrt{D}}\right), & 0 < \rho < \rho_0, \\ A_2 \left[ I_n\left(\frac{\rho}{\sqrt{D}}\right) - \frac{I'_n\left(\frac{1}{\sqrt{D}}\right)}{K'_n\left(\frac{1}{\sqrt{D}}\right)} K_n\left(\frac{\rho}{\sqrt{D}}\right) \right], & \rho_0 < \rho < 1, \end{cases} \quad (\text{A.3})$$

where  $I_n(r)$  and  $K_n(r)$  are modified Bessel functions of order  $n$ . In (A.3), the coefficients  $A_1$  and  $A_2$  are obtained by making  $\tilde{G}_n$  continuous at  $\rho_0$  and by requiring that the jump in the derivative of  $\tilde{G}_n$  at  $\rho_0$  is  $[\tilde{G}_{n\rho}]_{\rho_0} = -\frac{e^{in\theta_0}}{\rho_0}$ . Then, upon using the Wronskian determinant for  $K_n$  and  $I_n$ , we readily determine  $A_1$  and  $A_2$ , and obtain

$$\tilde{G}_n(\rho; \rho_0, \theta_0) = \left[ K_n\left(\frac{\rho_{>}}{\sqrt{D}}\right) - \frac{K'_n\left(\frac{1}{\sqrt{D}}\right)}{I'_n\left(\frac{1}{\sqrt{D}}\right)} I_n\left(\frac{\rho_{>}}{\sqrt{D}}\right) \right] e^{in\theta_0} I_n\left(\frac{\rho_{<}}{\sqrt{D}}\right), \quad 0 < \rho < 1, \quad (\text{A.4})$$

where we have define  $\rho_{<} = \min(\rho_0, \rho)$  and  $\rho_{>} = \max(\rho_0, \rho)$ . Therefore, the Fourier expansion for the reduced-wave Green's function satisfying (A.1) is

$$G(\rho, \theta; \rho_0, \theta_0) = \frac{1}{2\pi} \sum_{n=-\infty}^{\infty} e^{-in(\theta-\theta_0)} \left[ K_n\left(\frac{\rho_{>}}{\sqrt{D}}\right) - \frac{K'_n\left(\frac{1}{\sqrt{D}}\right)}{I'_n\left(\frac{1}{\sqrt{D}}\right)} I_n\left(\frac{\rho_{>}}{\sqrt{D}}\right) \right] I_n\left(\frac{\rho_{<}}{\sqrt{D}}\right), \quad 0 < \rho < 1. \quad (\text{A.5})$$

The infinite series representation (A.5) converges very slowly. To improve the convergence properties, we must extract from  $G$  the free-space Green's function  $G_f$ , which has the Fourier representation

$$G_f(\rho, \theta; \rho_0, \theta_0) = \frac{1}{2\pi} \left( K_0\left(\frac{|\mathbf{x} - \mathbf{x}_0|}{\sqrt{D}}\right) \right) = \frac{1}{2\pi} \sum_{n=-\infty}^{\infty} e^{-in(\theta-\theta_0)} K_n\left(\frac{\rho_{>}}{\sqrt{D}}\right) I_n\left(\frac{\rho_{<}}{\sqrt{D}}\right), \quad 0 < \rho < 1, \quad (\text{A.6})$$

where  $|\mathbf{x} - \mathbf{x}_0| \equiv \sqrt{\rho^2 + \rho_0^2 - 2\rho\rho_0 \cos(\theta - \theta_0)}$ . Then, we can decompose  $G$  in (A.5) as

$$G(\rho, \theta; \rho_0, \theta_0) = \frac{1}{2\pi} K_0\left(\frac{|\mathbf{x} - \mathbf{x}_0|}{\sqrt{D}}\right) - \frac{1}{2\pi} \sum_{n=-\infty}^{\infty} e^{-in(\theta-\theta_0)} \frac{K'_n\left(\frac{1}{\sqrt{D}}\right)}{I'_n\left(\frac{1}{\sqrt{D}}\right)} I_n\left(\frac{\rho_0}{\sqrt{D}}\right) I_n\left(\frac{\rho}{\sqrt{D}}\right), \quad 0 < \rho < 1. \quad (\text{A.7})$$

In (A.7), the first term arises from the source at  $(\rho_0, \theta_0)$ , while the infinite sum represents the effects of the boundary conditions. Then, we use  $K_{-n}(z) = K_n(z)$  and  $I_{-n}(z) = I_n(z)$  to further simplify (A.7) to

$$\begin{aligned} G(\rho, \theta; \rho_0, \theta_0) &= \frac{1}{2\pi} K_0\left(\frac{R}{\sqrt{D}}\right) - \frac{1}{2\pi} \frac{K'_0\left(\frac{1}{\sqrt{D}}\right)}{I'_0\left(\frac{1}{\sqrt{D}}\right)} I_0\left(\frac{\rho_0}{\sqrt{D}}\right) I_0\left(\frac{\rho}{\sqrt{D}}\right) + \frac{1}{\pi} \delta_M \\ &\quad - \frac{1}{\pi} \sum_{n=1}^M \cos(n(\theta - \theta_0)) \frac{K'_n\left(\frac{1}{\sqrt{D}}\right)}{I'_n\left(\frac{1}{\sqrt{D}}\right)} I_n\left(\frac{\rho_0}{\sqrt{D}}\right) I_n\left(\frac{\rho}{\sqrt{D}}\right), \quad 0 < \rho < 1. \end{aligned} \quad (\text{A.8})$$

Since  $K'_n\left(\frac{1}{\sqrt{D}}\right) < 0$ , and  $I'_n\left(\frac{1}{\sqrt{D}}\right) > 0$  for any integer  $n \geq 0$ , then  $\delta_M$  is a small error term bounded by

$$|\delta_M| \leq P_M \equiv - \sum_{n=M+1}^{\infty} \frac{K'_n\left(\frac{1}{\sqrt{D}}\right)}{I'_n\left(\frac{1}{\sqrt{D}}\right)} I_n\left(\frac{\rho_0}{\sqrt{D}}\right) I_n\left(\frac{\rho}{\sqrt{D}}\right).$$

In Table A 1, we give the number  $M$  of Fourier terms in (A.8) required to calculate the reduced-wave Green's function within a tolerance of  $10^{-8}$ . The series for  $P_M$  is found to converge fairly fast, especially when the singular point is not close to the boundary of the unit circle and/or  $D$  is not too large. Equation (A.8) for  $G$  with  $P_M < 10^{-8}$

| $\rho_0$ | $\rho$ | $M$ | $P_M$       |
|----------|--------|-----|-------------|
| 0.8      | 0.8    | 31  | 8.1737e-009 |
| 0.8      | 0.5    | 16  | 6.7405e-009 |
| 0.8      | 0.2    | 8   | 9.5562e-009 |
| 0.5      | 0.5    | 11  | 4.3285e-009 |

Table A 1. *The number of Fourier terms needed to determine  $G$  to within a tolerance  $10^{-8}$  for  $D = 1$ .*

is the one used in the numerical simulations in §6–7. From (A.8) we can readily extract the self-interaction, or regular part,  $R$  of the reduced-wave Green’s function, as written in (1.2 *b*). The gradients of  $R$  and  $G$  that are needed in Principal Result 3.1 to determine the motion of a collection of spots are determined numerically from (A.8).

### A.2 Neumann Green’s Function for a Unit Disk

For  $D \gg \mathcal{O}(1)$ , we recall from (2.12) that the reduced-wave Green’s function and its regular part can be approximated by the Neumann Green’s function  $G^{(N)}(\mathbf{x}; \mathbf{x}_0)$  and its regular part  $R^{(N)}(\mathbf{x}; \mathbf{x}_0)$  satisfying (2.13). For the unit disk, this Neumann Green’s function and its regular part are defined in cartesian coordinates by (see eq. (4.3) of [32]),

$$G^{(N)}(\mathbf{x}; \mathbf{x}_0) = \frac{1}{2\pi} \left( -\ln |\mathbf{x} - \mathbf{x}_0| - \ln \left| \mathbf{x} |\mathbf{x}_0| - \frac{\mathbf{x}_0}{|\mathbf{x}_0|} \right| + \frac{1}{2} (|\mathbf{x}|^2 + |\mathbf{x}_0|^2) - \frac{3}{4} \right), \quad (\text{A.9 } a)$$

$$R^{(N)}(\mathbf{x}_0; \mathbf{x}_0) = \frac{1}{2\pi} \left( -\ln (1 - |\mathbf{x}_0|^2) + |\mathbf{x}_0|^2 - \frac{3}{4} \right). \quad (\text{A.9 } b)$$

The gradients of these quantities can be obtained by a simple calculation as

$$\nabla G^{(N)}(\mathbf{x}; \mathbf{x}_0) = -\frac{1}{2\pi} \left[ \frac{(\mathbf{x} - \mathbf{x}_0)}{|\mathbf{x} - \mathbf{x}_0|^2} + \frac{|\mathbf{x}_0|^2}{\bar{\mathbf{x}} |\mathbf{x}_0|^2 - \bar{\mathbf{x}}_0} - \mathbf{x} \right], \quad \nabla R^{(N)}(\mathbf{x}_0; \mathbf{x}_0) = \frac{1}{2\pi} \left( \frac{2 - |\mathbf{x}_0|^2}{1 - |\mathbf{x}_0|^2} \right) \mathbf{x}_0,$$

where the overbar denotes complex conjugate. In §6–7 these results allow us to explicitly determine the dynamics of a collection of spots inside a disk when  $D$  is large, as characterized in Principal Result 3.1 of §3.

When  $\Omega$  is the unit disk, and for two specific sets of source and observation points in  $\Omega$ , in Table A 2 we give numerical results for the two-term approximation (see equation (2.12))

$$G \sim \tilde{G} \equiv \frac{D}{|\Omega|} + G^{(N)}, \quad R \sim \tilde{R} \equiv \frac{D}{|\Omega|} + R^{(N)}, \quad (\text{A.10})$$

with  $|\Omega| = \pi$ , which relates the reduced-wave and Neumann Green’s functions when  $D$  is large. The results for  $G^{(N)}$ ,  $R^{(N)}$ ,  $G$ , and  $R$ , were computed from (A.9) and (A.8). The results in Table A 2 are believed to be correct to the number of digits shown, and confirm that  $G \approx \tilde{G}$  and  $R \approx \tilde{R}$  when  $D$  is large.

### A.3 Green’s Function for a Rectangle

Next, we calculate the reduced-wave Green’s function  $G(x, y; x_0, y_0)$  in the rectangular domain  $\Omega = [0, L] \times [0, d]$ . Since the free-space Green’s function  $G_f$  is given by  $G_f(\mathbf{x}; \mathbf{x}_0) = (2\pi)^{-1} K_0(|\mathbf{x} - \mathbf{x}_0|/\sqrt{D})$ , we can use the method

|      | $(\rho, \rho_0, \theta - \theta_0) = (0.3, 0.5, 0.0)$ |             |          |             | $(\rho, \rho_0, \theta - \theta_0) = (0.8, 0.2, \pi/6)$ |             |          |             |
|------|---|-------------|----------|-------------|---|-------------|----------|-------------|
| $D$  | $G$   | $\tilde{G}$ | $R$      | $\tilde{R}$ | $G$   | $\tilde{G}$ | $R$      | $\tilde{R}$ |
| 0.1  | 0.12182   | 0.22154     | -0.15651 | -0.00196    | 0.02473   | 0.06198     | -0.16303 | -0.07467    |
| 1.0  | 0.48316   | 0.50802     | 0.24622  | 0.28452     | 0.33490   | 0.34846     | 0.19617  | 0.21181     |
| 4.0  | 1.45566   | 1.46295     | 1.22822  | 1.23945     | 1.29922   | 1.30339     | 1.16243  | 1.16674     |
| 10.0 | 3.36978   | 3.37281     | 3.14465  | 3.14931     | 3.21150   | 3.21325     | 3.07484  | 3.07660     |

Table A 2. Comparison of results for the reduced-wave Green's function  $G$  and its regular part  $R$  for the unit disk with the two-term large  $D$  approximation  $\tilde{G}$  and  $\tilde{R}$ , as given in (A.10). The comparison is made at two sets of source and observation points in  $\Omega$ . For  $D$  large, we note that  $G \approx \tilde{G}$  and  $R \approx \tilde{R}$ , as expected.

of images to write the solution to (1.2) as

$$G(\mathbf{x}; \mathbf{x}_0) = \frac{1}{2\pi} \sum_{n=-\infty}^{\infty} \sum_{m=-\infty}^{\infty} \sum_{l=1}^4 K_0 \left( \frac{|\mathbf{x} - \mathbf{x}_{mn}^{(l)}|}{\sqrt{D}} \right), \quad (\text{A.11 } a)$$

$$\mathbf{x}_{mn}^{(1)} = (x_0 + 2nL, y_0 + 2md), \quad \mathbf{x}_{mn}^{(2)} = (-x_0 + 2nL, y_0 + 2md), \quad (\text{A.11 } b)$$

$$\mathbf{x}_{mn}^{(3)} = (x_0 + 2nL, -y_0 + 2md), \quad \mathbf{x}_{mn}^{(4)} = (-x_0 + 2nL, -y_0 + 2md). \quad (\text{A.11 } c)$$

Since  $K_0(r)$  decays exponentially as  $r \rightarrow \infty$ , then the infinite series in (A.11) converges fairly rapidly when  $D = \mathcal{O}(1)$ . The regular part of the reduced-wave Green's function together with the gradients of  $G$  and  $R$ , as required in Principal Result 3.1, are readily evaluated numerically from (A.11).

#### A.4 Neumann Green's Function for a Rectangle

For  $D \gg \mathcal{O}(1)$  is large, we can approximate  $G$  and its regular part  $R$  by the corresponding Neumann Green's function  $G^{(N)}$  and its regular part  $R^{(N)}$  by the two-term expansion in (2.12). This latter Green's function, calculated by an analytical Ewald-type summation method, was given analytically in formula (4.13) of [38] as

$$G^{(N)}(\mathbf{x}; \mathbf{x}_0) = -\frac{1}{2\pi} \ln |\mathbf{x} - \mathbf{x}_0| + R^{(N)}(\mathbf{x}; \mathbf{x}_0), \quad (\text{A.12 } a)$$

where  $R^{(N)}(\mathbf{x}; \mathbf{x}_0)$  is given explicitly by

$$R^{(N)}(\mathbf{x}; \mathbf{x}_0) = -\frac{1}{2\pi} \sum_{n=0}^{\infty} \ln(|1 - q^n z_{+,+}| |1 - q^n z_{+,-}| |1 - q^n z_{-,+}| |1 - q^n z_{-,-}| |1 - q^n \zeta_{+,+}| |1 - q^n \zeta_{+,-}| |1 - q^n \zeta_{-,+}| |1 - q^n \zeta_{-,-}|) \\ + \frac{L}{d} \left[ \frac{1}{3} - \frac{\max(x, x_0)}{L} + \frac{1}{2} \left( \frac{x_0^2 + x^2}{L^2} \right) \right] - \frac{1}{2\pi} \ln \left( \frac{|1 - z_{-,-}|}{|r_{-,-}|} \right) - \frac{1}{2\pi} \sum_{n=1}^{\infty} \ln |1 - q^n z_{-,-}|. \quad (\text{A.12 } b)$$

Here points in the rectangle are written as complex numbers. In (A.12 b),  $q \equiv e^{-2L\pi/d}$ , while the eight complex-valued constants  $z_{\pm,\pm}$  and  $\zeta_{\pm,\pm}$  are given by

$$z_{+,\pm} \equiv \exp(\mu(-|x + x_0| + i(y \pm y_0))/2), \quad z_{-,\pm} \equiv \exp(\mu(-|x - x_0| + i(y \pm y_0))/2), \quad (\text{A.12 } c)$$

$$\zeta_{+,\pm} \equiv \exp(\mu(|x + x_0| - 2L + i(y \pm y_0))/2), \quad \zeta_{-,\pm} \equiv \exp(\mu(|x - x_0| - 2L + i(y \pm y_0))/2). \quad (\text{A.12 } d)$$

Here  $\mu$  is defined by  $\mu = 2\pi/d$ . The self-interaction term  $R^{(N)}(\mathbf{x}_0; \mathbf{x}_0)$ , and the gradients of  $R^{(N)}$  and  $G^{(N)}$  can be calculated readily from (A.12). In particular, for the unit square  $[0, 1] \times [0, 1]$  with a singularity at the middle

$\mathbf{x}_0 \equiv (0.5, 0.5)$  the self-interaction term  $R_{0,0}^{(N)} \equiv R^{(N)}(\mathbf{x}_0; \mathbf{x}_0)$  calculated from (A.12) is simply

$$R_{00}^{(N)} = -\frac{1}{\pi} \sum_{n=1}^{\infty} \ln(1 - q^n) + \frac{1}{12} - \frac{1}{2\pi} \ln(2\pi), \quad q \equiv e^{-2\pi}. \quad (\text{A.13})$$

## Appendix B Survey of NLEP Theory: Comparison of Quasi-Equilibria and Stability

In [60], the existence and stability of a one-spot pattern to the GS model on the infinite plane  $\mathbb{R}^2$  was studied. For this infinite-plane problem, we can set  $D = 1$  in (1.1). In the inner region near the spot, the leading-order analysis of [60] in terms of  $\nu \equiv -1/\ln \varepsilon$  and for  $A = \mathcal{O}(\varepsilon[-\ln \varepsilon]^{1/2})$ , showed that  $u \sim u_0$ , where  $u_0$  is locally constant near the spot. Moreover,  $v \sim v_0 = w(\rho)/(Au_0)$ , where  $w(\rho)$  is the radially symmetric ground-state solution of

$$\Delta_\rho w - w + w^2 = 0, \quad 0 < \rho < \infty; \quad w(0) > 0, \quad w'(0) = 0; \quad w \rightarrow 0 \text{ as } \rho \rightarrow \infty, \quad (\text{B.1})$$

where  $\Delta_\rho w \equiv w'' + \rho^{-1}w'$ . For  $\varepsilon \rightarrow 0$ , it was shown in [60] that  $u_0$  satisfies the quadratic equation

$$1 - u_0 \sim \frac{L}{u_0}, \quad L \equiv \frac{\varepsilon^2}{\nu A^2} \int_0^\infty w^2 \rho d\rho, \quad \nu \equiv -\frac{1}{\ln \varepsilon}. \quad (\text{B.2})$$

Therefore, the existence condition for a one-spot equilibrium solution is that

$$L \leq \frac{1}{4} \quad \Rightarrow \quad A \geq A_{fw} \equiv 2\varepsilon \sqrt{\frac{b_0}{\nu}}, \quad b_0 \equiv \int_0^\infty w^2(\rho) \rho d\rho. \quad (\text{B.3})$$

Define  $L_0$  and  $\gamma$  by  $L_0 = \lim_{\varepsilon \rightarrow 0} L = \mathcal{O}(1)$  and  $\gamma \equiv \nu \ln \tau = \mathcal{O}(1)$ , so that  $\tau = \mathcal{O}(\varepsilon^{-\gamma})$ , and assume that  $0 \leq \gamma < 2$ . Then, the following radially symmetric nonlocal eigenvalue problem (NLEP) was derived in equation (5.5) of [60]:

$$\Delta_\rho \psi_0 - \psi_0 + 2w\psi_0 - \frac{2(1 - u_0)(2 - \gamma)}{2u_0 + (1 - u_0)(2 - \gamma)} w^2 \frac{\int_0^\infty w\psi_0 \rho d\rho}{\int_0^\infty w^2 \rho d\rho} = \lambda \psi_0, \quad 0 < \rho < \infty, \quad (\text{B.4})$$

with  $\psi_0 \rightarrow 0$  as  $\rho \rightarrow \infty$ . An analysis of this NLEP in [60] led to Theorem 2.2 of [60], which we summarize as follows:

- (1) There exists a saddle node bifurcation at  $L_0 = \frac{1}{4}$ , such that there are two equilibrium solutions  $u_0^\pm$  given by  $u_0^\pm = (1 \pm \sqrt{1 - 4L_0})/2$  for  $L_0 < \frac{1}{4}$ , and no equilibrium solutions when  $L_0 > \frac{1}{4}$ .
- (2) Assume that  $0 \leq \gamma < 2$  and  $L_0 < \frac{1}{4}$ . Then, the solution branch  $(u_0^+, v_0^+)$  is linearly unstable.
- (3) Assume that  $0 \leq \gamma < 2$ . Then, the other solution branch  $(u_0^-, v_0^-)$  is linearly unstable if

$$L_0 > \frac{1}{4} \left[ 1 - \left( \frac{\gamma}{4 - \gamma} \right)^2 \right], \quad \Rightarrow \quad A < A_{sw} \equiv A_{fw} \left[ 1 - \left( \frac{\gamma}{4 - \gamma} \right)^2 \right]^{-1/2}. \quad (\text{B.5})$$

- (4) Assume that  $\gamma = 0$  and  $L_0 < \frac{1}{4}$ . Then,  $(u_0^-, v_0^-)$  is linearly stable.
- (5) If  $0 \leq \gamma < 2$ , the stability of  $(u_0^-, v_0^-)$  is unknown for  $A > A_{sw}$ .

We remark that the saddle-node bifurcation value of  $A$ , obtained from (B.2), has the scaling  $A = \mathcal{O}(\varepsilon[-\ln \varepsilon]^{1/2})$  as  $\varepsilon \rightarrow 0$ . The stability results listed above from [60] also relate only to this range in  $A$ . However, the quasi-equilibrium spot solution given in Principal Result 2.1 of §2, and the spot self-replication threshold of Principal Result 4.1, occur for the slightly larger range  $A = \mathcal{O}(\varepsilon[-\ln \varepsilon])$ . Consequently, the occurrence of spot self-replication behavior for the GS model (1.1) was not observed in the scaling regime for  $A$  considered in [60]. In §5.1 we compare the Hopf Bifurcation threshold predicted by (B.5) with that obtained from our global eigenvalue problem of §4.2.

### B.1 NLEP Theory for $k$ -Spot Patterns

In [62] a related theoretical approach, based on the rigorous analysis of other NLEP's, was used to obtain a leading-order asymptotic theory for the existence and stability of  $k$ -spot patterns to the GS model (1.1) in a bounded two-dimensional domain. In the inner region near the  $j^{\text{th}}$  spot centered at  $\mathbf{x}_j$ , the leading-order-in- $\nu$  scaling in [62] showed that  $u \sim u_j$ , where  $u_j$  is a constant, and that  $v$  satisfies  $v \sim v_j \equiv \frac{1}{Au_j}w(\rho)$ , where  $w(\rho)$  is the radially symmetric solution of (B.1). Moreover, the  $u_j$  for  $j = 1, \dots, k$  satisfy the nonlinear algebraic system (cf. [62])

$$1 - u_j - \frac{\eta_\varepsilon L_\varepsilon}{u_j} \sim \sum_{i=1}^k \frac{L_\varepsilon}{u_i}, \quad (\text{B.6})$$

where  $L_\varepsilon$  and  $\eta_\varepsilon$  are defined in terms of the area  $|\Omega|$  of the domain by

$$L_\varepsilon \equiv \frac{2\varepsilon^2 \pi b_0}{A^2 |\Omega|}, \quad \eta_\varepsilon \equiv \frac{|\Omega|}{2\pi D\nu}, \quad b_0 \equiv \int_0^\infty w^2 \rho d\rho, \quad \nu \equiv -\frac{1}{\ln \varepsilon}. \quad (\text{B.7})$$

For the case where  $u_j = u_0$  for  $j = 1, \dots, k$ , then (B.6) is a quadratic equation for  $u_j$ , which leads to the following three main parameter regimes of [62]:

$$\left\{ \begin{array}{ll} 4kL_0 < 1, & \text{for } \eta_\varepsilon \rightarrow 0 \Leftrightarrow D \gg \mathcal{O}(\nu^{-1}), \\ 4\eta_\varepsilon L_\varepsilon < 1, & \text{for } \eta_\varepsilon \rightarrow \infty \Leftrightarrow D = \mathcal{O}(1), \\ 4(k + \eta_0)L_0 < 1, & \text{for } \eta_\varepsilon \rightarrow \eta_0 \Leftrightarrow D = \mathcal{O}(\nu^{-1}), \end{array} \right. \quad L_0 = \lim_{\varepsilon \rightarrow 0} L_\varepsilon = \mathcal{O}(1), \quad \eta_0 = \lim_{\varepsilon \rightarrow 0} \eta_\varepsilon = \mathcal{O}(1). \quad (\text{B.8})$$

From (B.7), the second line in (B.8) is for  $A = \mathcal{O}(\varepsilon[-\ln \varepsilon]^{1/2})$  with  $D = \mathcal{O}(1)$ , while the third line in (B.8) is for  $A = \mathcal{O}(\varepsilon)$  with  $D = \mathcal{O}(\nu^{-1})$ .  $\nu = -1/\ln \varepsilon$ . Thus, the  $k$ -spot quasi-equilibrium patterns of [62] do not correspond to the range  $A = \mathcal{O}(\varepsilon[-\ln \varepsilon])$  and  $D = \mathcal{O}(1)$ , considered in §2, where spot-splitting can occur.

As shown in [62], the leading-order quasi-equilibrium solution satisfies  $u_j \sim u_0^\pm$  in the inner region. The global representation for  $v$  is  $v \sim v_0^\pm$ . Here  $u_0^\pm$  and  $v_0^\pm$  satisfy

$$u_0^\pm \sim \left\{ \begin{array}{ll} \frac{1}{2}(1 \pm \sqrt{1 - 4kL_0}), & \text{for } D \gg \mathcal{O}(\nu^{-1}), \\ \frac{1}{2}(1 \pm \sqrt{1 - 4\eta_\varepsilon L_\varepsilon}), & \text{for } D = \mathcal{O}(1), \\ \frac{1}{2}(1 \pm \sqrt{1 - 4(k + \eta_0)L_0}), & \text{for } D = \mathcal{O}(\nu^{-1}), \end{array} \right. \quad v_0^\pm \sim \sum_{j=1}^k \frac{1}{Au_0^\pm} w(\varepsilon^{-1}|\mathbf{x} - \mathbf{x}_j|). \quad (\text{B.9})$$

The stability analysis in [62] was largely based on the derivation and analysis of the radially symmetric NLEP

$$\Delta_\rho \psi - \psi + 2w\psi - \gamma w^2 \frac{\int_0^\infty w\psi \rho d\rho}{\int_0^\infty w^2 \rho d\rho} = \lambda \psi, \quad 0 < \rho < \infty; \quad \psi \rightarrow 0, \quad \rho \rightarrow \infty. \quad (\text{B.10 } a)$$

In terms of  $u_0 = u_0^\pm$  and  $\tau = \mathcal{O}(1)$ , in (B.10 a) there are two choices for  $\gamma$  given by

$$\gamma = \frac{2\eta_\varepsilon L_\varepsilon(1 + \tau\lambda) + kL_\varepsilon}{(u_0^2 + L_\varepsilon \eta_\varepsilon)(1 + \tau\lambda) + kL_\varepsilon}, \quad \text{or} \quad \gamma = \frac{2\eta_\varepsilon L_\varepsilon}{u_0^2 + L_\varepsilon \eta_\varepsilon}. \quad (\text{B.10 } b)$$

Assuming that the third condition in (B.8) holds, Theorem 2.3 of [62] gives a stability result for  $k$ -spot equilibrium solution based on an analysis of the NLEP (B.10), together with certain properties of  $\mathcal{F}(\mathbf{x}_1, \dots, \mathbf{x}_k)$  defined by

$$\mathcal{F}(\mathbf{x}_1, \dots, \mathbf{x}_k) = - \sum_{i=1}^k \sum_{j=1}^k (\mathcal{G})_{ij}. \quad (\text{B.11})$$

Here  $\mathcal{G}$  is the Green's matrix of (2.9) defined in terms of the reduced-wave Green's function. From [62], an equilibrium spot pattern must be at a critical point of  $\mathcal{F}$ . We denote by  $\mathcal{H}_0$  the Hessian of  $\mathcal{F}$  at this critical point.

Suppose that  $4(\eta_\varepsilon + k)L_\varepsilon < 1/4$ . Then, Theorem 2.3 of [62] proves that the large solutions  $(u^+, v^+)$  are all linearly unstable. For the small solutions  $(u^-, v^-)$ , this theorem provides the following results for three ranges of  $\eta_\varepsilon$ :

(1) Assume that  $\eta_\varepsilon \rightarrow 0$ , so that  $D \gg \mathcal{O}(\nu^{-1})$ . Then,

- If  $k = 1$ , and all the eigenvalues of the Hessian  $\mathcal{H}_0$  are negative, then there exists a unique  $\tau_1 > 0$ , with  $\tau_1 = \mathcal{O}(1)$ , such that for  $\tau < \tau_1$ ,  $(u^-, v^-)$  is linearly stable, while for  $\tau > \tau_1$ , it is linearly unstable.
- If  $k > 1$ ,  $(u^-, v^-)$  is linearly unstable for any  $\tau \geq 0$ .
- If the Hessian  $\mathcal{H}_0$  has a strictly positive eigenvalue, then  $(u^-, v^-)$  is linearly unstable for any  $\tau \geq 0$ .

(2) Assume that  $\eta_\varepsilon \rightarrow \infty$ , so that  $D \ll \mathcal{O}(\nu^{-1})$ . Then,

- If all the eigenvalues of the Hessian  $\mathcal{H}_0$  are negative, then  $(u^-, v^-)$  is linearly stable for any  $\tau > 0$ .
- If the Hessian  $\mathcal{H}_0$  has a strictly positive eigenvalue,  $(u^-, v^-)$  is linearly unstable for any  $\tau \geq 0$ .

(3) Assume that  $\eta_\varepsilon \rightarrow \eta_0$ , so that  $D = \mathcal{O}(\nu^{-1})$ . The following results hold:

- If  $L_0 < \frac{\eta_0}{(2\eta_0+k)^2}$ , and all eigenvalues of  $\mathcal{H}_0$  are negative, then  $(u^-, v^-)$  is linearly stable for  $\tau = \mathcal{O}(1)$  sufficiently small or  $\tau = \mathcal{O}(1)$  sufficiently large.
- If  $k = 1$ ,  $L_0 > \frac{\eta_0}{(2\eta_0+1)^2}$ , and all the eigenvalues of  $\mathcal{H}_0$  are negative, then there exists  $\tau_2 > 0$ ,  $\tau_3 > 0$ , such that for  $\tau < \tau_2$ ,  $(u^-, v^-)$  is linearly stable, while for  $\tau > \tau_3$ , it is linearly unstable.
- If  $k > 1$  and  $L_0 > \frac{\eta_0}{(2\eta_0+k)^2}$ , then  $(u^-, v^-)$  is linearly unstable for any  $\tau > 0$ .
- If the Hessian  $\mathcal{H}_0$  has a strictly positive eigenvalue,  $(u^-, v^-)$  is linearly unstable for any  $\tau \geq 0$ .

We now relate these results of [62] with those obtained in §2–4. Firstly, the condition of [62] that an equilibrium  $k$ -spot configuration  $\mathbf{x}_1, \dots, \mathbf{x}_k$  must be at a critical point of  $\mathcal{F}$  in (B.11) is equivalent to the equilibrium result in (3.8) of Principal Result 3.1 provided that we replace the source strengths  $S_{je}$  in (3.8) with their leading-order-in- $\nu$  asymptotically common value  $S_c \sim \mathcal{A}$ , as obtained from (2.11). The stability condition of [62] expressed in terms of the sign of the eigenvalues of the Hessian  $\mathcal{H}_0$  of  $\mathcal{F}$  is equivalent to the statement that the equilibrium spot configuration  $\mathbf{x}_1, \dots, \mathbf{x}_k$  is stable with respect to the slow motion ODE dynamics of Principal Result 3.1 of §3 when we use the leading-order approximation  $S_j \sim S_c$  for  $j = 1, \dots, k$ . Therefore, the condition on the Hessian  $\mathcal{H}_0$  in [62] relates to the small eigenvalues of order  $\mathcal{O}(\varepsilon^2)$  in the linearization.

In addition, the second result of Theorem 2.3 of [62] for  $\eta_\varepsilon \rightarrow \infty$ , as written above, includes the range  $D = \mathcal{O}(1)$ . The condition  $4(\eta_\varepsilon + k)L_\varepsilon < 1/4$ , together with (B.7) relating  $L_\varepsilon$  to  $A$ , shows that this second result of [62] holds when  $A = \mathcal{O}(\varepsilon[-\ln \varepsilon]^{1/2})$ . Therefore, for this range of  $A$  and  $D$ , the leading order NLEP analysis in [62] predicts that there is an equilibrium solution branch whose stability depends only on the eigenvalues of the Hessian matrix  $\mathcal{H}_0$ . This result is very similar to that obtained from our global eigenvalue problem in Principal Result 4.2 of §4.2 (see Fig. 9(a)) for the nearby parameter range  $A = \mathcal{O}(-\varepsilon \ln \varepsilon)$ . There, we showed to leading-order in  $\nu$  that a  $k$ -spot quasi-equilibrium solution is stable to competition or oscillatory instabilities when  $D = \mathcal{O}(1)$  and  $A = \mathcal{O}(-\varepsilon \ln \varepsilon)$ .

With the exception of the condition on the Hessian matrix of  $\mathcal{F}$ , these stability results of [62] depend only on the number  $k$  of spots, and not on their spatial locations within  $\Omega$ . This is qualitatively very different to that obtained in §5–§6 from our globally coupled eigenvalue problem, which accounts for all terms in powers of  $\nu$ .



## B.2 Comparison of the Quasi-Equilibrium Solutions

In this subsection we show that our asymptotic construction of quasi-equilibrium  $k$ -spot solutions, as given in Principal Result 2.1 of §2, can be reduced to that given in [62] when  $\mathcal{A} = \mathcal{O}(\nu^{1/2})$  in (2.7). Note that when  $\mathcal{A} = \mathcal{O}(\nu^{1/2})$ , then from (2.5),  $A = \mathcal{O}(\varepsilon[-\ln \varepsilon]^{1/2})$ , which is the key parameter regime of [62].

For  $\mathcal{A} = \mathcal{O}(\nu^{1/2})$ , (2.7) together with the core problem (2.3), suggest that we expand  $U_j$ ,  $V_j$ ,  $S_j$ , and  $\chi$ , in (2.3) as

$$\begin{aligned}\chi &\sim \nu^{-1/2}(\chi_{0j} + \nu\chi_{1j} + \cdots), & U_j &\sim \nu^{-1/2}(U_{0j} + \nu U_{1j} + \cdots), \\ S_j &\sim \nu^{1/2}(S_{0j} + \nu S_{1j} + \cdots), & V_j &\sim \nu^{1/2}(V_{0j} + \nu V_{1j} + \cdots).\end{aligned}\tag{B.12}$$

Upon substituting (B.12) into (2.3), and collecting powers of  $\nu$ , we obtain the leading-order problem

$$\Delta U_{0j} = 0, \quad U_{0j} \rightarrow \chi_{0j} \quad \text{as } \rho \rightarrow \infty; \quad \Delta V_{0j} - V_{0j} + U_{0j}V_{0j}^2 = 0, \quad V_{0j} \rightarrow 0 \quad \text{as } \rho \rightarrow \infty.\tag{B.13}$$

The solution to (B.13) is  $U_{0j} = \chi_{0j}$ , and  $V_{0j} = w/\chi_{0j}$ , where  $w(\rho)$  satisfies (B.1). At next order, we get

$$\Delta U_{1j} = U_{0j}V_{0j}^2, \quad U_{1j} \rightarrow S_{0j} \ln \rho + \chi_{1j} \quad \text{as } \rho \rightarrow \infty,\tag{B.14 a}$$

$$\Delta V_{1j} - V_{1j} + 2U_{0j}V_{0j}V_{1j} = -U_{1j}V_{0j}^2, \quad V_{1j} \rightarrow 0 \quad \text{as } \rho \rightarrow \infty.\tag{B.14 b}$$

At one higher order, we find that  $U_{2j}$  satisfies

$$\Delta U_{2j} = 2U_{0j}V_{0j}V_{1j} + V_{0j}^2U_{1j}, \quad U_{2j} \rightarrow S_{1j} \ln \rho + \chi_{2j} \quad \text{as } \rho \rightarrow \infty.\tag{B.15}$$

Upon applying the divergence theorem to (B.14 a), and using  $U_{0j} = \chi_{0j}$  and  $V_{0j} = w/\chi_{0j}$ , we obtain

$$S_{0j} = \int_0^\infty U_{0j}V_{0j}^2 \rho d\rho = \frac{b_0}{\chi_{0j}}, \quad b_0 \equiv \int_0^\infty w^2 \rho d\rho,\tag{B.16}$$

which determines  $S_{0j}$  in terms of  $\chi_{0j}$ . We then decompose the solution to (B.14) in the form

$$U_{1j} = \frac{1}{\chi_{0j}}(\chi_{0j}\chi_{1j} + \hat{U}_{1j}), \quad V_{1j} = \frac{1}{\chi_{0j}^3}(-\chi_{0j}\chi_{1j}w + \hat{V}_{1j}),$$

where  $\hat{U}_{1j}$  and  $\hat{V}_{1j}$  are the unique solutions on  $0 < \rho < \infty$  of

$$\Delta_\rho \hat{U}_{1j} = w^2, \quad \Delta_\rho \hat{V}_{1j} - \hat{V}_{1j} + 2w\hat{V}_{1j} = -\hat{U}_{1j}w^2; \quad \hat{V}_{1j} \rightarrow 0 \quad \hat{U}_{1j} - b_0 \ln \rho \rightarrow 0, \quad \text{as } \rho \rightarrow \infty.\tag{B.17}$$

Similarly, by applying the divergence theorem to (B.15), we calculate  $S_{1j}$  as

$$S_{1j} = -\frac{b_0\chi_{1j}}{\chi_{0j}^2} + \frac{b_1}{\chi_{0j}^3}, \quad b_1 \equiv \int_0^\infty (w^2\hat{U}_{1j} + 2w\hat{V}_{1j}) \rho d\rho.\tag{B.18}$$

The BVP solver COLSYS (cf. [2]) is used to numerically compute the ground-state solution  $w(\rho)$  together with the solutions  $\hat{U}_{1j}$  and  $\hat{V}_{1j}$  of (B.17). Then, from a simple numerical quadrature, we estimate  $b_0 \approx 4.9347$  and  $b_1 \approx 0.8706$ .

Finally, upon substituting (B.16) and (B.18) into the nonlinear algebraic system (2.7) of §2, we obtain that

$$\mathcal{A} = \nu^{1/2} \left( \chi_{0j} + \frac{b_0}{\chi_{0j}} \right) + \nu^{3/2} \left[ \frac{b_1}{\chi_{0j}^3} + \left( 1 - \frac{b_0}{\chi_{0j}^2} \right) \chi_{1j} + 2\pi \left( \frac{b_0}{\chi_{0j}} R_{j,j} + \sum_{i \neq j}^k \frac{b_0}{\chi_{0i}} G_{ij} \right) \right].\tag{B.19}$$

For a prescribed  $\mathcal{A}$  with  $\mathcal{A} = \mathcal{A}_0\nu^{1/2} + \mathcal{A}_1\nu^{3/2} + \cdots$ , we could then calculate  $\chi_{0j}$  and  $\chi_{1j}$  from (B.19). Since  $\mathcal{A} = \mathcal{O}(\nu^{1/2})$  corresponds to  $A = \mathcal{O}(\varepsilon[-\ln \varepsilon]^{1/2})$ , we conclude that it is in this parameter range that the coupled core problem (2.3) reduces to the scalar ground-state problem for  $v$ , as was exploited in [62].

Finally, we show that (B.19) reduces to the expression (B.6) used in [62]. To see this, we note from (2.1) that

$\mathcal{A} = A\sqrt{D}\nu/\varepsilon$  and  $u_j = \varepsilon U_j/(A\sqrt{D}) \approx \varepsilon\nu^{-1/2}\chi_{0j}/(A\sqrt{D})$ . Moreover, for  $D \gg \mathcal{O}(1)$ , we use  $R_{j,j} = \frac{D}{|\Omega|} + \mathcal{O}(1)$ , and  $G_{ij} = \frac{D}{|\Omega|} + \mathcal{O}(1)$  for  $i \neq j$  (see equation (2.12) of §2). Then, from (B.19), we obtain

$$\frac{A\sqrt{D}\nu}{\varepsilon} \sim \frac{A\sqrt{D}\nu}{\varepsilon}u_j + \frac{b_0\varepsilon}{A\sqrt{D}u_j} + \frac{2\pi\nu D}{|\Omega|} \left[ \frac{b_0\varepsilon}{A\sqrt{D}u_j} + \sum_{i \neq j}^k \frac{b_0\varepsilon}{A\sqrt{D}u_i} \right]. \quad (\text{B.20})$$

Upon using (B.7) for  $L_\varepsilon$  and  $\eta_\varepsilon$ , (B.20) reduces to the following result, in agreement with (B.6) of [62]:

$$1 - u_j = \frac{b_0\varepsilon^2}{A^2 D \nu u_j} + \frac{2\pi}{|\Omega|} \frac{b_0\varepsilon^2}{A^2} \sum_{i=1}^k \frac{1}{u_i} = \frac{L_\varepsilon \eta_\varepsilon}{u_j} + \sum_{i=1}^k \frac{L_\varepsilon}{u_i}. \quad (\text{B.21})$$

### B.3 Comparison of the Global Eigenvalue Problem with the NLEP of [62]

Next, we show for  $\mathcal{A} = \mathcal{O}(\nu^{1/2})$  and  $D = \mathcal{O}(\nu^{-1})$  that our eigenvalue problem, consisting of (4.8) coupled to (4.13), can be reduced to the NLEP (B.10) derived in [62]. To show this, we expand  $\Phi_j$ ,  $N_j$ ,  $B_j$ , and  $C_j$ , in (4.8) as

$$B_j = B_{j0} + \nu B_{j1} + \dots, \quad C_j = \nu(C_{j0} + \nu C_{j1} + \dots), \quad N_j = N_{j0} + \nu N_{j1} + \dots, \quad \Phi_j = \nu\psi_j + \dots.$$

Upon substituting these expansions, together with  $U_j \sim \nu^{-1/2}\chi_{0j}$  and  $V_j \sim \nu^{1/2}w/\chi_{0j}$ , into (4.8) for  $N_j$ , we conclude that  $N_{j0} = B_{j0}$ , and that  $N_{j1}$  satisfies

$$\Delta_\rho N_{j1} = \frac{w^2}{\chi_{0j}^2} B_{j0} + 2w\psi_j, \quad 0 < \rho < \infty; \quad N_{j1} \rightarrow C_{j0} \ln \rho + B_{j1} \quad \text{as } \rho \rightarrow \infty. \quad (\text{B.22})$$

Upon applying the divergence theorem to (B.22), we calculate  $C_{j0}$  as

$$C_{j0} = \frac{b_0}{\chi_{0j}^2} B_{j0} + 2 \int_0^\infty w\psi_j \rho d\rho, \quad b_0 \equiv \int_0^\infty w^2 \rho d\rho. \quad (\text{B.23})$$

Then, we let  $D = D_0/\nu \gg 1$  where  $D_0 = \mathcal{O}(1)$ , and we impose that  $\chi_{0j} = \chi_0$  for  $j = 1, \dots, k$ , so that to leading-order each local spot solution is the same. For  $D \gg 1$ , the  $\lambda$ -dependent Green's function  $G_{\lambda ij}$  and its regular part,  $R_{\lambda j,j}$ , satisfying (4.11), have the leading-order behavior

$$G_{\lambda ij} \sim \frac{D}{|\Omega|(1+\tau\lambda)} + \mathcal{O}(1), \quad i \neq j; \quad R_{\lambda j,j} \sim \frac{D}{|\Omega|(1+\tau\lambda)} + \mathcal{O}(1). \quad (\text{B.24})$$

Upon using (B.24), together with  $B_j \sim B_{j0}$  and  $C_j \sim \nu C_{j0}$ , we obtain that (4.13), with  $D = D_0/\nu$ , reduces to

$$C_{j0} + \frac{2\pi D_0}{(1+\tau\lambda)|\Omega|} \sum_{i=1}^k C_{i0} + B_{j0} = 0, \quad j = 1, \dots, k.$$

Upon substituting (B.23) for  $C_{j0}$  into this equation, we obtain that  $B_{j0}$  for  $j = 1, \dots, k$  satisfies

$$\left(1 + \frac{b_0}{\chi_0^2}\right) B_{j0} + \frac{2\pi D_0}{(1+\tau\lambda)|\Omega|} \frac{b_0}{\chi_0^2} \sum_{i=1}^k B_{i0} = -2 \int_0^\infty w\psi_j \rho d\rho - \frac{4\pi D_0}{(1+\tau\lambda)|\Omega|} \sum_{i=1}^k \int_0^\infty w\psi_i \rho d\rho. \quad (\text{B.25})$$

Next, we define the vectors  $\mathbf{p}_0$  and  $\Psi$  by  $\mathbf{p}_0 \equiv (B_{10}, \dots, B_{k0})^T$  and  $\Psi \equiv (\int_0^\infty w\psi_1 \rho d\rho, \dots, \int_0^\infty w\psi_k \rho d\rho)^T$ . Then, (B.25) can be written in matrix form in terms of  $\mathbf{e} = (1, \dots, 1)^T$  as

$$\left[ \left(1 + \frac{b_0}{\chi_0^2}\right) I + \frac{2\pi D_0}{(1+\tau\lambda)|\Omega|} \frac{b_0}{\chi_0^2} \mathbf{e}\mathbf{e}^T \right] \mathbf{p}_0 = - \left( 2I + \frac{4\pi D_0}{(1+\tau\lambda)|\Omega|} \mathbf{e}\mathbf{e}^T \right) \Psi.$$

The matrix multiplying  $\mathbf{p}_0$  is an invertible rank-one perturbation of the identity matrix, and hence

$$\mathbf{p}_0 = \mathcal{D}\Psi, \quad \mathcal{D} \equiv - \left[ \left(1 + \frac{b_0}{\chi_0^2}\right) I + \frac{2\pi D_0}{(1+\tau\lambda)|\Omega|} \frac{b_0}{\chi_0^2} \mathbf{e}\mathbf{e}^T \right]^{-1} \left( 2I + \frac{4\pi D_0}{(1+\tau\lambda)|\Omega|} \mathbf{e}\mathbf{e}^T \right). \quad (\text{B.26})$$

We then re-write some quantities in the symmetric matrix  $\mathcal{D}$  in terms of  $L_\varepsilon$  and  $\eta_\varepsilon$ , as defined in (B.7), to get  $b_0/\chi_0^2 = \eta_\varepsilon L_\varepsilon/u_0^2$  and  $2\pi D_0/[(1+\tau\lambda)|\Omega|] = [\eta_\varepsilon(1+\tau\lambda)]^{-1}$ . Since the eigenvalues of the matrix  $\mathbf{e}\mathbf{e}^T$  are either  $k$  or  $0$ , the two distinct eigenvalues  $r_1$  and  $r_2$  of  $\mathcal{D}$  are

$$r_1 = -\frac{2\chi_0^2}{b_0} \frac{L_\varepsilon\eta_\varepsilon(1+\tau\lambda) + kL_\varepsilon}{(u_0^2 + L_\varepsilon\eta_\varepsilon)(1+\tau\lambda) + kL_\varepsilon}, \quad r_2 = -\frac{2\chi_0^2}{b_0} \frac{L_\varepsilon\eta_\varepsilon}{u_0^2 + L_\varepsilon\eta_\varepsilon}. \quad (\text{B.27})$$

Finally, to obtain an NLEP we substitute  $U_j \sim \nu^{-1/2}\chi_0$ ,  $V_j \sim \nu^{1/2}w/\chi_0$ ,  $\Phi_j \sim \nu\psi_j$ , and  $N_{j0} \sim B_{j0}$ , into (4.8) for  $\Phi_j$ , which leads to the following radially symmetric vector NLEP for  $\psi \equiv (\psi_1, \dots, \psi_k)^T$ :

$$\Delta_\rho\psi - \psi + 2w\psi + \frac{w^2b_0}{\chi_0^2} \frac{\int_0^\infty \rho w \mathcal{D}\psi d\rho}{\int_0^\infty \rho w^2 d\rho} = \lambda\psi, \quad 0 < \rho < \infty; \quad \psi \rightarrow 0, \quad \text{as } \rho \rightarrow \infty.$$

By diagonalizing this vector NLEP by using the eigenpairs of  $\mathcal{D}$ , we obtain the scalar NLEP

$$\Delta_\rho\psi_c - \psi_c + 2w\psi_c + w^2 \left( \frac{r_i b_0}{\chi_0^2} \right) \frac{\int_0^\infty \rho w \psi_c d\rho}{\int_0^\infty \rho w^2 d\rho} = \lambda\psi_c, \quad 0 < \rho < \infty; \quad i = 1, 2, \quad (\text{B.28})$$

where  $r_1$  and  $r_2$  are the eigenvalues of  $\mathcal{D}$  given in (B.27). This NLEP is identical to the NLEP (B.10) studied rigorously in [62]. Therefore, we conclude that our global eigenvalue problem in §4.2 reduces to leading-order in  $\nu$  to the NLEP problem of [62] when  $A = O(\varepsilon[-\ln\varepsilon]^{1/2})$  and  $D = \mathcal{O}(\nu^{-1})$ .

### Appendix C Numerics for the Global Eigenvalue Problem: Competition and Oscillatory Instabilities

In §5–§6 stability thresholds are computed for spot configurations  $\mathbf{x}_1, \dots, \mathbf{x}_k$  for which the Green's matrix  $\mathcal{G}$  and the  $\lambda$ -dependent Green's matrix  $\mathcal{G}_\lambda$  are circulant. Therefore, we must solve the coupled eigenvalue problem (4.17) and (4.14), where the common spot profile and source strength  $S_c$  satisfy (2.3) and (2.22), respectively. In solving (2.3) and (4.14), we have chosen the finite interval  $[0, L]$  with  $L = 15$  to adequately approximate the infinite domain.

One numerical approach is to calculate the eigenvalue  $\lambda$  by a fixed-point iterative type method for a given set of parameters  $A$ ,  $D$ ,  $\tau$ , and  $\varepsilon$ , and for a given configuration of spots. The outline of this method is as follows:

- (1) Given  $\tau, \varepsilon, A$ , and  $D$ , calculate  $S_c$ ,  $\chi(S_c)$ , and the common spot profile  $U_c, V_c$  from (2.3) and (2.22).
- (2) For the  $n^{\text{th}}$  iteration, starting from a known eigenvalue  $\lambda^n$ , solve (4.14) for the common value  $\hat{B}_c$ .
- (3) Next, with  $\hat{B}_c$  known, compute a new approximation  $\lambda^{n+1}$  to  $\lambda$  by numerically solving (4.17) using Newton's method. This requires the evaluation of the matrix eigenvalues of the  $\lambda$ -dependent Green's matrix in (4.20).
- (4) Repeat step 2 using the updated value  $\lambda^{n+1}$  until the algorithm converges to some  $\lambda$ , with an error that is less than a given tolerance. Then,  $\lambda$  is the eigenvalue of the globally coupled eigenvalue problem.

This fixed-point iteration approach for  $\lambda$  converges rather slowly, and its success relies on the initial guess. In addition, since we need to study the stability for a range of values of the parameter  $\tau$ , the computational effort required with this simple scheme is rather large. In §5–6, this scheme is used to plot the path of certain eigenvalues in the complex plane as a parameter is varied.

Our primary numerical method used in §5–6 is based on the assumption that an instability occurs at some critical values of the parameters. For instance, to compute the Hopf bifurcation threshold  $\tau_H$ , we assume that there is a complex conjugate pair of pure imaginary eigenvalues when  $\tau = \tau_H$  for which  $\lambda_r \equiv \text{Re}(\lambda) = 0$  and  $\lambda_i \equiv \text{Im}(\lambda) \neq 0$ . Instead of solving for  $\lambda$  for each given  $\tau$ , we fix  $\lambda_r = 0$ , and solve for the thresholds  $\tau_H$  and  $\lambda_i$ , associated with a specific eigenvalue  $\omega_{\lambda_j}$  and eigenvector  $\mathbf{v}_j$  of  $\mathcal{G}_\lambda$ . A rough outline of the algorithm that we use is as follows:

- (1) Given  $\varepsilon$ ,  $A$ , and  $D$ , calculate  $S_c$ ,  $\chi(S_c)$ , and the common spot profile  $U_c, V_c$  from (2.3) and (2.22).
- (2) Fix  $\lambda_r = 0$ . In the  $n^{\text{th}}$  iteration, starting from the current approximation  $\tau^{(n)}, \lambda_i^{(n)}$ , solve the BVP (4.14) with boundary conditions  $\hat{N}'_c(L) = 1/L$  and  $\hat{\Phi}'_c(L) = 0$  using COLSYS (cf. [2]). This yields  $\hat{B}_c$  as  $\hat{B}_c = \hat{N}_c(L) - \ln L$ , and its derivative  $\partial_{\lambda_i} \hat{B}_c$  is calculated numerically by varying  $\lambda_i$  using a centered difference scheme.
- (3) Calculate  $\mathcal{G}_\lambda$  and evaluate its  $j^{\text{th}}$  eigenvalue  $\omega_j(\tau\lambda_i)$ . The partial derivatives  $\partial_\tau \omega_j$  and  $\partial_{\lambda_i} \omega_j$  are computed numerically by a centered difference scheme.
- (4) Calculate the residuals  $\text{Re}(f_j^{(n)})$  and  $\text{Im}(f_j^{(n)})$  in (4.18), and then calculate the Jacobian

$$\mathcal{J} \equiv \begin{pmatrix} \partial_\tau \text{Re}(f_j^{(n)}) & \partial_{\lambda_i} \text{Re}(f_j^{(n)}) \\ \partial_\tau \text{Im}(f_j^{(n)}) & \partial_{\lambda_i} \text{Im}(f_j^{(n)}) \end{pmatrix} = \begin{pmatrix} \partial_\tau \text{Re}(\hat{B}_c) & \partial_{\lambda_i} \text{Re}(\hat{B}_c) + 2\pi \partial_{\lambda_i} \text{Re}(\omega_j) \\ \partial_\tau \text{Im}(\hat{B}_c) & \partial_{\lambda_i} \text{Im}(\hat{B}_c) + 2\pi \partial_{\lambda_i} \text{Im}(\omega_j) \end{pmatrix}.$$

- (5) Use Newton's method to update  $\begin{pmatrix} \tau^{(n+1)} \\ \lambda_i^{(n+1)} \end{pmatrix} = \begin{pmatrix} \tau^{(n)} \\ \lambda_i^{(n)} \end{pmatrix} - \mathcal{J}^{-1} \begin{pmatrix} \text{Re}(f_j^{(n)}) \\ \text{Im}(f_j^{(n)}) \end{pmatrix}$ . Then go to step 2 and iterate further until reaching a specified tolerance.

To compute competition instability thresholds, we can use either the simpler formulation (4.24), or else employ a similar approach to that outlined above for computing oscillatory instability thresholds. The competition instability threshold occurs at  $\lambda = 0$  when the largest eigenvalue first enters the right half plane along the  $\text{Im}(\lambda) = 0$  axis. For this case, the  $\lambda$ -dependent matrix satisfies  $\mathcal{G}_{\lambda=0} = \mathcal{G}$ , and both  $\hat{B}_c$  and  $\omega_j$  are real-valued. We fix all the other parameters, and choose either  $A$ ,  $D$  or the spot location as the bifurcation parameter. For instance, if we treat  $A$  as the bifurcation parameter, then the algorithm to compute the competition stability threshold is as follows:

- (1) Set  $\lambda = 0$  and fix all of the parameters except for  $A$ . Calculate  $\mathcal{G}$  and its  $j^{\text{th}}$  eigenvalue  $\omega_j$ .
- (2) In the  $n^{\text{th}}$  iteration, starting from initial guess  $A^{(n)}$  for  $A$ , we calculate  $S_c$  and  $U_c, V_c$  from (2.22) and (2.3).
- (3) Solve the BVP (4.14) with  $\lambda = 0$  and  $\hat{N}'_c(L) = 1/L$  and  $\hat{\Phi}'_c(L) = 0$ . Compute  $\hat{B}_c$  as  $\hat{B}_c = \hat{N}_c(L) - \ln L$ .
- (4) Substitute  $\hat{B}_c$  and  $\omega_j$  in (4.17), and calculate the real-valued residual  $f_j^{(n)}$ .
- (5) Compute  $\frac{\partial \hat{B}_c}{\partial S_c}$  numerically by a centered difference scheme. Also compute  $\frac{\partial f_j^{(n)}}{\partial A} \equiv \frac{\partial \hat{B}_c}{\partial A} = \frac{\partial \hat{B}_c}{\partial S_c} \frac{\partial S_c}{\partial A}$ .
- (6) In (4.17), use Newton's method to update  $A^{(n+1)} = A^{(n)} - \left( \partial f_j^{(n)} / \partial A \right) f_j^{(n)}$ . Then, go to step 2 and iterate further until reaching a specified tolerance.

In computing the thresholds for an oscillatory instability for the infinite-domain problem in §5, and for the unit square and disk in §6, we must evaluate the  $\lambda$ -dependent Green's matrix  $\mathcal{G}_\lambda$ . This is done by replacing  $D$  with  $D/(1 + \tau\lambda)$  in the explicit formulae of Appendix A. However, since  $\lambda$  is in general complex, in order to use the results in Appendix A we must be able to evaluate the required modified Bessel functions  $K_n(z)$  and  $I_n(z)$  of a complex argument. This was done using the special function software of [64].

In §5–§6 the numerical approach outlined in this appendix was used to compute oscillatory and competition instability thresholds for various spot configurations in the infinite plane as well as the unit square and disk.

## References

- [1] E. Anderson et al. (1999), *LAPACK User's Guide: Third Edition*, SIAM Publications.
- [2] U. Ascher, R. Christiansen and R. Russell (1979), *Collocation software for boundary value ODE's*, Math. Comp., **33**, pp. 659–679.

- [3] Y. A. Astrov and H. G. Purwins (2001), *Plasma spots in a gas discharge system: birth, scattering and formation of molecules*, Phys. Lett. A, **283**(3-4), pp. 349–354.
- [4] Y. A. Astrov and H. G. Purwins (2006), *Spontaneous division of dissipative solitons in a planar gas-discharge system with high ohmic electrode*, Phys. Lett. A, **358**(5-6), pp. 404–408.
- [5] N. Berglund and H. Kunz (1999), *Memory effects and scaling laws in slowly driven systems*, J. Phys. A, **32**(1), pp. 15–19.
- [6] J. G. Blom, R. A. Trompert and J. G. Verwer (1996), *Algorithm 758: VLUGR 2: A vectorizable adaptive grid solver for PDEs in 2D*, ACM Trans. Math. Softw., **22**(3), pp. 302–328.
- [7] S. Boatto and C. Simo (2008), *Thomson’s heptagon: A case of bifurcation at infinity*, Physica D, **237**(14), pp. 2051–2055.
- [8] S. Boatto and H. Cabral (2003), *Nonlinear stability of a latitudinal ring of point-vortices on a nonrotating sphere*, SIAM J. Appl. Math., **64**(1), pp. 216–230.
- [9] W. Chen and M. J. Ward (2009), *Oscillatory instabilities and dynamics of multi-spike patterns for the one-dimensional Gray-Scott model*, Europ. J. Appl. Math **20**(2), pp. 187–214.
- [10] W. Chen, D. Iron, J. Rumsey and M. J. Ward (2010), *The stability and dynamics of two-spot patterns for a class of reaction-diffusion systems in  $\mathbb{R}^2$* , to be submitted, Studies in Applied Math.
- [11] X. Chen and M. Kowalczyk (2001), *Dynamics of an interior spike in the Gierer-Meinhardt system*, SIAM J. Math. Anal., **33**(1), pp. 172–193.
- [12] H. Cheng, J. Huang and T. J. Leiterman (2006), *An adaptive fast solver for the modified Helmholtz equation in two dimensions*, J. Comput. Phys., **211**(2), pp. 616–637.
- [13] D. Coombs, R. Straube and M. J. Ward (2009), *Diffusion on a sphere with localized traps: mean first passage time, eigenvalue asymptotics, and Fekete points*, SIAM J. Appl. Math., **70**(1), pp. 302–332.
- [14] P. W. Davis, P. Blanchedeau, E. Dullos and P. De Kepper (1998), *Dividing blobs, chemical flowers, and patterned islands in a reaction-diffusion system*, J. Phys. Chem. A, **102**(43), pp. 8236–8244.
- [15] A. Doelman, W. Eckhaus and T. J. Kaper (2001), *Slowly-modulated two-pulse solutions in the Gray-Scott model I: asymptotic construction and stability*, SIAM J. Appl. Math., **61**(3), pp. 1080–1102.
- [16] A. Doelman, W. Eckhaus and T. J. Kaper (2001), *Slowly-modulated two-pulse solutions in the Gray-Scott model II: geometric theory, bifurcations and splitting dynamics*, SIAM J. Appl. Math., **61**(6), pp. 2036–2062.
- [17] A. Doelman, R. A. Gardner and T. J. Kaper (2002), *A stability index analysis of 1-D patterns of the Gray Scott model*, Memoirs of the AMS, **155**, No. 737.
- [18] A. Doelman, R. A. Gardner and T. J. Kaper (1998), *Stability analysis of singular patterns in the 1D Gray-Scott model: A matched asymptotic approach*, Physica D, **122**(1-4), pp. 1–36.
- [19] A. Doelman and T. J. Kaper (2003), *Semistrong pulse interactions in a class of coupled reaction-diffusion systems*, SIAM J. Appl. Dyn. Sys., **2**(1), pp. 53–96.
- [20] A. Doelman, T. J. Kaper and L. A. Peletier (2006), *Homoclinic bifurcations at the onset of pulse self-replication*, J. Differential Equations, **231**(1), pp. 359–423.
- [21] A. Doelman, T. J. Kaper and K. Promislow (2007), *Nonlinear asymptotic stability of the semi-strong pulse dynamics in a regularized Gierer-Meinhardt model*, SIAM J. Math. Anal., **38**(6), pp. 1760–1789.
- [22] S. Ei, M. Mimura and M. Nagayama (2002), *Pulse-pulse interaction in reaction-diffusion systems*, Physica D, **165**(3-4), pp. 176–198.
- [23] S. Ei, M. Mimura and M. Nagayama (2006), *Interacting spots in reaction-diffusion systems*, Discrete Contin. Dyn. Sys. Series A, **14**(1), pp. 31–62.
- [24] S. Ei, Y. Nishiura and K. Ueda (2001),  *$2^n$  Splitting or edge splitting?: A manner of splitting in dissipative systems*, Japan. J. Indust. Appl. Math., **18**, pp. 181–205.
- [25] S. Ei and J. Wei (2002), *Dynamics of metastable localized patterns and its application to the interaction of spike solutions for the Gierer-Meinhardt system in two space dimensions*, Japan J. Indust. Appl. Math., **19**(2), pp. 181–226.
- [26] See *FlexPDE* website <http://www.pdesolutions.com> for details.
- [27] S. Gueron and I. Shafir (1999), *On a discrete variational problem involving interacting particles*, SIAM J. Appl. Math., **60**(1), pp. 1–17.
- [28] D. Iron and M. J. Ward (2002), *The dynamics of multi-spike solutions to the one-dimensional Gierer-Meinhardt model*, SIAM J. Appl. Math., **62**(6), pp. 1924–1951.
- [29] D. Iron, M. J. Ward and J. Wei (2001), *The stability of spike solutions to the one-dimensional Gierer-Meinhardt model*, Physica D, **150**(1-2), pp. 25–62.
- [30] E. Knobloch (2008), *Spatially localized structures in dissipative systems: open problems*, Nonlinearity, **21**(1), pp. T45–T60.
- [31] T. Kolokolnikov and M. J. Ward (2003), *Reduced-wave Green’s functions and their effect on the dynamics of a spike for the Gierer-Meinhardt model*, Europ. J. Appl. Math., **14**(5), pp. 513–545.
- [32] T. Kolokolnikov, M. S. Titcombe and M. J. Ward (2005), *Optimizing the fundamental Neumann eigenvalue for the Laplacian in a domain with small traps*, Europ. J. Appl. Math., **16**(2), pp. 161–200.
- [33] T. Kolokolnikov, M. J. Ward and J. Wei (2006), *Slow translational instabilities of spike patterns in the one-dimensional Gray-Scott model*, Interfaces Free Bound., **8**(2), pp. 185–222.

- [34] T. Kolokolnikov, M. J. Ward and J. Wei (2005), *The existence and stability of spike equilibria in the one-dimensional Gray-Scott Model: The low feed-rate regime*, Studies in Appl. Math., **115**(1), pp. 21–71.
- [35] T. Kolokolnikov, M. J. Ward and J. Wei (2005), *The existence and stability of spike equilibria in the one-dimensional Gray-Scott model: The pulse-splitting regime*, Physica D., **202**(3-4), pp. 258–293.
- [36] T. Kolokolnikov, W. Sun, M. J. Ward and J. Wei (2006), *The stability of a stripe for the Gierer-Meinhardt model and the effect of saturation*, SIAM J. Appl. Dyn. Sys., **5**(2), pp. 313–363.
- [37] T. Kolokolnikov, M. J. Ward and J. Wei (2006), *Zigzag and breakup instabilities of stripes and rings for the two-dimensional Gray-Scott model*, Studies in Appl. Math., **116**(1), pp. 35–95.
- [38] T. Kolokolnikov, M. J. Ward, and J. Wei (2009), *Spot self-replication and dynamics for the Schnakenburg model in a two-dimensional domain*, J. Nonlinear Sci., **19**(1), pp. 1–56.
- [39] P. Mandel and T. Erneux (1987), *The slow passage through a steady bifurcation: delay and memory effects*, J. Stat. Phys., **48**(5-6), pp. 1059–1070.
- [40] K. Lee, W. D. McCormick, J. E. Pearson and H. L. Swinney (1994), *Experimental observation of self-replicating spots in a reaction-diffusion system*, Nature, **369**(2), pp. 215–218.
- [41] D. Morgan and T. Kaper (2004), *Axisymmetric ring solutions of the Gray-Scott model and their destabilization into spots*, Physica D, **192**(1-2), pp. 33–62.
- [42] C. B. Muratov and V. V. Osipov (2001), *Spike autosolitons and pattern formation scenarios in the two-dimensional Gray-Scott model*, Eur. Phys. J. B, **22**, pp. 213–221.
- [43] C. B. Muratov and V. V. Osipov (2002), *Stability of static spike autosolitons in the Gray-Scott model*, SIAM J. Appl. Math., **62**(5), pp. 1463–1487.
- [44] C. B. Muratov and V. V. Osipov (2000), *Static spike autosolitons in the Gray-Scott model*, J. Phys. A: Math Gen., **33**, pp. 8893–8916.
- [45] Y. Nishiura (2002), *Far-from equilibrium dynamics, translations of mathematical monographs*, Vol. **209**, AMS Publications, Providence, Rhode Island.
- [46] Y. Nishiura and D. Ueyama (1999), *A skeleton structure of self-replicating dynamics*, Physica D, **130**(1-2), pp. 73–104.
- [47] Y. Nishiura and D. Ueyama (2001), *Spatial-temporal chaos in Gray-Scott model*, Physica D, **150**(3-4), pp. 137–162.
- [48] J. E. Pearson (1993), *Complex patterns in a simple system*, Science, **216**, pp. 189–192.
- [49] S. Pillay, M. J. Ward, A. Peirce and T. Kolokolnikov (2010), *An asymptotic analysis of the mean first passage time for narrow escape problems: part I: two-dimensional domains*, SIAM Multiscale Modeling and Simulation, **8**(3), pp. 803–835.
- [50] W. N. Reynolds, S. Ponce-Dawson and J. E. Pearson (1997), *Self-replicating spots in reaction-diffusion systems*, Phys. Rev. E, **56**(1), pp. 185–198.
- [51] W. N. Reynolds, S. Ponce-Dawson, and J. E. Pearson (1994), *Dynamics of self-replicating patterns in reaction-diffusion systems*, Phys. Rev. Lett., **72**(17), pp. 2797–2800.
- [52] C. P. Schenk, M. Or-Guil, M. Bode and H. Purwins (1997), *Interacting pulses in three-component reaction-diffusion systems on two-dimensional domains*, Phys. Rev. Lett., **78**(19), pp. 3781–3784.
- [53] W. Sun, M. J. Ward and R. Russell (2005), *The slow dynamics of two-spike solutions for the Gray-Scott and Gierer-Meinhardt systems: competition and oscillatory instabilities*, SIAM J. Appl. Dyn. Syst., **4**(4), pp. 904–953.
- [54] D. Ueyama (1999), *Dynamics of self-replicating patterns in the one-dimensional Gray-Scott model*, Hokkaido Math J., **28**(1), pp. 175–210.
- [55] V. K. Vanag and I. R. Epstein (2007), *Localized patterns in reaction-diffusion systems*, Chaos, **17**(3), 037110.
- [56] H. Van der Ploeg and A. Doelman (2005), *Stability of spatially periodic pulse patterns in a class of singularly perturbed reaction-diffusion equations*, Indiana Univ. Math. J., **54**(5), p. 1219–1301.
- [57] M. J. Ward, W. D. Henshaw and J. Keller (1993), *Summing logarithmic expansions for singularly perturbed eigenvalue problems*, SIAM J. Appl. Math., **53**(3), pp. 799–828.
- [58] M. J. Ward, D. McInerney, P. Houston, D. Gavaghan and P. Maini (2002), *The dynamics and pinning of a spike for a reaction-diffusion model*, SIAM J. Appl. Math., **62**(4), pp. 1297–1328.
- [59] M. J. Ward and J. Wei (2003), *Hopf bifurcations and oscillatory instabilities of spike solutions for the one-dimensional Gierer-Meinhardt model*, J. Nonlinear Sci., **13**(2), pp. 209–264.
- [60] J. Wei (2001), *Pattern formations in two-dimensional Gray-Scott model: existence of single-spot solutions and their stability*, Physica D, **148**(1-2), pp. 20–48.
- [61] J. Wei and M. Winter (2003), *Asymmetric spotty patterns for the Gray-Scott model in  $\mathbb{R}^2$* , Studies in Appl. Math., **110**(1), pp. 63–102.
- [62] J. Wei and M. Winter (2003), *Existence and stability of multiple spot solutions for the Gray-Scott model in  $\mathbb{R}^2$* , Physica D., **176**(3-4), pp. 147–180.
- [63] J. Wei and M. Winter (2008), *Stationary multiple spots for reaction-diffusion systems*, J. Math. Biol., **57**(1), pp. 53–89.
- [64] S. Zhang and J. Jin (1996), *Computation of special functions*, John Wiley and Sons, New Jersey. (fortran routines at <http://jin.ece.uiuc.edu/routines/routine.html>)